

STRENGTHENING OF METALS USING A GRAPHENE MONOLAYER

BY

KAIHAO ZHANG

DISSERTATION

Submitted in partial fulfillment of the requirements
for the degree of Doctor of Philosophy in Mechanical Engineering
in the Graduate College of the
University of Illinois at Urbana-Champaign, 2019

Urbana, Illinois

Doctoral Committee:

Assistant Professor Sameh H. Tawfick, Chair
Professor Placid M. Ferreira
Professor M. Taher A. Saif
Professor Pascal Bellon

ABSTRACT

A practical route to exploiting graphene's supreme properties for a variety of applications is to incorporate graphene layers in composite materials. Harnessing the high stiffness, intrinsic strength as well as transport properties of graphene in its composites requires the combination of high-quality graphene having low defect density, and the precise control of the interfacial interactions between the graphene and the matrix. These requirements equally hold for polymer and metal matrices, and enable the use of graphene in applications ranging from tough thin films for use in flexible electronics to the design of advanced aerospace structures. My dissertation addresses the synthesis, understanding and control of these composites and their mechanical properties probed from the nano- to the microscales.

To this end, a model system of ultrathin metal films coated with graphene monolayer via chemical vapor deposition (CVD) is designed and used to study as-grown graphene's contributions in graphene-metal composite thin films. Due to the thinness of the metal layer - typically less than 300 nm - individual or few graphene layers have a strong contribution on the composite thin film's mechanics. To create the most ideal interface between the metal and the graphene, CVD synthesis is used to grow the graphene wrapping around the surface of the films. A highly dynamic CVD synthesis route is developed to achieve high-quality graphene monolayer growth on ultrathin metal films while avoiding solid-state dewetting instability which takes place at the extremely high synthesis temperatures. We study how the competition between temperature-driven segregation and precipitation of carbon radicals governs the graphene's nucleation and growth kinetics on

ultrathin metal catalysts. The result of the dynamic recipe is repeatable growth of graphene monolayers with ultralow defect density as confirmed by Raman spectroscopy.

Precise mechanical characterization of ultrathin films is carried using various nanoindentation modalities including indentation of supported and freestanding thin films. CVD grown graphene-metal thin film composites exhibit unusual increase in the elastic modulus, strength and toughness. For example, there is 35 % and 57 % increases in the Young's modulus and tensile strength in graphene-palladium thin film composites compared to those for a bare palladium film having a thickness of 66 nm. Notably, this enhancement exhibits scale effects, where the composite modulus increase varies with the thickness, and is highest for the thinnest metal thicknesses. My work demonstrates that the inherent strong interfaces between graphene and strongly interacting metals like Ni and Pd after synthesis could lead to the manufacturing of composites with significantly higher performances. I also observed increase in toughness and qualitatively different modes of crack propagation owing to the addition of the high stiffness graphene shield on the metal surface during synthesis. Raman spectroscopy and electron imaging of surface reconstructions confirm the high interfacial stresses due to the combination of the lattice mismatch between the graphene and the metals and the kinetics of growth. The findings of this dissertation promote graphene-based thin film composites for flexible electronic devices, and enable fundamental studies of exploiting strain engineering at the graphene-metal interface for electronics, chemistry and mechanics. Furthermore, the results of this dissertation are broadly relevant to the design of bulk graphene-based composite materials.

ACKNOWLEDGEMENTS

I am deeply indebted to my adviser Sameh Tawfick for his important role in my doctoral study and research. It has been an honor to be his first Ph.D. student. I joined Sam's group when he just came to Champaign. Sam provided me with every bit of guidance, expertise and assistance that I needed during my exploration in new areas. As an adviser, he has taught me how to do systematic experiments, fundamental research and how to efficiently showcase my work. As a mentor, he has assisted me to establish and clarify my research vision and career path. I appreciate all his contributions of creative ideas, prompt feedback, time and enthusiasm to make my Ph.D. experience productive and enjoyable.

I would like to thank our research collaborators Gaurav Bahl, Harley Johnson, Elif Ertekin at the U of I and Pascal Pochet at INAC in France. Gaurav has assisted and guided my first publication about laser assisted manufacturing, also the first chapter of this dissertation. Harley and Pascal have offered computational supports and many inspiring ideas to my experimental research on the graphene-metal interfacial science. It has been refreshing, in my later Ph.D. study, to enjoy the Nano Manufacturing group collaborating with Elif, who broadens my research vision in data driven advance manufacturing. Particularly, I would like to acknowledge my Ph.D. committee members, Placid Ferreira, Taher Saif and Pascal Bellon at the U of I for their time and invaluable feedback on my work.

The Kinetic Materials Research Group have been a great source of friendships, collaboration and advise to my personal and professional time at the U of I. I can still remember the origin group

members, Peter Lee, Ping-ju Chen, Jonathan Bunyan and I worked together to assemble the first chair for our labs in the winter of 2013. Our friendship and collaboration are everlasting. I would like to acknowledge my colleague Matthew Poss, who has designed and fabricated the most professional apparatus for graphene synthesis. In regard to the study on graphene, I really appreciate our synthesis subgroup members: Matthew Robertson, Charalampos Androulidakis (Harris), Mingze Chen and Mitisha Surana. Matt R and Harris helped me immensely on the atomic force microscopy (AFM) scanning. Harris has inspired me the mechanical analysis of 2D materials in Raman spectroscopy. I particularly appreciate the assistance from Mingze. As my undergraduate mentee, he worked hard and closely with me around a whole year probing the challenging synthesis of high-quality graphene on the ultrathin metal substrates, which turned out to be the main chapter of this dissertation, and brought us the opportunities for subsequent graphene-metal interface studies. In my later experiments on the graphene-metal surface reconstructions, I am especially grateful for the assistance from Mitisha on Raman spectroscopy mapping.

Lastly, I am deeply indebted to my family for their support and understanding. Although we only united for very limited time over the past five years, their love makes me focus on my pursuits. The last word of acknowledgment is for my loving and understandable wife Yuan Tang, who has just received her Ph.D. degree in China. Every word we have said in our oversea phone call between the U.S. and China over the past five years is memorable and invaluable.

Kaihao Zhang

Champaign, IL

June 30, 2019

TABLE OF CONTENTS

CHAPTER 1: INTRODUCTION AND OUTLINE.....	1
1.1. Motivation.....	1
1.2. Dissertation outline	3
1.3. References.....	6
CHAPTER 2: FABRICATION OF ULTRALONG METAL NANOWIRES	7
2.1. Laser assisted draw-casting (LDC) process.....	7
2.1.1. Challenges in making long metal nanowires	7
2.1.2. Scalable draw-casting fabrication of metal nanowires	9
2.2. Fabrication of ultra-long Pd nanowires using LDC.....	13
2.2.1. Experimental Implement.....	13
2.2.2. Structural characterization of as-drawn Pd nanowires.....	17
2.3. Conclusions.....	22
2.4. References.....	23
CHAPTER 3: FABRICATION OF HIGH-QUALITY GRAPHENE-METAL NANOCOMPOSITES VIA CVD SYNTHESIS	24
3.1. Chemical vapor deposition synthesis with ultrathin metal films.....	24
3.1.1. Selection of metal catalysts for graphene synthesis.....	24
3.1.2. Kinetics of carbon segregation and precipitation in CVD processes.....	26
3.1.3. Experimental implement.....	32
3.2. Graphene synthesis on nano-grain ultrathin metal films	33
3.2.1. Solid-state dewetting of metal catalysts in CVD	33

3.2.2. Multilayer graphene synthesis on thin Ni films	35
3.3. Graphene synthesis on coarse grain thin metal films.....	38
3.3.1. Ultrathin Pd leaves with large grain structures	38
3.3.2. High-quality graphene monolayer synthesis on Pd leaves	41
3.4. Conclusions.....	48
3.5. References.....	49
CHAPTER 4: NANOMECHANICS AT THE GRAPHENE-METAL INTERFACE.....	51
4.1. Conformability of CVD grown graphene on polycrystalline thin metal films	52
4.2. Interfacial strain of CVD grown graphene on thin Pd films	55
4.2.1. Raman spectroscopy characterization of graphene on Pd leaves.....	55
4.2.2. Load transfer of as-grown PdGr leaf composites	60
4.3. Orientation dependent interfacial stresses in graphene on Pd substrate	62
4.3.1. Orientation dependent surface reconstructions on PdGr leaves	62
4.3.2. Strain at the graphene-Pd interface probed by Raman spectroscopy.....	66
4.4. Conclusions.....	75
4.5. References.....	76
CHAPTER 5: ELASTIC PROPERTIES OF GRAPHENE-COATED THIN METAL FILMS.....	78
5.1. Introduction to the elasticity of thin film materials	79
5.1.1. Surface stress effect in nanoscale elasticity	79
5.1.2. Mechanical property measurement for thin film materials.....	81
5.2. The elasticity enhancement in CVD grown Ni-MLG thin film composites.....	82
5.3. The elasticity enhancement of CVD grown PdGr thin film composites	89

5.3.1. Indentation modulus increase by graphene monolayer synthesis	89
5.3.2. Fabrication of freestanding PdGr thin film composites	91
5.3.3. Deflection of Pd and PdGr thin films in microbridge nanoindentation	94
5.3.4. Effect of mismatch interfacial stress on the elastic modulus of PdGr thin film composites.....	111
5.4. Conclusions.....	119
5.5. References.....	120
CHAPTER 6: STRENGTHENING AND TOUGHENING OF THIN METAL FILMS BY CVD GROWN GRAPHENE.....	123
6.1. Fracture of CVD grown Ni-MLG thin film composites	123
6.1.1. Strength of thin films probed by the membrane nanoindentation.....	123
6.1.2. Fracture behaviors at the graphene-Ni interface	126
6.2. Strengthening and toughening of graphene monolayer on polycrystalline thin Pd films	130
6.3. Fracture behaviors of single crystal thin Pd films with graphene monolayer.....	136
6.3.1. The onset of plasticity in as-grown PdGr thin film composites.....	137
6.3.2. Crack propagation in thin metal films coated with graphene monolayer	138
6.4. Conclusions.....	139
6.5. References.....	141
CHAPTER 7: CONCLUSIONS AND SUGGESTIONS FOR FUTURE WORK.....	142
7.1. Summary and conclusions	142
7.2. Discussions and suggestions for future work.....	144
7.2.1. Synthesis of graphene single crystal on polycrystalline metal substrates....	144

7.2.2. The intrinsic toughening mechanisms in graphene-metal nanocomposites.	145
7.2.3. Multi-functionality in graphene-metal composites.....	147
7.3. References.....	149

CHAPTER 1: INTRODUCTION AND OUTLINE

1.1. Motivation

High-quality low dimensional carbon-based materials, for instance carbon nanotubes (CNTs) and graphene promise exceptional performance owing to the high stiffness and strength of the covalent carbon-carbon bond and the ability to scale up the superb properties of sp^2 -hybridization by aligning CNT or graphene building blocks in fibers or sheets. However, broader applications of low dimensional carbon materials to real-world problems have yet been fulfilled because of challenges in material synthesis and processing, as well as the trade-off between structure quality and scalability.

Under laboratory conditions, CNT fibers spun directly from the chemical vapor deposition (CVD)-synthesized aerogel exhibit superior stiffness and strength than those of commercial carbon fibers, Dyneema or Kevlar.^{1, 2} Importantly, these laboratory-made CNT fibers usually show their outstanding properties at very small gauge lengths (<1 mm) whereas with much lower strength even for centimeter scale. Graphene, another sp^2 -hybridized carbon atoms similar to CNT, has been attracting great interest because of its intrinsic scalability with two-dimensional lattice and atomic scale thickness, as well as its supreme in-plane mechanical ($E = 1 \text{ TPa}, \sigma = 130 \text{ GPa}$),³ thermal and electrical conductive properties ($k = 3000 - 5000 \text{ W m}^{-1}\text{K}^{-1}, \sigma_e = 10^4 \text{ S cm}^{-1}$).⁴⁻⁷ Graphene fibers fabricated from reduced graphene oxide flakes via wet-spinning can possess strength to 652 MPa and electrical conductivity of 416 S cm^{-1} .⁸ However, these performances are orders magnitudes lower than those of graphene monolayer and inferior to CNT fibers, due to many factors such as poor graphene integrity and high structure defects from

fabrication processes. High temperature treatment ($>1800\text{ }^{\circ}\text{C}$) can lead to large crystalline domains in graphene fibers and achieve high strength ($\sim 1.08\text{ GPa}$).⁹ This is also far weaker than the pristine graphene performances, and less cost-effective.

One promising route to combine the mechanical, thermal and electrical properties is incorporating high quality graphene layers in composite materials. For example, copper nanowires with CVD synthesized graphene layer shows significant reduction in wire wall scattering of electrons, translating into $\sim 15\%$ faster electron mobility compared to bare copper nanowires.¹⁰ Nonetheless, most of the reported graphene reinforced composites suffer from inhomogeneous dispersion of graphene nanosheets in matrices, uncontrolled porosity and defect density caused by agglomeration of graphene layers, as well as insufficient graphene-matrix interfacial bonding.^{11, 12} The manufacturing of graphene-based composites requires not only scalable high-quality graphene sheet production, but that graphene-matrix also be well incorporated. Therefore, the goal of this dissertation is to design high performance graphene-based composites by bridging graphene synthesis and graphene-matrix interaction. CVD is an efficient way to produce scalable and high-quality graphene layers.¹³ Many efforts have been invented in interfaces between the graphene and the metal catalysts during CVD synthesis pursuing large area graphene layers. Yet, there is a lack of knowledge linking the atomic-level graphene synthesis mechanisms in CVD to the larger scale integration of the graphene and the metallic matrices in a graphene-metal composite for many reasons. Firstly, it is impractical to track the contributions of a single layer graphene on the mechanics of graphene-metal matrix composites fabricated by metallurgical mixing. These materials exhibit complex structures governed by graphene aggregation, metal grain refinements, weak interfaces and voids. Secondly, the inelastic properties of bulk composites made by mixing

the graphene with the metal powders typically shows large enhancements in yield strength for instance, but the fundamental mechanisms leading to the observed behaviors, such as the dislocations activities, are difficult to be probed in these materials.

To study this technologically important material, a well-controlled and tunable model composite is needed. This composite sample should play a similar role to that of individual nanostructures such as CNTs or graphene which can be individually probed. However, there exist several challenges to fabricate such a nanoscale sample: the metal needs to be extremely thin in order to clearly observe the contribution of a single or few graphene layers. The interface between the graphene and the metal needs to be clean and smooth. Ideally this interface needs to be accessible for structural characterization to probe the “epitaxy” of the carbon atoms onto the underlying crystalline metal. The fabrication of such graphene-coated thin films having this required epitaxial interface can only be achieved by CVD synthesis. However, synthesis of graphene on thin films (<500 nm) is challenged by the metal solid-state instability at the high temperatures encountered in CVD.

1.2. Dissertation outline

The scope of this dissertation is to create a new route to fabricate graphene-metal composite materials at nanoscale. To maximize the contributions of graphene’s properties, nanoscale metal substrates, including metal nanowires and ultrathin metal films are used as the catalysts for graphene synthesis in CVD. A recipe for high-quality graphene monolayer growth on metal nanostructures in high temperature CVD has been developed, enabling close investigation on the

graphene-metal interfaces and their functions in the mechanical behaviors of graphene-metal nanocomposites.

This dissertation is organized into the chapters as below:

Chapter 2 introduces a novel continuous fabrication method for metal nanowires based on a laser-assisted draw-casting (LDC) process. As-fabricated metal nanowires have large crystalline structures and outstanding mechanical as well as conductive properties, which can be used in flexible and stretchable conductors and are suitable for graphene nucleation in CVD.

Chapter 3 presents the fabrication of graphene-metal nanocomposites using a dynamic CVD process. Given the challenges of instability of metal nanostructures at high temperature, the kinetic and dynamic model of carbon segregation and precipitation is developed to guide synthesis of high-quality graphene monolayer on nanothin metal films. Chapter 3 also presents another route to obtain this material using low temperature growth on Ni thin films. The latter route leads to multilayered graphene (MLG).

Chapter 4 describes structural characterizations of graphene-metal interfaces. The conformability of as-grown graphene layers on polycrystalline metal substrates is studied using multiple frequency atomic force microscopy (AFM) technique. Moreover, native strain configuration at the graphene-metal interfaces is studied by Raman spectroscopy of as-grown graphene on metal substrates. This chapter discusses the fundamental mechanisms of mechanical reinforcement of graphene in its composites.

Chapter 5 characterizes the elastic behaviors of as-grown graphene-metal thin film composites using nanoindentation of supported and suspended thin films. We present a new approach to accurately extract the elastic properties from nanoindentation data of freestanding ultrathin films. This chapter demonstrates that the favorable interfacial mechanics can significantly modify the composite elastic properties, and discusses the mechanisms behind.

Chapter 6 presents the inelastic behavior of as-grown graphene-metal thin film composites. Our measurements show unusual strength increase in metals by merely a graphene monolayer synthesis. The toughness of these films is also increased as shown by qualitatively different cracking behaviors. The fundamental strengthening and toughening mechanisms of graphene monolayer on polycrystalline thin metal films are elucidated. This chapter also presents the preliminary explorations of the intrinsic toughening mechanisms of graphene monolayer within a single Pd grain.

Chapter 7 summarizes the finding and contributions in this dissertation. Outlooks and study plans are proposed for fundamentally relating process to atomic structure and properties of graphene-crystalline materials composites, with special emphasis of interfacial mechanics and its role in fracture toughness.

1.3. References:

1. Behabtu, N.; Young, C. C.; Tsentalovich, D. E.; Kleinerman, O.; Wang, X.; Ma, A. W.; Bengio, E. A.; ter Waarbeek, R. F.; de Jong, J. J.; Hoogerwerf, R. E.; Fairchild, S. B.; Ferguson, J. B.; Maruyama, B.; Kono, J.; Talmon, Y.; Cohen, Y.; Otto, M. J.; Pasquali, M. *Science* **2013**, 339, (6116), 182-6.
2. Koziol, K.; Vilatela, J.; Moisala, A.; Motta, M.; Cunniff, P.; Sennett, M.; Windle, A. *Science* **2007**, 318, (5858), 1892-5.
3. Lee, C.; Wei, X.; Kysar, J. W.; Hone, J. *Science* **2008**, 321, (5887), 385-388.
4. Geim, A. K. *Science* **2009**, 324, (5934), 1530-4.
5. Geim, A. K.; Novoselov, K. S. *Nat Mater* **2007**, 6, (3), 183-91.
6. Balandin, A. A.; Ghosh, S.; Bao, W.; Calizo, I.; Teweldebrhan, D.; Miao, F.; Lau, C. N. *Nano Letters* **2008**, 8, (3), 902-907.
7. Novoselov, K. S.; Geim, A. K.; Morozov, S. V.; Jiang, D.; Zhang, Y.; Dubonos, S. V.; Grigorieva, I. V.; Firsov, A. A. *Science* **2004**, 306, (5696), 666-669.
8. Meng, F.; Lu, W.; Li, Q.; Byun, J.-H.; Oh, Y.; Chou, T.-W. *Advanced Materials* **2015**, 27, (35), 5113-5131.
9. Xin, G.; Yao, T.; Sun, H.; Scott, S. M.; Shao, D.; Wang, G.; Lian, J. *Science* **2015**, 349, (6252), 1083-1087.
10. Mehta, R.; Chugh, S.; Chen, Z. *Nano Lett* **2015**, 15, (3), 2024-30.
11. Huang, X.; Qi, X.; Boey, F.; Zhang, H. *Chemical Society Reviews* **2012**, 41, (2), 666-686.
12. Stankovich, S.; Dikin, D. A.; Dommett, G. H. B.; Kohlhaas, K. M.; Zimney, E. J.; Stach, E. A.; Piner, R. D.; Nguyen, S. T.; Ruoff, R. S. *Nature* **2006**, 442, (7100), 282-286.
13. Novoselov, K. S.; Fal'ko, V. I.; Colombo, L.; Gellert, P. R.; Schwab, M. G.; Kim, K. *Nature* **2012**, 490, (7419), 192-200.

CHAPTER 2: FABRICATION OF ULTRALONG METAL NANOWIRES

Abstract

Metal nanostructures like thin metal films and metal nanowires are typically fabricated by physical vapor deposition and solution-based synthesis routes which are usually subjected to the trade-off between geometry uniformity and scalability. Moreover, a lack of control of the crystalline structures in metal catalysts fabricated by traditional methods usually attenuates their mechanical and catalytic behaviors. A cost-efficient and scalable metal micro and nanowires fabrication process with ability to tune the wire dimensions and microstructures is highly sought-after. In this chapter, we develop a novel laser assisted draw-casting process (LDC) to fabricate single ultralong metal nanowire. The proposed LDC process is fast (~10 seconds) and capable to produce 140 mm long palladium wire with tip diameter to be less than 200 nm. As-drawn Pd nanowires have large crystalline structures (>20 μm) which span across the whole wire thickness, showing potential to achieve high electrical conductivities and outstanding mechanical properties. Importantly, this provides a proper metal matrix for high-quality nanocomposites.

2.1. Laser assisted draw-casting (LDC) process

2.1.1. Challenges in making long metal nanowires

Commercial methods for manufacturing continuous metallic microwires rely on mechanical drawing of solid feedstock to the required dimensions.¹ It becomes challenging and costly when drawing metal wires down to sub-ten microns in diameter, since the materials exhibit strong size-dependent mechanical properties and become very sensitive to surface stress from processing. There are a number of nanofabrication methods to produce metal nanowires with desired

dimensions and properties. However, most of current fabrication routes are limited by the trade-off between geometry uniformity and wire continuity, as depicted in Figure 2.1. For example, bottom-up processes like solution-based synthesis can massively produce silver nanowires with smooth surface and high crystallinity, whereas the wire length is usually less than 30 μm due to a lack of understanding of nanowire growth mechanism.² On the other hand, top-down methods including lithographic patterning, physical vapor deposition can produce Au, Pt or Pd nanowires with sub-50 nm width and significant length.^{3, 4} But they typically have polycrystalline microstructures and irregular cross sections.

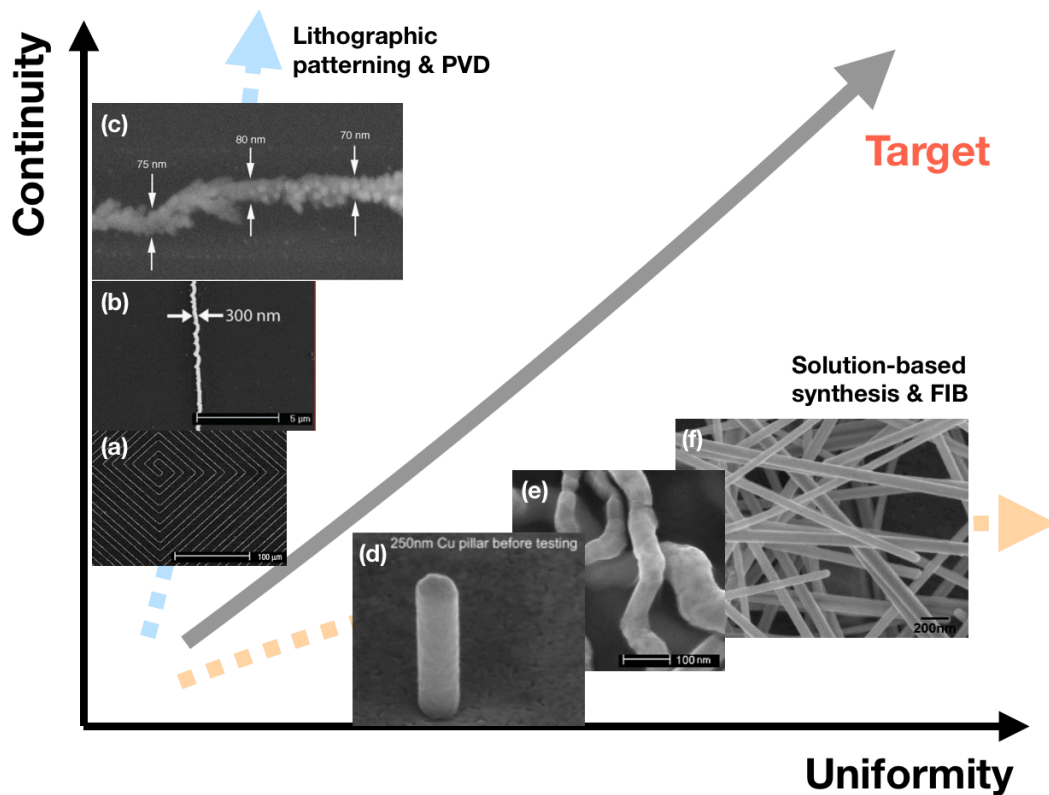


Figure 2.1. The trade-off between geometry uniformity and continuity in making metallic nanowire. SEM images are adapted from references: (a),³ (b),⁴ (c),⁵ (d),⁶ (e),⁷ (f).⁸

2.1.2. Scalable draw-casting fabrication of metal nanowires

Taylor proposed a facile filament drawing method in 1924.⁹ Figure 2.2 illustrates the drawing mechanism in the Taylor drawing process: the metal to be drawn is heated within a glass tube having diameter of ~ 2 mm, and with one closed end. As the metal core melts and glass softens, the close end of the tube is drawn quickly by hand to produce glass encapsulated metal rods. The metal-glass rod can be about 300 mm long with diameter down to 0.5 mm. The glass cladding can be then removed using hydrofluoric etching leaving the bare metal filament. Taylor drawing process is intrinsically an easy and inexpensive route to produce metallic microwires and has been recently used by Yoel Fink and other researchers to fabricate multimodal and multifunctional optical fibers and metal nanowires.¹⁰⁻¹³

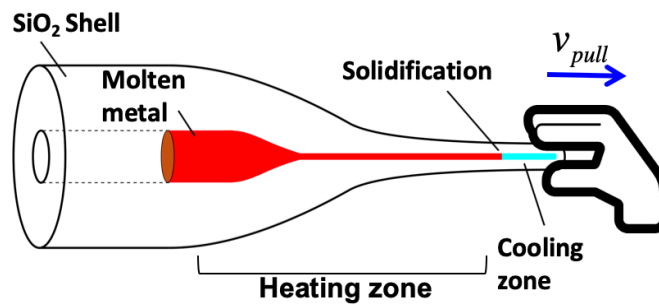


Figure 2.2. Schematic of Taylor drawing process

To be more specific, the actual Taylor drawing process and its modified versions are similar to commercial continuous casting of metal slabs, e.g. steel. The softened glass tube serves as a viscous mold with the tapered inner diameter. Under a suitable drawing condition, the molten metal fills the deformed glass cladding and follows the motion of glass. There are several factors that restrict the lower limit of diameter of metal wire and upper limit of the drawing rate can be reached in this draw-casting process:

- In the heating zone. The range of drawing temperatures is determined by the mismatch in metal and glass viscosities, as shown in Figure 2.3a. At temperatures beyond metal's melting point, the metal core, usually has orders magnitude lower viscosity than that in glass cladding and can be considered as inviscid.

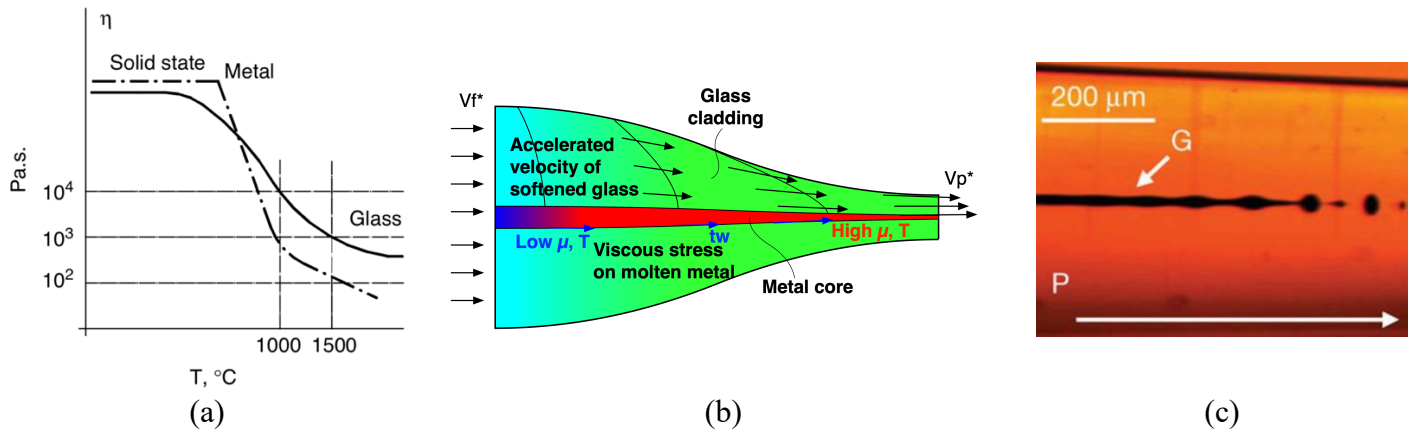


Figure 2.3. (a) Viscosity η as a function of temperature during the solidification process. The dash lines indicate the temperature region where the casting process can be realized.¹⁴ Viscosity and velocity mismatch in Taylor drawing process. (c) Optical microscope (OM) image of a glass core (G) breaks up into droplets in polymer cladding during drawing process.¹²

Here, we adopt the Taylor's metal-glass core-shell structure and propose a microscale continuous laser assisted draw-casting (LDC) process to produce metal nanowires. The process starts from a metal-glass preform consisted of a commercially available metal wire which is inserted inside a glass capillary tube. The preform is fixed to two motorized linear actuators, as shown in Figure 2.4a. Two CO_2 laser beams intersect on the preform and heat it to the elevated temperatures, at which glass capillary softens and the metal core melts. There is an instant drop in surface tension in the metal core caused by laser heating. The molten metal tends to bead up to minimize its surface energy before it fills the spacing of the glass capillary as the drawing motion starts. As a result, the molten metal is sealed within the softened capillary in the initial heating stage, and the drawing

forces are transferred by shear stresses at the inner capillary walls. We can tune the heating power and laser dwelling time so that the glass viscosity becomes low enough to enable high drawing rates and considerable reduction in the metal wire diameter in one drawing step. The process can be qualitatively described as illustrated in Figure 2.4b. The softened glass mold forms a conical-shape meniscus by a tangential hoop and axial stresses applied by the drawing stage, while it maintains high viscosity and confines the flow of metal melt. The profile evolution of the glass is a function of the temperature and velocity in the softened region, which can be predicted by the Navier-Stokes equation.^{15, 16} Due the significant difference between viscosities two core and shell materials, the drag from the metal on the glass can be ignored in heating zone. The glass capillary hence forms a dynamic mold, into which the molten metal is cast. Specifically, the shear stress at the metal-glass interface stretch the metal melt, which simultaneously fills the inner diameter. Capillarity of the liquid metal on the glass wall is crucial here since they either assist or resist the casting process. Notably, the volume change of stretched glass capillary and metal wire is balanced by the continuous feeding of preform at low speeds from the feeding stage. This theoretically allows the continuous drawing of metal-glass fibers with the desired dimensions.

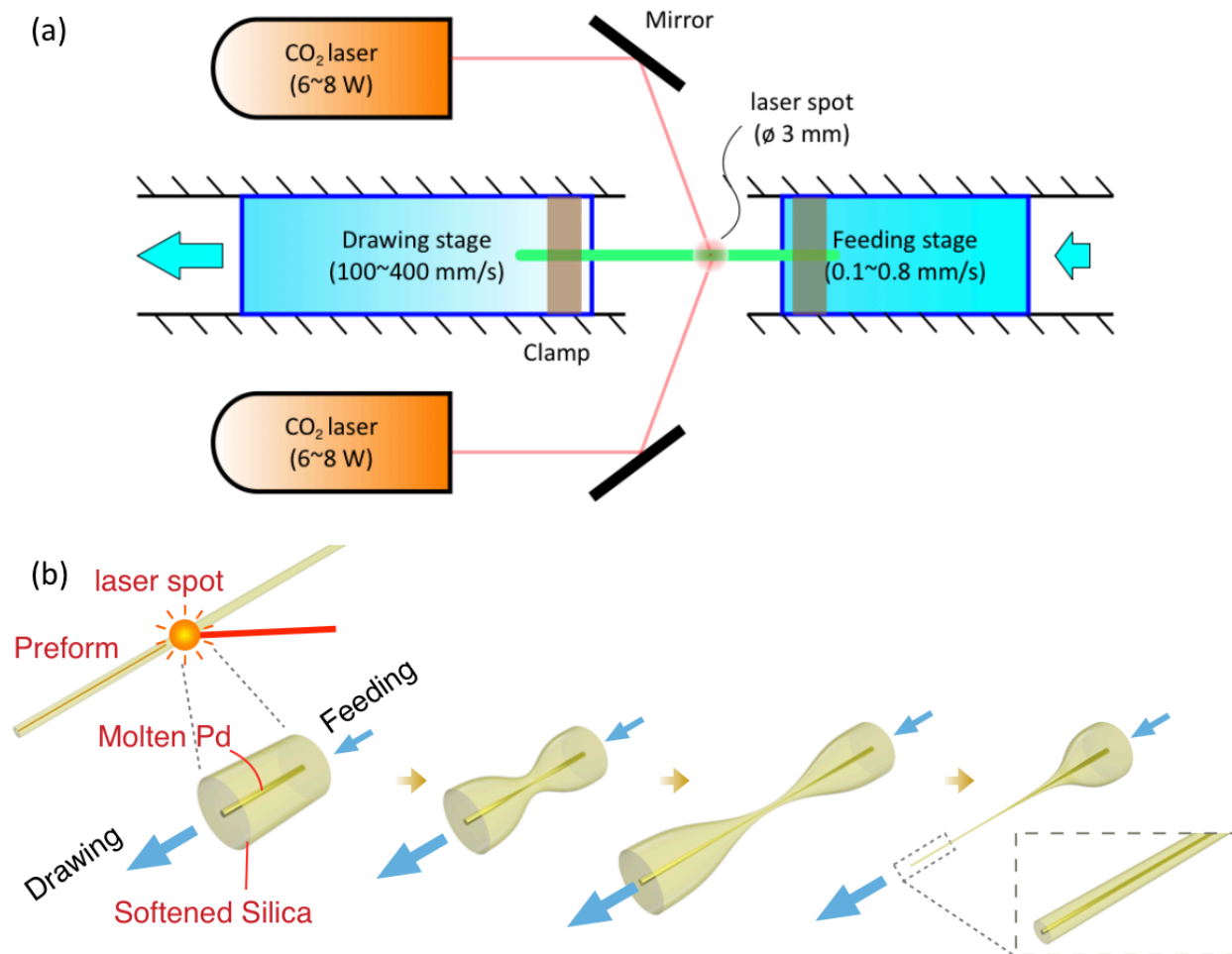


Figure 2.4. Schematics of (a) the LDC setup consisting of two CO₂ laser sources and two aligned linear actuators, and (b) Pd-silica preform deformation in the LDC process.

Table 2.1 lists the commonly used glass and metal materials. In this study, palladium (Pd) and fused silica are selected as the preform materials for the following reasons: (1) Pd has a melting point close to the softening point of silica capillary which pairs them up for fast heating and cooling conditions in the LDC process; (2) Pd is highly resistant to the oxidation and reaction with SiO₂ at high temperature hence this rules out the interfacial chemical reaction during laser heating; (3) Pd is an important catalyst for graphene synthesis due to its high carbon solubility and strong graphene-Pd interaction, which will be discussed in details in Chapter 3.

Table 2.1. Material selection for LDC process

	Borosilicate	Fused silica	Cu	Pd	Ni
Melting point/ Softening point ($^{\circ}\text{C}$)	820	1686	1084	1555	1453
Density (g cm^{-3})	2.23	2.20	8.94	12.16	8.91
Dynamic viscosity ($\text{Pa} \cdot \text{s}$) at melting point	$7 \times 10^{6.6}$	1×10^6	4×10^{-3}	4×10^{-3}	4.4×10^{-3}

2.2. Fabrication of ultra-long Pd nanowires using LDC

2.2.1. Experimental Implement

To validate the proposed LDC process, we use commercially available Pd wires with $25.4 \mu\text{m}$ in diameter and a fused silica capillary with ID of $50 \mu\text{m}$ (OD: $800 \mu\text{m}$, L: $\sim 40 \text{ mm}$). Figure 2.5a displays the actual LDC setup and Table 2.2 lists the instrument details. The Pd-silica preform is clamped across the drawing and feeding stages by bolted clamp assemblies, see Figure 2.5b. As discussed in the previous section, the drawing temperature and the corresponding viscosity of silica determine the rheological behavior and cone shape of the silica capillary in the heating zone, while the molten Pd just fills and follows the deformation of the silica mold. It is important to firstly acquire the local temperature variance in the preform during laser heating.

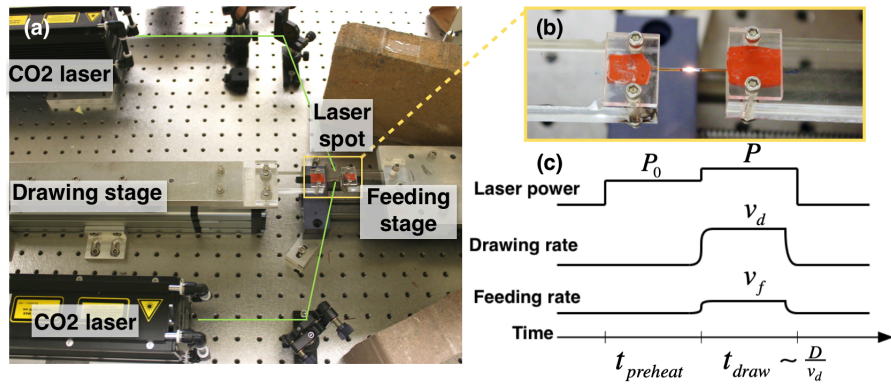


Figure 2.5. (a) Photograph of the LDC setup. (b) A clamped preform being preheated. (c) Main parameters in the LDC process. $P_0 = 14 \text{ W}$, $P = 15 \text{ W}$, $v_d = 200 - 400 \text{ mm s}^{-1}$, $v_f = 0.1 -$

$$0.8 \text{ mm s}^{-1}, t_{preheat} = 3 \text{ s}, t_{draw} = 2 \text{ s}.$$

Table 2.2. Materials and instruments used in LDC

Name	Parameters	Source
Pd wire	Ø 25.4 µm, 99.9%	California Fine Wire Co.
Cu wire	Ø 25.4 µm, 99.999%	
Ni wire	Ø 25.4 µm, 99.99%	
Silica capillary	ID 50 µm, OD 794 µm	PolyMicro (TSP050794)
Borosilicate	ID 142 µm, OD 559 µm	Drummond Microcaps
CO ₂ laser	10.6 µm wavelength, ~3 mm spot size	Synrad (48-1KWM and 48-2KWM)
Linear stage (feeding)	0.1-0.8 mm s ⁻¹	DryLin (H1W1150)
Linear stage (pulling)	200-400 mm s ⁻¹	PBC Linear (MTB055D-0902-14F12)

The transmittance of pure fused silica to CO₂ lasers having wavelength of 10.6 µm is less than 5%.¹⁷ In light of this fact, we need to preheat the silica mold with a lower laser power allowing the heat transfers into capillary wall and melt Pd. Preheating time $t_{preheat}$ and laser power P_0 can be optimized to enable the suitable softening and melting condition of Pd-silica preform as drawing starts. Figure 2.5c depicts a typical LDC process flow with preheat time $t_{preheat} = 3$ s and drawing time $t_{draw} = 2$ s. In this study, t_{draw} is limited by the setup dimensions. These drawing parameters have been validated by measuring the temperature in the preform during laser preheating. As illustrated in Figure 2.6a-2.6c, thermocouples (R-type, Pt-13% Rh) are attached to the inner and outer silica walls. At $t_{preheat} = 3$ s, we measure the outer wall temperature (T_1) to be ~1600 °C, which is in the range of the glass transition of pure fused silica (see Table 2.1). The measured temperature here is considered as the lower bound of the actual silica temperature due to losses associated with the thermocouple contact resistance. Notably, across the silica wall thickness of ~370 µm, the inner wall temperature (T_2) is very close to T_1 with the maximum gradient of ~80 °C. Considering the contact thermal resistance of thermocouple on the inner silica

wall and Pd surface, Pd surface temperature (T_3) is close to the melting point (1555 °C) of the metal core.

On the other hand, during Pd-silica deformation in $t_{draw} = 2$ s, combination of drawing (v_d) and feeding rate (v_f) determines the final strand's diameter as well as the continuity of Pd wire inside of silica mold. A simple mass conservation calculations gives the relation of Pd diameter reduction

between two stage rates as: $\phi_d = \phi_i \sqrt{\frac{v_f}{v_d}}$, where ϕ_i represents the initial Pd wire diameter (25.4 μ m). Table 2.2 lists the range of two rates limited by the current lab instruments. It is found that ϕ_d is more sensitive to the feeding rate.

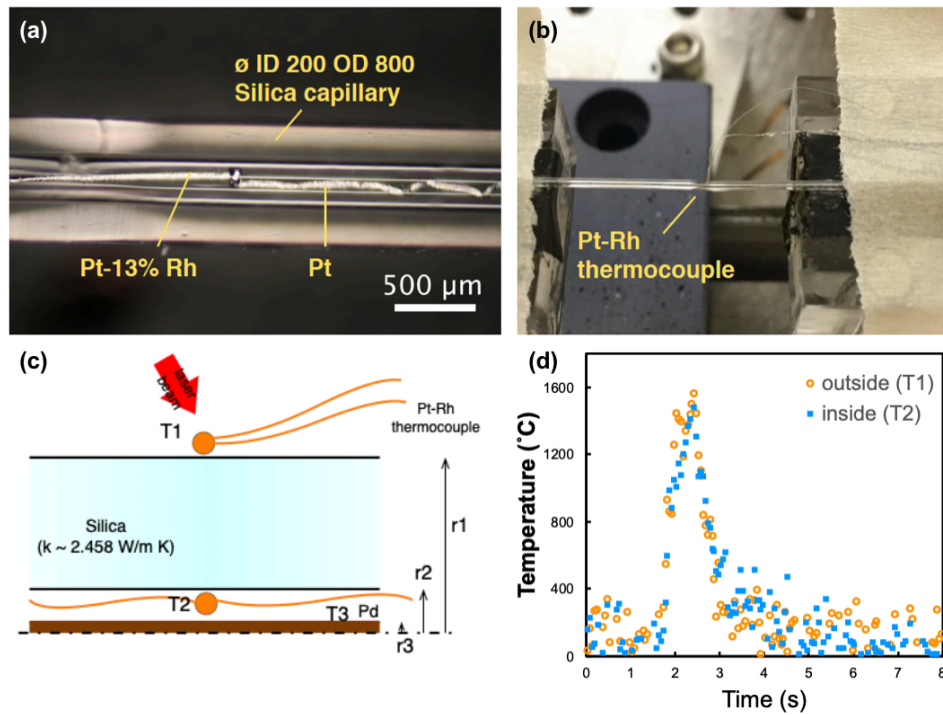


Figure 2.6 Measurement of preform temperature change in the LDC process. (a) OM image of a Pt-Ph thermocouple inserted inside of silica capillary. (b) A Pt-Ph thermocouple sits on the capillary outer wall. (c) Schematic of temperature measurement. (d) Measured heating and cooling profiles of the capillary outer and inner wall temperature.

With all the above drawing parameters, the LDC proceeds as illustrated in Figure 2.7. Typically, a single LDC process lasts less than 10 s and produces ~ 500 mm Pd-silica fiber with reduced diameters (limited by the maximum speed of our current linear actuator). The highest aspect ratio wire obtained has 140 mm length and a diameter below 200 nm (aspect ratio exceeding 10^5) encapsulated in the silica mold. Figure 2.8 shows the conical shape silica capillary with the reduced inner and outer diameters, as well as the as-drawn Pd-silica core-shell cross section.

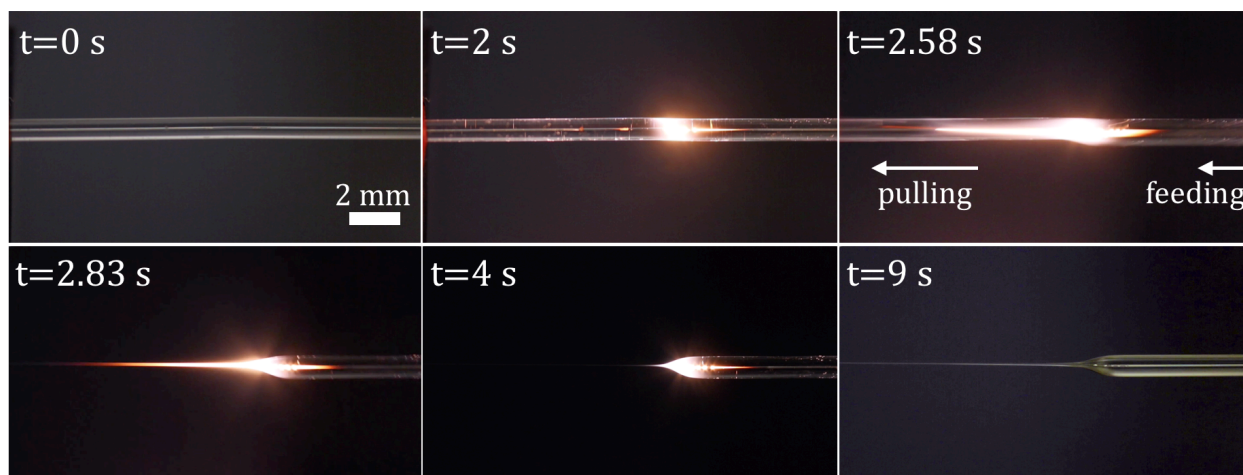


Figure 2.7. Snapshots of a Pd-silica preform deformation in LDC process. Drawing rate 400 mm s^{-1} , feeding rate 0.3 mm s^{-1} .

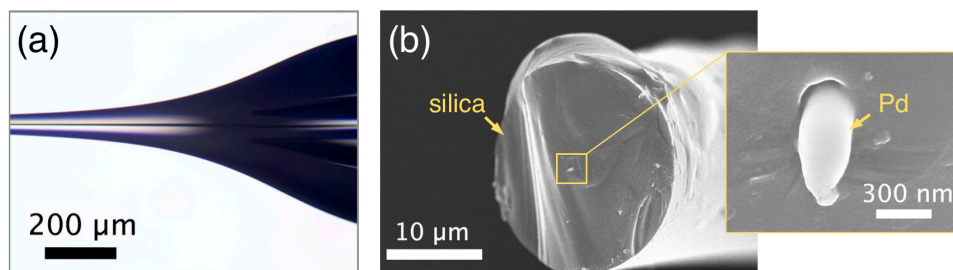


Figure 2.8. (a) OM image of the reduced area in the drawn capillary meniscus with the Pd core. (b) SEM images show the cross section of the as-drawn Pd-silica core-shell structure.

2.2.2. Structural characterization of as-drawn Pd nanowires

As-drawn Pd nanowires can be transferred to a desired substrate by removing the silica encapsulation by hydrofluoric acid (HF) etching. To be specific, the drawn Pd-silica fibers are firstly laid on the Si or HF resistant polymer (e.g. VHB substrate). 10 vol.% HF solution was then dropped on the substrates for SiO₂ etching. Depending on the HF etch rate and thickness of the silica mold, the etching time varies from 4 to 6 hours at room temperature. The exposed bare Pd wires sit on the substrate and then rinsed by D.I. water and methanol. Figure 2.9a shows a typical as-drawn Pd wire laid on a Si substrate. Since we use a linear stage of fixed travel length, the conical shape of silica mold is transferred to the drawn Pd wire leading a tapered morphology with negligible surface roughness. For the shown wire, the diameter varies from 1203 to 180 nm over 3.75 mm length along the wire, indicating $\sim 2.73 \text{ \AA}\mu\text{m}^{-1}$ taper angle and aspect ratio of 10^4 . The detailed microscopic morphologies at different positions of the wire are illustrated in Figure 2.9b.

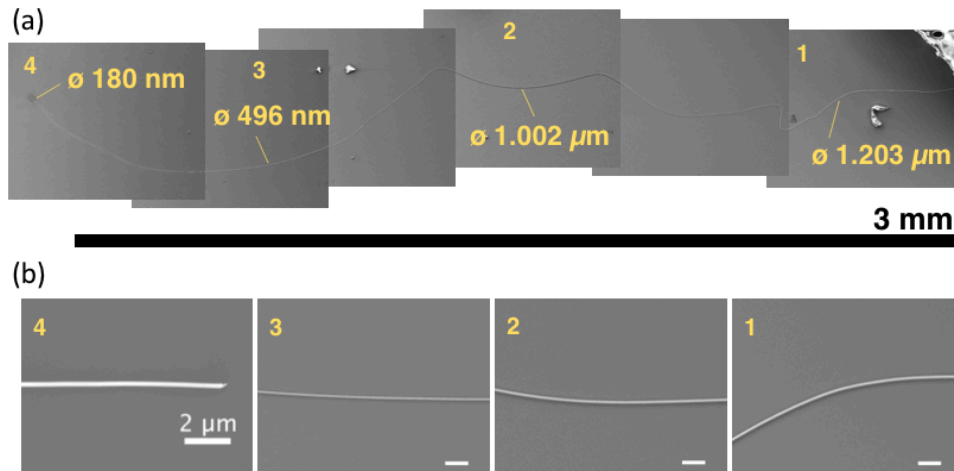


Figure 2.9. Stacked SEM images of as-drawn Pd wires. The silica mold is removed by etching in HF and single bare Pd wire lies on the Si substrate.

During the drawing process, a decrease in the inner diameter of the capillary takes place downstream of the laser spot, where the temperature is the highest. The mass conservation ($\phi_d = \phi_i \sqrt{\frac{v_f}{v_d}}$) suggests we can vary drawing and feeding rates to tune the final Pd diameter. Comparing two derivatives of the mass conservation relation ($\left. \frac{\partial \phi_d}{\partial v_d} \right|_{v_d} = -\frac{1}{2} \phi_i \sqrt{v_f} \left(\frac{1}{v_d} \right)^{1.5}$ and $\left. \frac{\partial \phi_d}{\partial v_f} \right|_{v_f} = \frac{1}{2} \phi_i \sqrt{\frac{1}{v_d}} \left(\frac{1}{v_f} \right)^{0.5}$), we know that the preform feeding rate strongly affects the wire diameter and we verify this in the experiments. As presented in Figure 2.10, the silica meniscus length L_m , which denotes the distance from where the necking starts to where the silica dimensions are frozen, decreases with the lower v_f . As a result, the inner diameter of the capillary gets smaller with low preform feeding, leading to the thinner Pd wires. Therefore, the diameter of the drawn Pd wires can be precisely controlled by the drawing parameters.

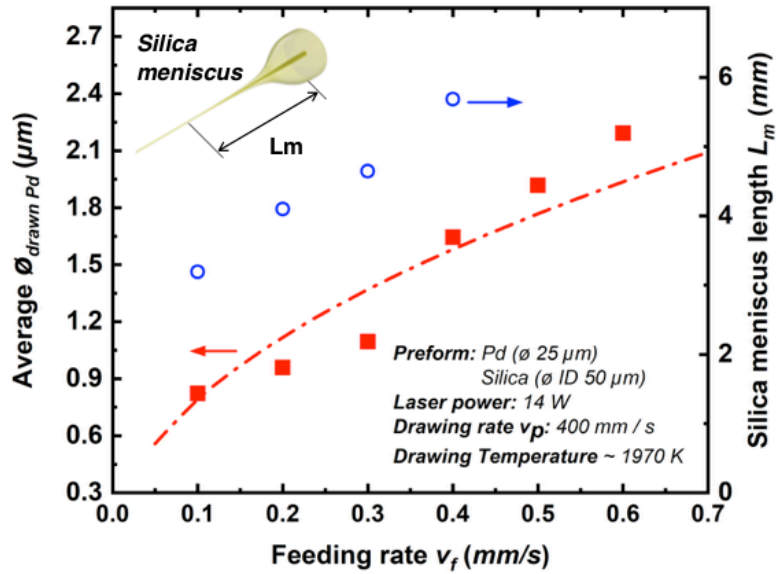


Figure 2.10. Measured Pd diameter and silica tapered meniscus length as a function of varying

the feeding rate. The red dashed line presents the mass conservation relation: $\phi_d = \phi_i \sqrt{\frac{v_f}{v_d}}$.

The mechanical, conductive and catalytic properties of as-drawn Pd wires strongly depends on their microstructures. We use the electron back scattering diffraction (EBSD) to trace the crystalline structure change before and after LDC process. SEM and EBSD images in Figure 2.11a present the polycrystalline structure across the initial Pd wire's cross section. The grain size is below 20 μm . This is not surprising since these Pd microwires are fabricated by the traditional cold drawing process. In contrast, as-drawn Pd nanowire shows the reconstruction of crystals spanning the entire cross section of the wire, forming a bamboo-shaped grain structure. Under current LDC working conditions, as-drawn Pd nanowire has large crystalline structure over 80 μm in length, as shown in Figure 2.11b.

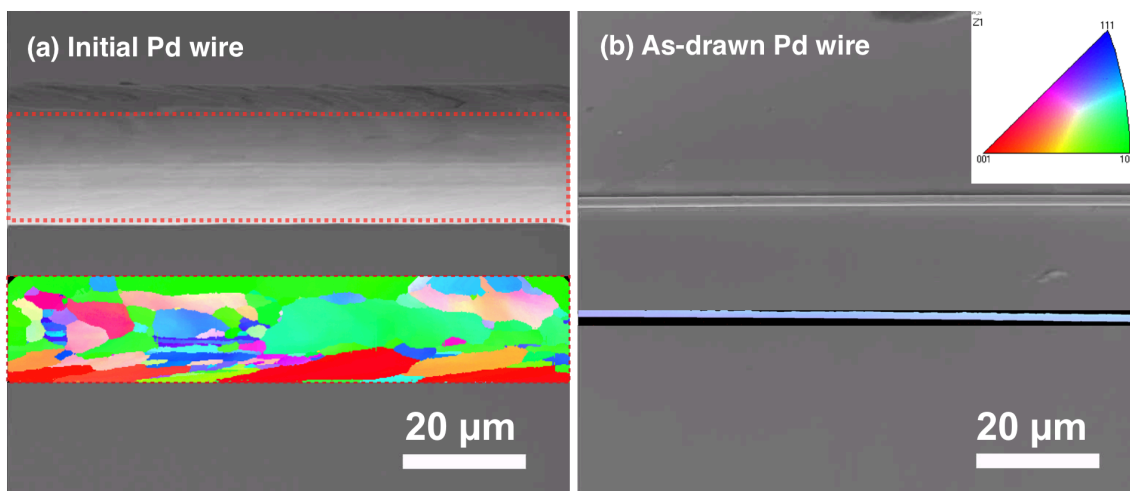


Figure 2.11. EBSD indicates the polycrystalline microstructure in the initial Pd microwire (\varnothing 25.4 μm) and as-drawn long single crystal Pd wire (\varnothing ~ 2 μm).

We further test the conductive and mechanical property enhancement due to the reconstruction of crystalline structure in as-drawn Pd wires:

- Firstly, we measure the electron transport in as-drawn Pd wires using the four-probe method. As shown in Figure 2.12, we observe that the electrical conductivity of Pd wires

drops by 15.5 % while the diameter decreases by 98.8 %. The conductivity of a drawn Pd wire with average diameter of 1.26 μm is ten times higher than that of the best single-walled CNT bundle¹⁸ (made from wet spinning) and 100 times higher than that of the high quality aligned multi-walled CNT films.¹⁹

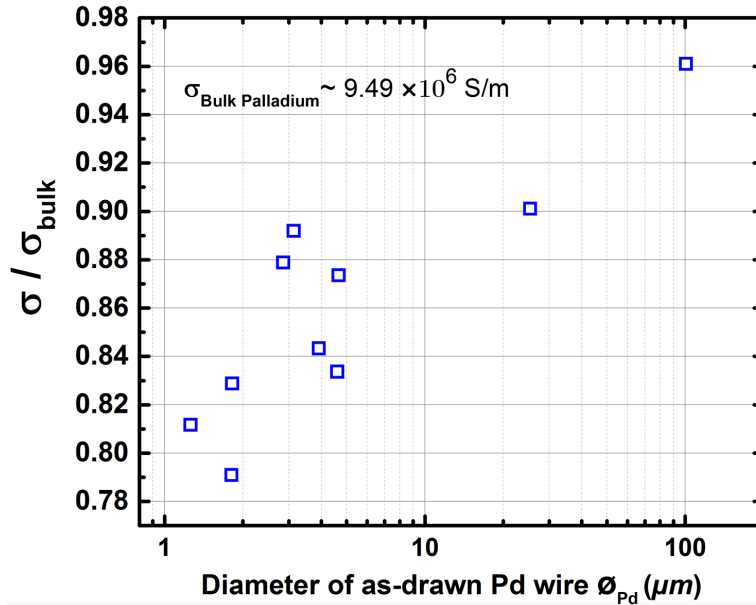


Figure 2.12. Dependence of relative change in electrical conductivity of as-drawn Pd wires on the average wire diameter ranging from 1 to 100 μm . Notably, the drawn Pd wires are tapered and the reported average wire diameter is measured in the middle of the length.

- Second, we indirectly examine the mechanical behaviors of as-drawn Pd nanowires by studying the in-plane buckling. In this study, 3M VHB (very high bonding) tapes are used as the flexible substrate because they are transparent and can accommodate uniaxial pre-strain over 800 % without tearing. The drawn Pd-silica fibers are laid and aligned on the pre-stretched VHB substrate, followed by etching the silica by HF. VHB tape is notably resistant to HF. After removing the silica mold, bare Pd nanowires are deposited on VHB substrate. We hereby slowly release the pre-strain in VHB and indirectly apply

compressive stress on Pd nanowires, as sketched in Figure 2.13a. Qualitatively, when the compressive strains on the concave side of a slender buckling element exceeds the elastic strain limit, a plastic hinge is formed while the modulus is effectively reduced, following the decrease of the stress-strain slope post-yielding. Here, as displayed in Figure 2.13b and 2.13c, the effective modulus of the Pd wire evolves as the VHB substrate is released in inelastic buckling stage, and it is a function of both the pre-strain in VHB and instantaneous strain in the wire. The formation of plastic hinges shown in Figure 2.13c is associated with energy dissipation, and the straightening of the wire profile from a sinusoidal geometry to straight beams connected by a small radius elastic hinge.

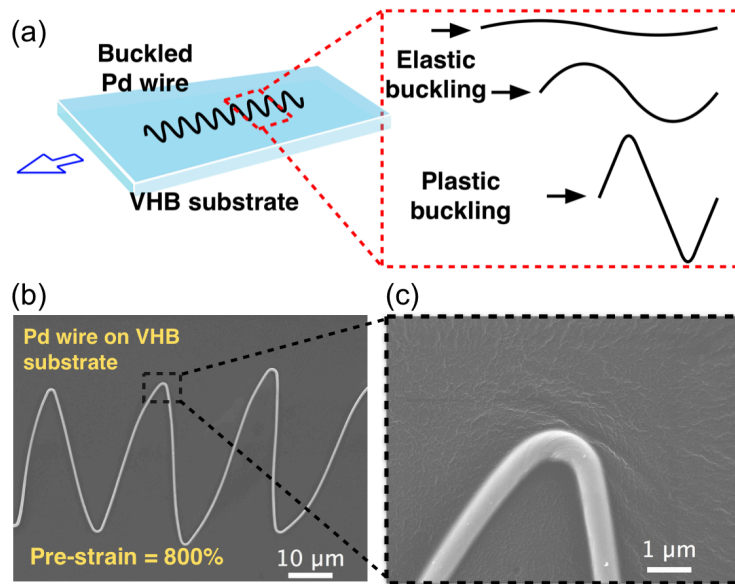


Figure 2.13. (a) Schematic of buckling of a Pd wire on a pre-strained VHB substrate transitioning from sinusoidal elastic buckling to inelastic buckling patterns at higher pre-strains. (b) SEM image of a buckled Pd wire on VHB with pre-strain of 800 %. (c) A zoomed-in SEM image showing the plastic hinge on Pd wire.

2.3. Conclusions

In summary, we developed a new fabrication process for the centimeter-long Pd micro and nanowires. This novel LDC process can also enable the fabricate of a variety of metal wires for a wide range of applications, and due to its high drawing rates ($\sim\text{m s}^{-1}$), is suitable for high throughput production. Geometries of as-drawn metal wires are tunable by controlling the preform properties and process parameters. A 140 mm-long silica-coated Pd wire with diameter downsized to 250 nm was obtained in this study, achieving an aspect ratio of $> 10^5$. According to our experiments and calculations, the diameter scales inversely with the drawing speed, and we are expected to achieve wires of 10 nm at a drawing speed of 5 m s^{-1} and higher laser power. As-drawn Pd wires have large crystalline structures ($>80 \mu\text{m}$) which span across the whole wire thickness. This bamboo-shaped crystalline structure significantly reduces the electron scattering at grain boundaries therefore significantly enhances the electrical conductivity at the nanoscales. In addition, we demonstrated as-drawn Pd wires' integration in a highly stretchable conductor which can be strained up to 800 % without failure. We believe that the ultralong ultra-high-aspect-ratio metal nanowires fabricated by LDC are promising for applications in flexible and wearable electronics. Importantly, they provide a proper platform for fundamental metallurgical and catalytic studies of low dimensional structures.

2.4. References:

1. Donald, I. W. *Journal of Materials Science* **1987**, 22, (8), 2661-2679.
2. Wiley, B. J.; Wang, Z.; Wei, J.; Yin, Y.; Cobden, D. H.; Xia, Y. *Nano Lett* **2006**, 6, (10), 2273-8.
3. Menke, E. J.; Thompson, M. A.; Xiang, C.; Yang, L. C.; Penner, R. M. *Nature Materials* **2006**, 5, 914.
4. Xiang, C.; Yang, Y.; Penner, R. M. *Chemical Communications* **2009**, (8), 859-873.
5. Im, Y.; Lee, C.; Vasquez, R. P.; Bangar, M. A.; Myung, N. V.; Menke, E. J.; Penner, R. M.; Yun, M. *Small* **2006**, 2, (3), 356-358.
6. Greer, J. R.; De Hosson, J. T. M. *Progress in Materials Science* **2011**, 56, (6), 654-724.
7. Xu, Z.; Shen, C.; Sun, S.; Gao, H. J. *The Journal of Physical Chemistry C* **2009**, 113, (34), 15196-15200.
8. <http://novarials.com/ProductsAgNWsA70.html>.
9. Taylor, G. F. *Physical Review* **1924**, 23, (5), 655-660.
10. Bayindir, M.; Abouraddy, A. F.; Arnold, J.; Joannopoulos, J. D.; Fink, Y. *Advanced Materials* **2006**, 18, (7), 845-849.
11. Deng, D. S.; Orf, N. D.; Danto, S.; Abouraddy, A. F.; Joannopoulos, J. D.; Fink, Y. *Applied Physics Letters* **2010**, 96, (2), 023102.
12. Kaufman, J. J.; Tao, G.; Shabahang, S.; Banaei, E.-H.; Deng, D. S.; Liang, X.; Johnson, S. G.; Fink, Y.; Abouraddy, A. F. *Nature* **2012**, 487, 463.
13. Percival, S. J.; Vartanian, N. E.; Zhang, B. *RSC Advances* **2014**, 4, (21), 10491-10498.
14. Larin, V. S.; Torcunov, A. V.; Zhukov, A.; González, J.; Vazquez, M.; Panina, L. *Journal of Magnetism and Magnetic Materials* **2002**, 249, (1), 39-45.
15. Sørensen, H. L.; Polzik, E. S.; Appel, J. J. *Lightwave Technol.* **2014**, 32, (10), 1886-1891.
16. Romaniuk, R. *Bulletin of The Polish Academy of Sciences: Technical Sciences* **2008**, 56, (2).
17. McLachlan, A. D.; Meyer, F. P. *Appl. Opt.* **1987**, 26, (9), 1728-1731.
18. Behabtu, N.; Young, C. C.; Tsentlovich, D. E.; Kleinerman, O.; Wang, X.; Ma, A. W. K.; Bengio, E. A.; ter Waarbeek, R. F.; de Jong, J. J.; Hoogerwerf, R. E.; Fairchild, S. B.; Ferguson, J. B.; Maruyama, B.; Kono, J.; Talmon, Y.; Cohen, Y.; Otto, M. J.; Pasquali, M. *Science* **2013**, 339, (6116), 182.
19. Tawfik, S.; O'Brien, K.; Hart, A. J. *Small* **2009**, 5, (21), 2467-2473.

CHAPTER 3: FABRICATION OF HIGH-QUALITY GRAPHENE-METAL NANOCOMPOSITES VIA CVD SYNTHESIS

Abstract:

Manufacturing of high performance graphene-based composite materials requires high-quality graphene sheets. Extensive efforts have been invented in synthesizing large-area high-quality graphene mono and bilayer, however, graphene synthesis mechanisms are usually overlooked in assembling the macroscale graphene-based composite materials. High-quality graphene synthesis on the nanoscale metal catalysts is expected to offer insights that links the atomic-level graphene formation mechanisms to the larger scale integration of the graphene the metallic matrices in a graphene-metal composite. In this chapter, we use a model system of ultrathin metal films to study the graphene synthesis mechanisms in chemical vapor deposition (CVD) processes. A dynamic and kinetic model of carbon segregation and precipitation in graphene nucleation in CVD is proposed and guides a highly dynamic rapid CVD recipe for high-quality graphene monolayer growth on ultrathin metal films.

3.1. Chemical vapor deposition synthesis with ultrathin metal films

3.1.1. Selection of metal catalysts for graphene synthesis

There are extensive studies on synthesizing large-area high-quality graphene sheets on bulk metal catalyst via CVD.¹⁻⁵ Several transition metals can be used as the catalytic materials. They can be basically grouped into two broad types: Group 1: metals having low solid carbon solubility and low graphene-metal binding energy (e.g. the Cu and Pt group); and Group 2: metals having high solid carbon solubility and strong graphene-metal binding energy (e.g. the Ni and Pd group). Metal

catalysts from Group 1 offer self-limited monolayer graphene synthesis by surface adsorption and therefore are suitable for obtaining single layer graphene by carefully controlling the carbon deposition rate. The synthesis on Cu and Pt proceeds by slow isothermal adsorption at high temperature (normally > 1000 °C), and the metal catalyst is typically chemical etched to release the graphene monolayer and transfer it to target substrates.^{1, 6} In this study, we mainly focus on synthesis with Group 2 materials for the following reasons: (i) our focus is the pristine graphene-metal interface right after graphene formation in CVD, therefore, strong binding energy between seed metal and graphene sheet is required; (ii) the metal catalysts at the nanoscales are highly unstable at synthesis temperatures in CVD, as a result, we need a highly active catalyst for extremely rapid synthesis before nanoscale metal substrate degrades. We summarize the commonly used transition metals and their properties associated with the interaction with graphene in Table 3.1. Ni and Pd exhibit high binding energy and low separation distance to the graphene as well as high carbon solubility at high temperatures, which make them promising candidates for graphene-metal nanocomposites. In the rest of this chapter, we will focus on the CVD syntheses on Ni and Pd.

Table 3.1. Selection of metal catalyst for CVD synthesis^{7, 8}

Gr-metal	Lattice spacing (111)	Lattice mismatch	Binding energy (meV at. ⁻¹)	C-metal separation (Å)	Adhesion energy (J m ⁻²)	Melting point (°C)	Carbon solubility at 1000 °C	Interaction
Gr-Gr	2.461	0	0.5	3.34	0.35			↓
Gr-Cu	2.543	4.07 %	33	3.3	12.8	1085	0.04	↓
Gr-Pt	2.766	2.24 %	38	3.3		1768	1.76	↓
Gr-Ni	2.474	1.22 %	125	2.1	72.7	1395	2.03	↑
Gr-Pd	2.729	-3.36 %	84	2.5		1554	5.98	↑

3.1.2. Kinetics of carbon segregation and precipitation in CVD processes

In general, graphene growth on Group 2 metals can be implemented by carbon diffusion and precipitation during heating and cooling in hydrocarbon environment. This features in Group 2 metals leads to the synthesis of high-quality graphene monolayer by a highly dynamic recipe within a growth time of less than a minute. In this chapter, we use a transfer arm to load and unload metal catalyst films having thickness of h in a high temperature furnace to achieve the quick temperature change and drive the carbon atoms segregation in the catalyst, as sketched in Figure 3.1a. We analyze the kinetics of graphene formation on Group 2 metals using a simplified model shown in Figure 3.1b, based on the following assumptions:

- At synthesis temperatures, hydrocarbon precursors like CH_4 quickly decompose into carbon species (CH_x) and carbon radicals readily dissolve into metal catalyst due to their lower chemical potential in bulk metal than that on the surface.⁹ Carbon concentration on metal surface is mainly determined by the concentration of hydrocarbon (c_g);
- Gas flows in the furnace reach the steady state before the catalyst is loaded. A boundary layer with an average thickness of $\langle\delta\rangle$ is established on the metal surface. c_g is constant in the steady state flow and can be controlled by precursors flow rates (e.g. CH_4 and He);
- The metal catalyst has a finite thickness of h , while the back side is not exposed to carbon precursor.
- The carbon solubility limit in catalyst is defined as the maximum carbon concentration

$$c_{max} = S_0 \exp\left(-\frac{H_0}{RT}\right).^{10}$$

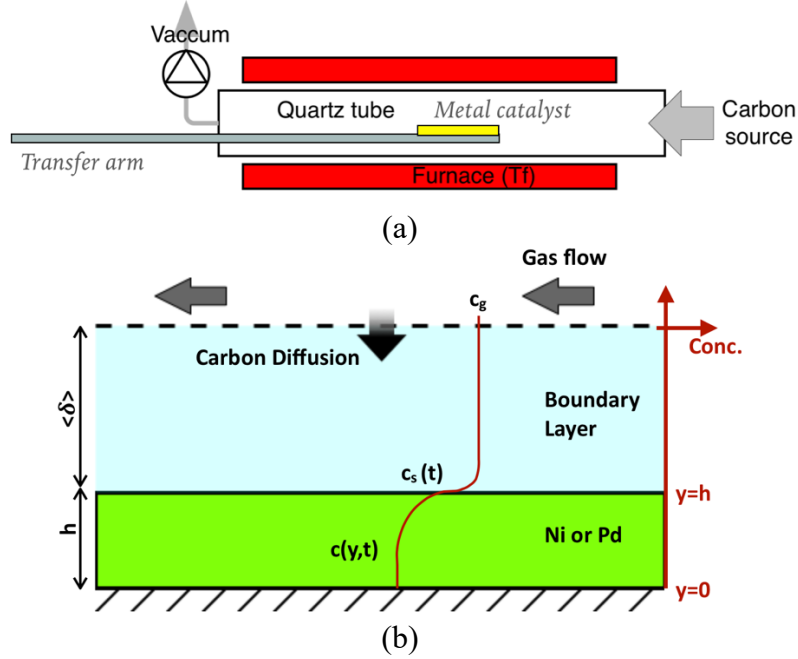


Figure 3.1. (a) Schematic diagram of low pressure CVD. (b) Illustration of diffusion-mediated graphene formation model on Group 2 metals.

In Figure 3.1b, diffusion coefficient of carbon precursor in the gas domain (e.g. $D_g \sim 10^{-4} \text{ m}^2 \text{ s}^{-1}$) is much higher than that of carbon in the metal (e.g. $D_{\text{Pd}} \sim 10^{-10} \text{ m}^2 \text{ s}^{-1}$) at synthesis temperature (~ 1100 °C), as a result, interfacial concentration c_s on catalyst surface is more sensitive to c_g than the diffusion in catalyst. It is safe to use c_s as a boundary condition, e.g. $c_s \approx c_g$. Considering the above assumptions, 1D Fick's 2nd law can be applied to metal domain:

$$\frac{\partial c}{\partial t} = D \frac{\partial^2 c}{\partial y^2} \quad (3.1)$$

The initial condition: $c(y, t = 0) = c_0$

The boundary conditions: $c(y = h, t) = c_s$ and $\frac{\partial c}{\partial t}(y = 0, t) = 0$

$$\text{Using Laplace transforms:}^{11} \frac{\partial^2 \hat{c}}{\partial y^2} - \frac{p}{D} \hat{c} = -\frac{c(y, t=0)}{D} = -\frac{c_0}{D} \quad (3.2)$$

B.C.: $\hat{c}(y = h, p) = \frac{c_s}{p}$ and $\frac{\partial \hat{c}}{\partial y}(y = 0, p) = 0$ and I.C.: $\hat{c}(y, p = 0) = \frac{c_0}{p}$

We can then solve Equation (2): $\hat{c} = \frac{c_s}{(e^{qh}+e^{-qh})p} e^{qy} + \frac{c_s}{(e^{qh}+e^{-qh})p} e^{-qy} + \frac{c_0}{p}$, $q \equiv \sqrt{\frac{p}{D}}$ (3.3)

Expand the denominator with Laurent series: $\hat{c} = \frac{c_0}{p} + c_s \sum_{n=0}^{\infty} (-1)^n \left\{ \frac{e^{-q[(2n+1)h-y]}}{p} + \frac{e^{-q[(2n+1)h+y]}}{p} \right\}$ (3.4)

Take the inverse transform on Equation (4) with $\mathcal{L}^{-1} \left\{ \frac{e^{-qx}}{p} \right\} = \text{erfc} \left(\frac{x}{\sqrt{4Dt}} \right)$:

$\Rightarrow c(y,t) = c_0 + c_s \sum_{n=0}^{\infty} (-1)^n \left\{ \text{erfc} \left(\frac{(2n+1)h-y}{\sqrt{4Dt}} \right) + \text{erfc} \left(\frac{(2n+1)h+y}{\sqrt{4Dt}} \right) \right\}$ (3.5)

Equation 3.5 describes the carbon concentration distribution change in metal catalyst with time and the given boundary condition c_s . Notably, D is the carbon diffusion coefficient in catalyst, which is temperature dependent: $D_{pd}(T) = D_0 \exp \left(-\frac{E_0}{RT} \right)$. D_0 is a diffusion prefactor $\sim 10^{-4.7} \text{ m}^2 \text{ s}^{-1}$ for Pd and $2.48 \times 10^{-4} \text{ m}^2 \text{ s}^{-1}$ for Ni, E_0 is the activation energy $\sim 132 \text{ kJ mol}^{-1}$ for Pd and 168 kJ mol^{-1} for Ni.^{10, 12} Limited by metal instability at extremely high temperatures, which will be discussed soon in this chapter, temperature change in catalyst with time after loading into the hot zone has to be taken into consideration. We can herein rewrite the carbon concentration distribution expressed in Equation 3.5 as a function of growth time t_g and precursor concentration c_g . Figure 3.2a gives a typical furnace temperature (T_f) and precursor flow rate (c_s) profiles during CVD process. Metal catalyst is supported on the arm and inserted into hot zone after the furnace temperature T_f stabilizes at synthesis temperature (e.g. $1100 \text{ }^\circ\text{C}$). Catalyst dwells for a short period of time (t_g), then rapidly cools down by retracted out of the hot zone. The heating in catalyst can be easily simulated in COMSOL Conjugated Heat Transfer Module,¹³ hence the transient temperature variance (T_s) with the dwelling time in furnace (t_g) on metal surface can be estimated, as shown in Figure 3.2b. This growth time dependent temperature in catalyst can in turn be used

to calculate the transient carbon diffusion coefficient in Equation 3.5. In experiments, c_g can be controlled by flow rates of precursors, e.g. $(\text{CH}_4:\text{He})_g$ (g: growth).

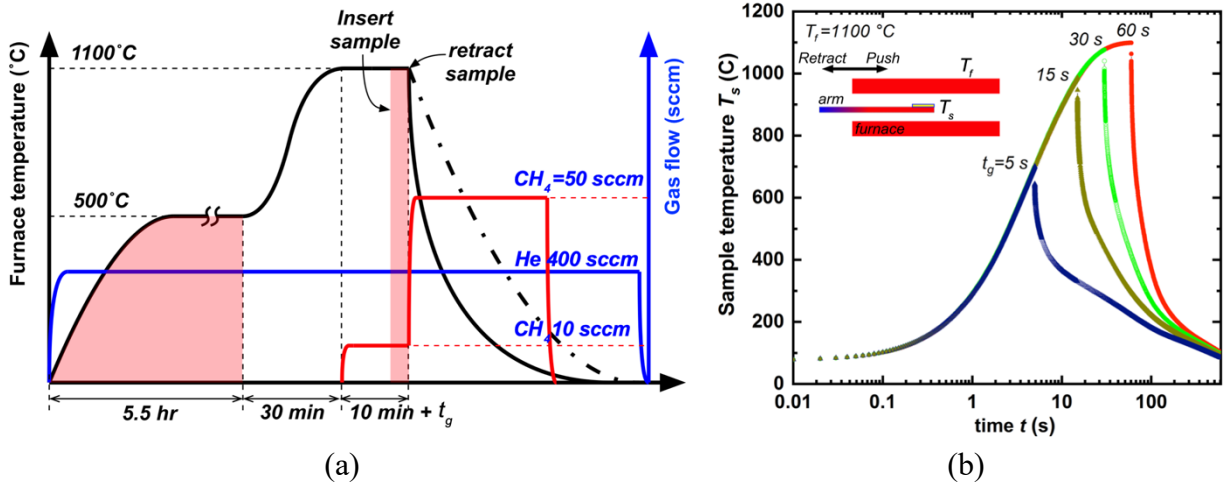


Figure 3.2. (a) Typical temperature ramp and gas flow profiles of carbon precursor during CVD process. (b) COMSOL simulated temperature profiles on metal catalyst during CVD process.

First, we analyze the carbon distribution during heating process. Figure 3.3a displays the calculated carbon concentration $c(y, t)$ (at%) using analytical solution in Equation 3.5 for a thin Pd film at 1100 °C with the gas mixtures: $(\text{CH}_4:\text{He})_g = 10:400, 20:400,$ and $50:400$ sccm. In addition, numerical simulations using COMSOL Chemical Reaction Module¹⁴ help to confirm that, since the diffusion in gas boundary layer is much faster than that in Pd, it is reasonable to assume $c_s \approx c_g$ on Pd surface. The numerical simulations, displayed in solid lines in Figure 3.3a vary from analytical calculations at the onset of heating due to the consideration of diffusion through the gas boundary layer, but asymptotically converge after longer heating duration. Notably, with all hydrocarbon concentrations used, $c_s < c_{max}$, indicating that the non-saturation of the catalyst with carbon during heating. Specially, cooling is crucial for graphene formation in Gorup 2 catalysts. Similar to heating, we study the cooling process using both numerical simulations and analytical solution to estimate the temperature and diffusion kinetics. We simulate the retraction of the Pd

catalyst out of the hot zone after a certain growth time (here, $t_g = 30$ s). The numerical simulations indicate the presence of three main scenarios of carbon segregation kinetics depending on the hydrocarbon concentration c_g during cooling:

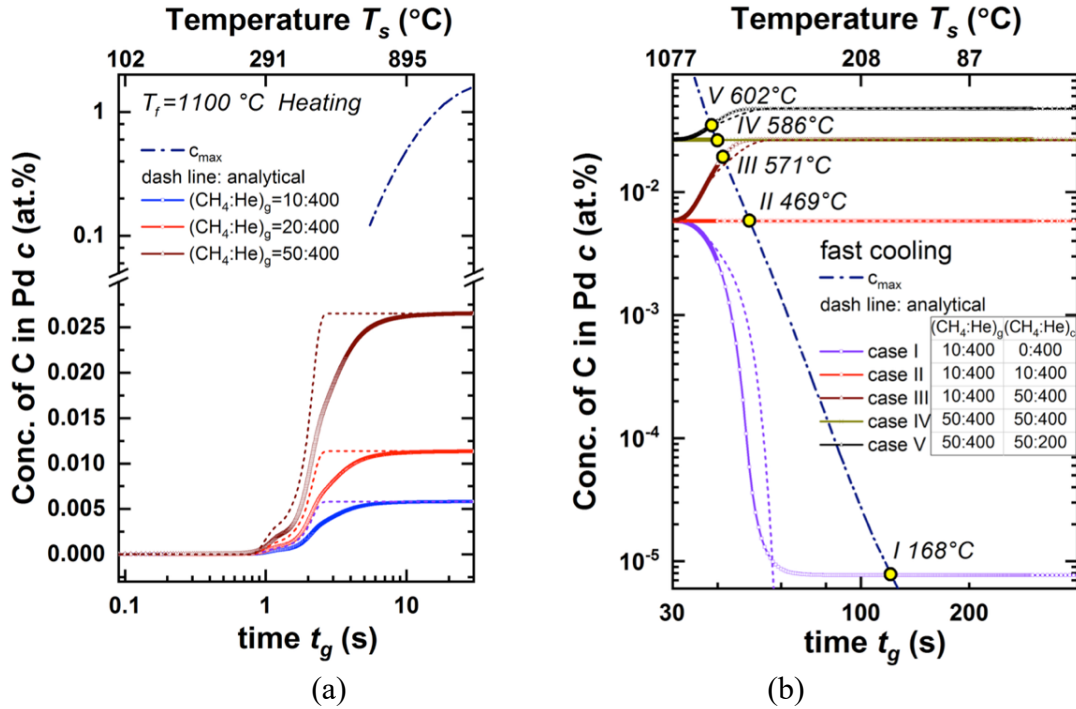


Figure 3.3. Simulated concentration of dissolved carbon in Pd catalyst during (a) heating and (b) cooling steps in CVD process.

Scenario I: the hydrocarbon gas is shut down during cooling $(CH_4: He)_c = 0: 400$ sccm (c: cooling). In this case, shown in Figure 3.3b case I, c_g and c_s drop quickly and an outward diffusion flux J'_d drives the diffusion of carbon on Pd surface. The large amounts of segregated carbon reach the critical concentration for graphene nucleation and growth.^{15, 16}

Scenario II: the hydrocarbon concentration is maintained at the same value during heating and cooling processes $(CH_4: He)_c = 10: 400$ sccm. Shown in Figure 3.3b case II, under this condition, $c(y, t)$ remains approximately constant during cooling due to the absence of concentration gradient.

The onset of graphene nucleation is delayed due to the insufficient carbon concentration in the absence of flux J'_d . There is an “incubation” period of low carbon concentration c_s on Pd surface as cooling starts. Importantly, as T_s drops, the solubility c_{max} also decreases, eventually meets and becomes less than c_s , which can trigger the segregation of carbon to Pd surface and then boosts the graphene nucleation (see yellow intersection points in Figure 3.3b). The difference in graphene formation between (I) and (II) can be attributed to the low carbon agglomeration rate J'_d by diffusion and high precipitation rate $J_{prec.}$ by precipitation.

Scenario III: the hydrocarbon concentration increases when cooling starts. $(CH_4: He)_c = 50: 400$ sccm and c_s becomes higher during cooling than during the heating step. This increase drives an additional inward carbon flux J''_d during cooling. Consequently, $c(y, t)$ rises and meets the solubility limit earlier. Compared to (I) and (II), higher $c(y, t)$ in cooling step shortens the incubation period of the carbon atoms on Pd surface and initiates graphene nucleation and growth at higher temperature, hence results in higher graphene crystallinity.¹⁷ This interesting observation implies that for Group 2 catalysts, the onset of growth during cooling can be precisely controlled by the hydrocarbon gas flows.

Notably, if the cooling rate varies, the same scenarios generally persist. Figure 3.4a depicts the simulated T_s profiles with the different cooling rates at the onset of cooling step ($t_g = 30$ s). Slow cooling delays the saturation of the Pd with carbon, as demonstrated by the delayed intersections between $c(y, t)$ and c_{max} curves in Figure 3.4b. This suggests that low cooling rate leads to longer carbon incubation time and lower graphene nucleation temperature. Based on these modeling results, it is expected that high carbon precipitation flux $J_{prec.}$ at high temperature is the

key to obtain controllable growth of graphene monolayer with high crystallinity. In the rest of this chapter, we will validate the aforementioned kinetic model in experiments.

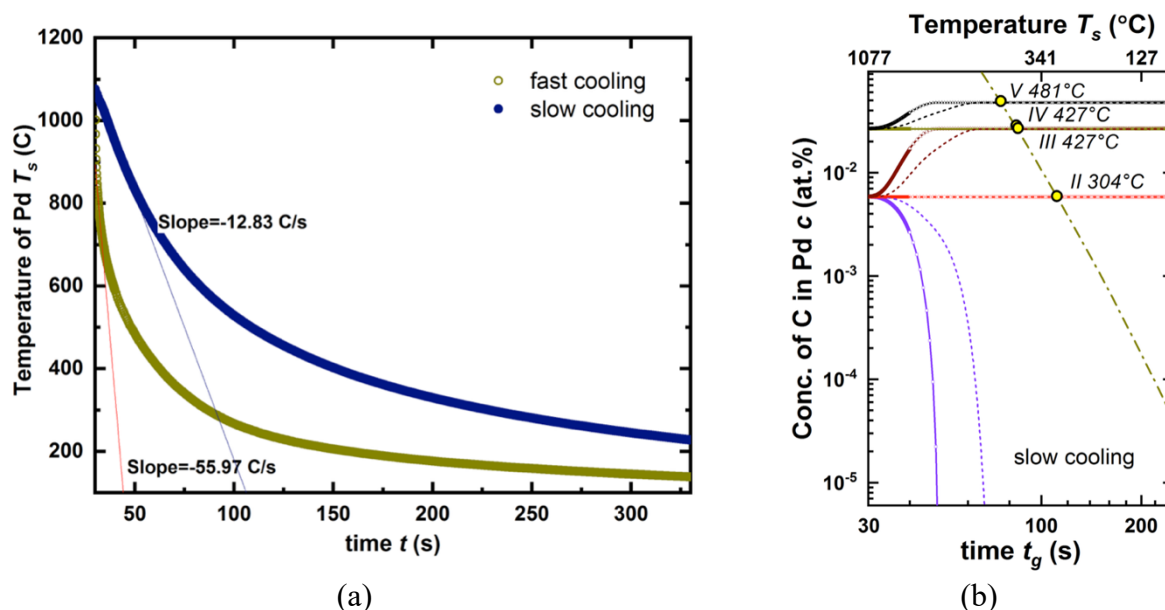


Figure 3.4. (a) COMSOL simulated temperature profiles in cooling step in CVD process. (b)

Simulated concentration of dissolved carbon in Pd with slow cooling.

3.1.3. Experimental implement

Experimental validations of the proposed synthesis mechanisms with Group 2 catalysts are conducted using a home-built tube furnace, as shown in Figure 3.5. A quartz tube (Technical Glass Products) having diameter of 50.8 mm and length of 760 mm is used as the chamber. A gradient tube furnace (Carbolite EZS-3G) heats and maintains the tube at synthesis temperatures. The tube is pumped by a mechanical pump (Kurt J. Lesker, 221C2MLAN) and kept under vacuum during synthesis. The catalyst is supported on a transform arm (Kurt J. Lesker, Elevating PowerPorbe EPP40), which can load and retract the sample in the hot zone under vacuum.

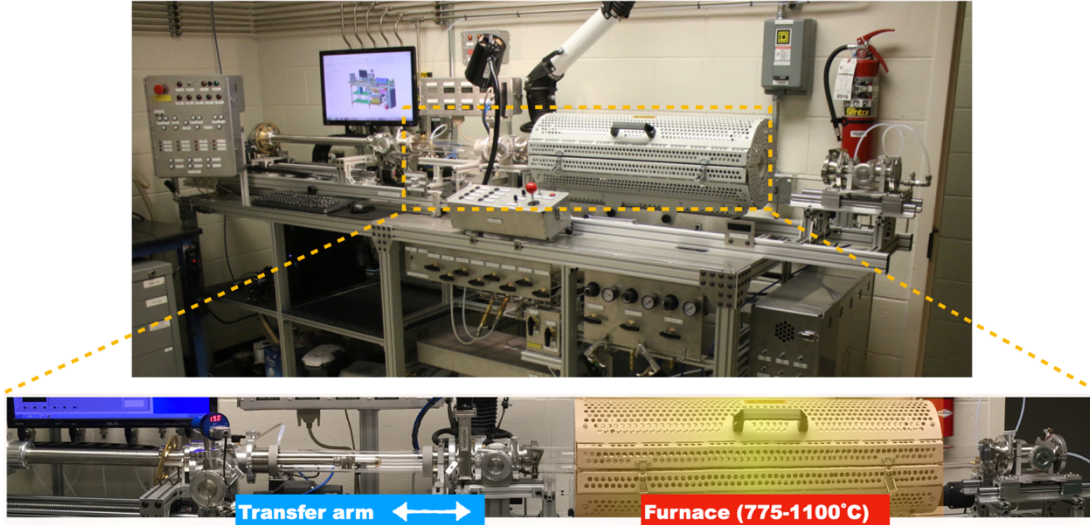


Figure 3.5. Experimental setup of low pressure CVD system.

As-grown sample is characterized using Scanning Electron Microscope (SEM, JEOL 7000F), Transmission Electron Microscope (TEM, JEOL 2100 Cryo), Optical microscope (Zeiss AXIO Imager.A2m) and Raman spectroscopy (Horiba Raman Confocal Imaging Microscope).

3.2. Graphene synthesis on nano-grain ultrathin metal films

3.2.1. Solid-state dewetting of metal catalysts in CVD

It is challenging to grow uniform and high-quality monolayer graphene on nanoscale metal catalysts. Specifically, metal catalysts with nanoscale dimensions, although having high melting temperatures, tend to minimize their free surface energy by dewetting or agglomeration and exhibit high instability at temperatures below their melting points. This is called solid-state dewetting and very common for small scale metals.¹⁸ Figure 3.6a sketches a deposited thin metal film on a substrate. Driven by several processes including grooving at its grain boundaries and triple junctions, hole formation, edge retraction and fingering instability, this thin metal film can break up and agglomerate into discrete islands at temperatures as low as one half of the melting

temperature of the corresponding bulk metal, as shown in Figure 3.6b. This dewetting challenges graphene synthesis since most CVD processes require long duration at extremely high temperatures which significantly exceed the onset of dewetting. For testing, a thin Pd film having thickness of 150 nm deposited by sputtering on a SiO₂/Si substrate is loaded to furnace at 1100 °C in vacuum. Figure 3.6c shows the dewetted Pd films after 60 s.

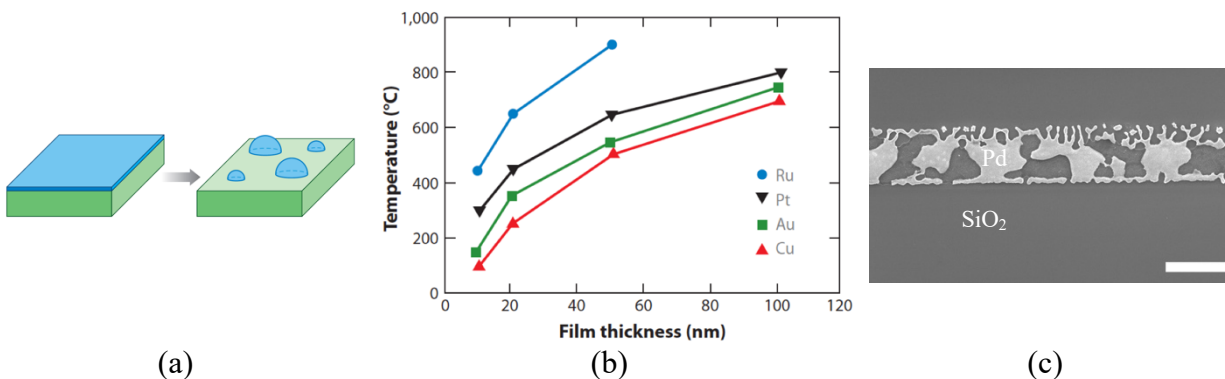


Figure 3.6. (a) Schematic of solid-state dewetting of thin metal film at temperatures much below its melting point.¹⁸ (b) Film thickness at which dewetting is observed as a function of annealing temperature for different metals.¹⁹ (c) SEM image of dewetting in sputtered Pd films (150 nm thin on the SiO₂/Si substrate). Scale bar: 10 μm.

Since hole formation in thin metal films will be most likely at high-energy grain boundaries,¹⁸ reducing the triple junction density in catalyst or lowering the synthesis temperature could help to avoid this solid-state dewetting. Under the sputtering conditions, for example, Ni: 150 W, 0.6 Ås⁻¹¹ and Pd: 70W, 0.7 Ås⁻¹, metal grain size is around tens of nanometer. Although grain structure can expand by annealing, nanoscale thickness of a thin film limits the grain growth once the columnar microstructure forms across the thickness.²⁰ Therefore, the sputtered thin metal films will have high triple junction densities.

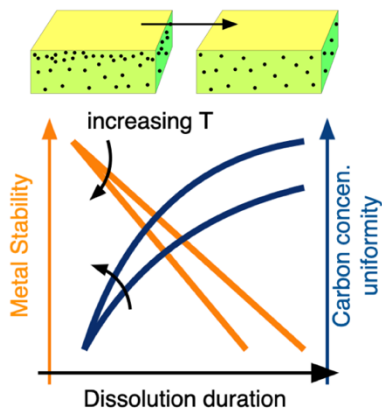


Figure 3.7. Synthesis strategy on ultrathin metal films.

We propose a generic graphene synthesis strategy for ultrathin metal catalysts with instabilities at high synthesis temperatures, as presented in Figure 3.7. Firstly, by decreasing the synthesis temperature or shortening the heating duration, nanoscale metal catalysts can maintain stable during CVD. However, the temperature-driven carbon segregation in this case is not sufficient resulting in non-uniform carbon distribution in the metal. According to theoretical analysis in the previous section, carbon uniformity in the catalyst is crucial for graphene nucleation. Therefore, low temperature CVD synthesis rarely give good control in graphene layers and quality.

3.2.2. Multilayer graphene synthesis on thin Ni films

We firstly verify the proposed strategy in Figure 3.7 for low temperature synthesis case. The sputtered thin Ni film is used due to its high binding energy to graphene, according to Table 3.1. Moreover, thin Ni film intrinsically has weak interfacial energy with SiO₂ hence the as-grown Ni-graphene composite film can easily delaminate and be transferred with water assistant.²¹ As-deposited Ni films with thickness of 155 nm have average grain size of 17.3 nm, as shown in Figure 3.8a and 3.8b. The Ni films are annealed at 775 °C in 60 sccm H₂ and 400 sccm He at 1.67

Torr for 30 min. During this step, the native oxide on the Ni surface is reduced while the Ni grains grow in size. The annealing step also decreases the bonding of Ni to the SiO₂ surface and facilitates film delamination after growth.

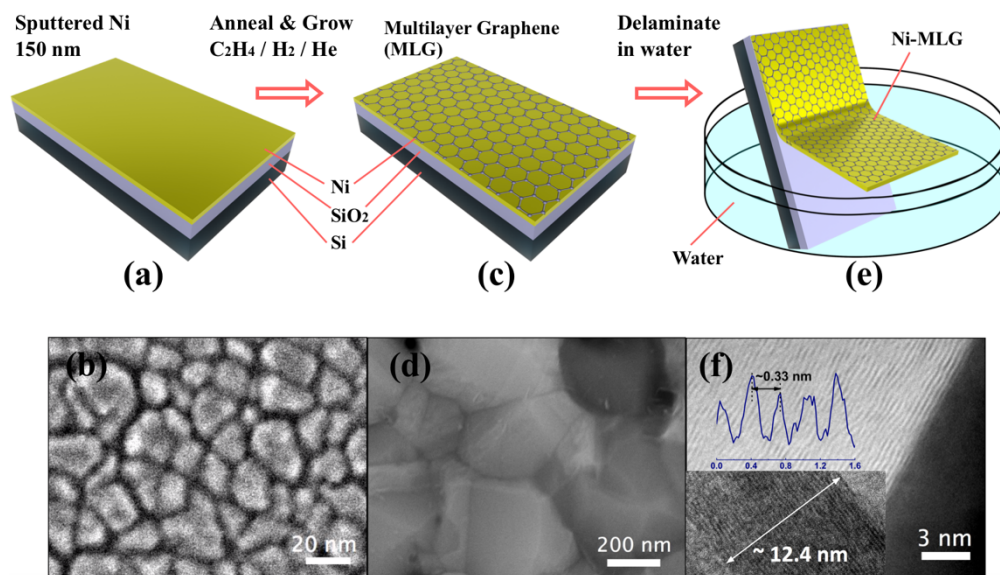
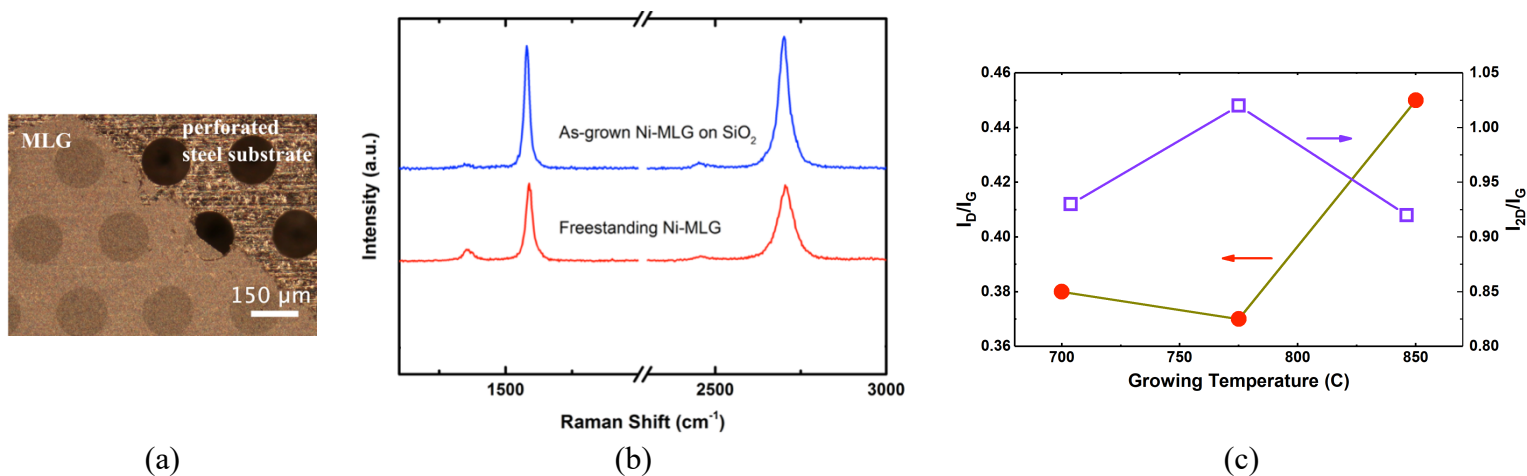


Figure 3.8. Synthesis MLG on thin Ni film. (a) Schematic of thin Ni film catalyst. (b) Schematic of as-grown Ni-MLG laminated structure. (c) Schematic of delaminated Ni-MLG film assisted by water. (d) SEM image of as-sputtered Ni film. (e) SEM image of as-grown Ni-MLG film. (f) TEM image of the Ni-MLG interface.

Since low synthesis temperature is used here, we flow C₂H₄, which has relatively low thermal decomposition temperature to increase the surface carbon concentration c_s . Graphene is synthesized by flowing 50 sccm C₂H₄ and 60 sccm H₂ at 775 °C and 460 mTorr for 10 minutes. Following this step, the tube is purged with 600 sccm He and the sample is then fast cooled to room temperature by retracting out of hot zone using the transfer arm. Figure 3.8c and 3.8d shows the structure and surface morphology of as-grown Ni-graphene film (referred to as-grown Ni-MLG) on substrate. Given a sufficient c_s on the Ni surface, the thickness of formed multilayer graphene

(MLG) can be simply controlled by growth time. Growth time of 1, 5, 10 and 20 minutes results in MLG thicknesses of 2.6, 7.8, 10.9 and 29.7 nm, respectively. Importantly, the Ni-MLG interface is uniform, with the MLG showing excellent conformability to the Ni grains as confirmed by TEM image in Figure 3.8f.

As-grown Ni-MLG films can be readily transfer to any substrate by slowly submerging into water. We can obtain freestanding MLG layer by etching Ni in $\text{FeCl}_3 / \text{HCl}$ solution while it is floating and then transferring the MLG film onto a perforated substrate, see Figure 3.9a. Such clamped freestanding configuration is used for mechanical behavior testing, which will be discussed in Chapter 5 and Chapter 6. Confocal Raman spectroscopy (532 nm) mapping of a $20 \times 20 \mu\text{m}^2$ area is used to characterize the coverage and quality of the MLG on Ni. As depicted in Figure 3.9b, as-grown Ni-MLG film exhibits G peak at 1579 cm^{-1} . The blue shift of a narrow 2D peak (Full Width at Half Maximum (FWHM) $\approx 55 \text{ cm}^{-1}$ at 2701 cm^{-1}) suggests a strained state in MLG on Ni and orientation misalignment between the graphene layers.^{22, 23} After we transfer graphene layers onto a perforated substrate, the amplitude of the D peak (1355 cm^{-1}) slightly increases, indicating some defects introduced during the transfer process.²⁴ Raman intensity ratios I_{2D}/I_G and I_D/I_G are used to indicate the number of layer and the crystallite size or defects in graphene. As shown in Figure 3.9c, I_{2D}/I_G of Ni-MLG ranges from 0.91 – 1.02, confirming the multilayer nature in MLG. $I_D/I_G \sim 0.36$ (for $775 \text{ }^\circ\text{C}$ condition) implies relatively good quality of the MLG layers.



(a) Figure 3.9. (a) As-grown MLG can be readily transferred from Ni surface to a perforated substrate by etching Ni. (b) Raman spectra of as-grown MLG on Ni and transferred MLG showing the nature of multilayer and negligible transfer-induced defect. (c) Variation of Raman intensity ratios I_{2D}/I_G and I_D/I_G with different growth temperature. Intensity ratios are obtained from spatial maps of a $20 \times 20 \mu\text{m}^2$ area.

3.3. Graphene synthesis on coarse-grain thin metal films

3.3.1. Ultrathin Pd leaves with large grain structures

Although we avoid dewetting of thin Ni films in CVD process and achieve multilayer graphene synthesis, quality and crystalline size of the MLG layer in Ni-MLG are still far away from those in Cu-Gr systems. According to the strategy in Figure 3.7, we hereby increase the synthesis temperature for highly uniform carbon distribution and thus high graphene quality. Pd catalyst is used because of its higher melting temperature and high binding energy to graphene. Nevertheless, thin Pd films fabricated by the conventional deposition methods, like sputtering, will encounter solid-state dewetting at high temperatures. Figure 3.10 illustrates the sputtered Pd film having thickness of 150 nm breaks up after loaded in a 1100 °C furnace for 10 s and completely dewets after 30 s. This temperature is about 70 % of the melting point of bulk Pd.

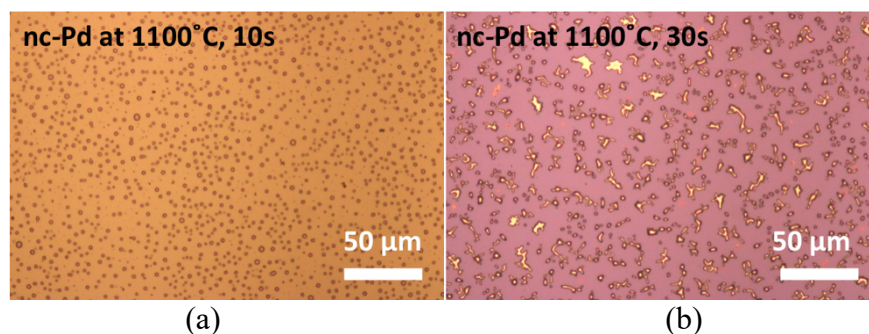


Figure 3.10. Optical images of a sputtered Pd film (sputtered on SiO₂/Si, thickness: 150 nm) heated in a 1100 °C furnace for (a) 10 s and (b) 30 s.

In this study, we use a commercially available ultrathin film material which has been extensively used for “gilding” furniture and sculptures, but possesses promising chemomechanical properties for CVD synthesis. Gilding is ubiquitously seen in artifacts having various sizes and materials.²⁵⁻²⁷ It is an ancient coating technique using ultrathin metal films, called metal leaves, beaten from pure bulks to cover over the base stones and wood, for example, Tutankhamun’s middle coffin as shown in Figure 3.11a. This decoration technique not only enriches the artwork with tiny amounts of precious metals, but also protects the precious artifacts owing to outstanding corrosion and wear resistance of these metal films. Importantly, gilding materials can be easily scalable. Figure 3.11b illustrates the gold leaf-gilded roof of Carbide & Carbon Building in Chicago. The ultrathinness of the metal leaves is crucial for the smooth conformation onto rough surfaces. To achieve the required thinness, the leaves are worked by repeated beating of thick pure metal foils from millimeter down to 100-200 nm. During beating, the metal layers are sandwiched between low surface energy sheets to allow well-lubricated flow of the metal and facilitate the isolation and manipulation of individual feestanding sub 200 nm thin leaves. The pure Pd leaves having dimensions of 150 × 150 mm² and 150 nm thickness are commercially available, see Figure 3.11c. SEM imaging shows the as-bought Pd leaves grain structure. As shown in Figure 3.11d, the

average grain size is about $20\ \mu\text{m}$ and extends through the film thickness. This large grain structure in ultrathin metal films is caused during the metalworking process shown in Figure 3.11e - 3.11h. Compared to grain growth from nanometer scale in deposited thin films, repeated beating allows the Pd crystal structure to downsize its thickness to nanometer scale while expand in plane in $10\text{-}100\ \mu\text{m}$ scale.

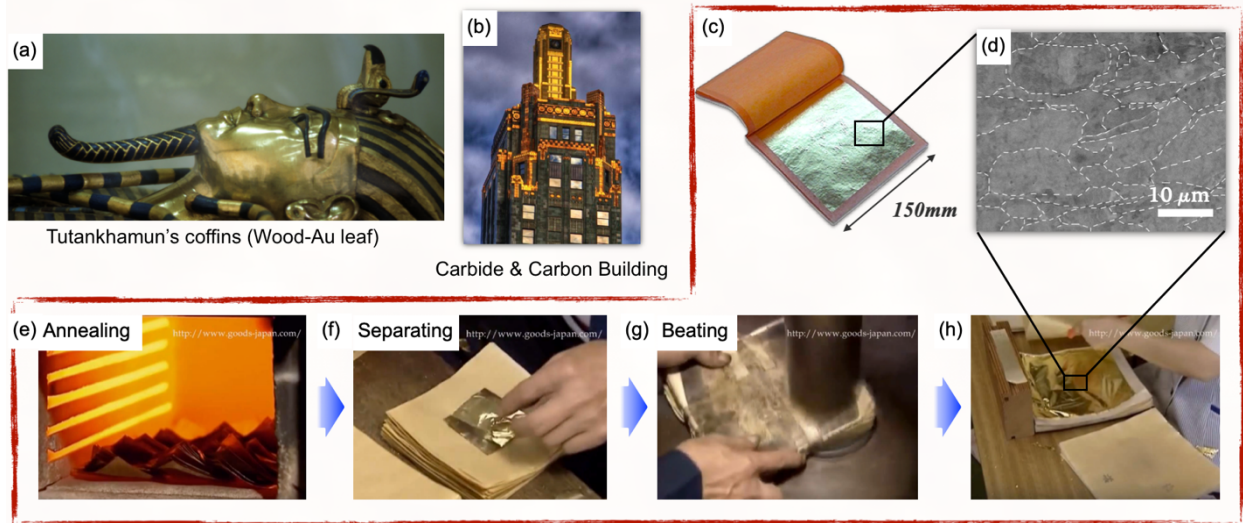


Figure 3.11. Ultrathin metal films having large crystalline structure from ancient gilding technique. (a) Photograph of the gold leaf-gilded wooden coffin of Tutankhamun. Copyright: Griffith Institute, University of Oxford. (b) Photograph of Carbide&Carbon Building in Chicago. Copyright 2010, Thaddeus Roan. (c) Photograph of a book of Pd leaves. (d) SEM image of the as-bought Pd leaf showing large ($> 20\ \mu\text{m}$) grain size. (e-h) Manufacturing process of ultrathin metal leaves for gilding.²⁸

Pd leaves offer substantial resistance to the solid-state dewetting compared to Pd films deposited by sputtering. Instead of obvious dewetting observed in Figure 3.10, Figure 3.12a and 3.12b show relatively complete surface of a Pd leaf supported on SiO_2/Si substrate after heating in a $1100\ \text{°C}$ furnace for 10 and 30 s. A few small holes can be optically seen under the microscope after 30 s.

After 45 s, 90 % of the Pd area is still intact. Figure 3.12c shows the fraction of the stable Pd area (defined as retained Pd area A_{Pd} over the total area A_{tot}) of Pd leaf and sputtered Pd film when heated at 1100 °C as a function of dwelling time t_g . Owing to large grain structure in 150 nm thickness, the Pd leaves have very low triple junction density and become more resistant to dewetting. This interesting property allows the synthesis of high quality graphene at high temperature.

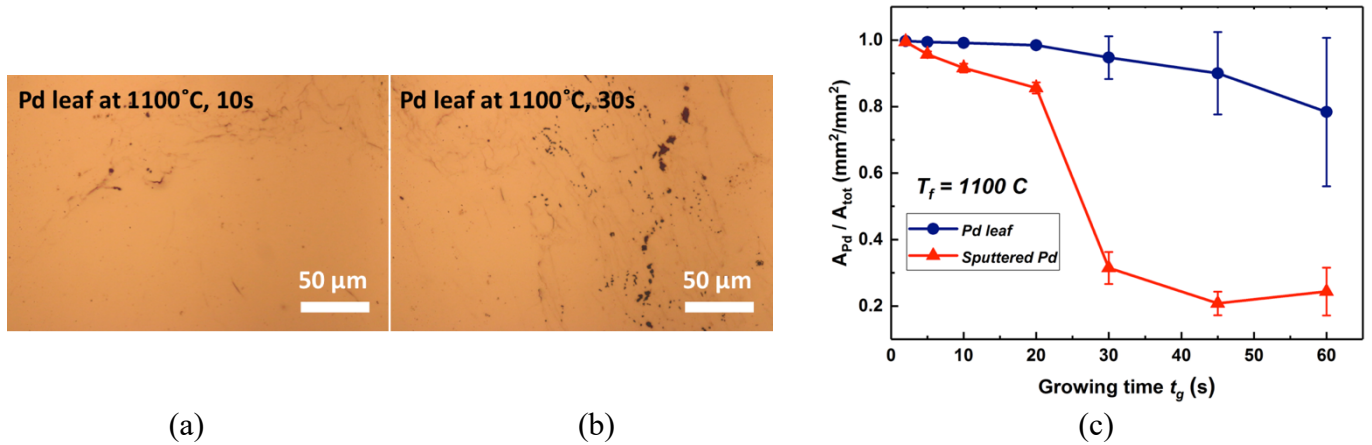


Figure 3.12. Optical images of a Pd leaf (laminated on SiO₂/Si, thickness: ~150 nm) heated in a 1100 °C furnace for (a) 10 s and (b) 30 s. (c) Comparison of retained Pd area on SiO₂/Si substrate after annealing at 1100 °C between sputtered Pd film and Pd leaf.

3.3.2. High quality graphene monolayer synthesis on Pd leaves

The Pd leaves are purchased from Wehrung & Billmeier Gold Leaf. As-received Pd leaf is laminated on a SiO₂/Si substrate using the capillary forces of a deionized water film, causing it to conformally stick to the substrate. The supported Pd leaf is then dried in ambient environment for 12 hours, before is cleaned in HNO₃ solution for 2 min and rinsed in DI water, Acetone, and IPA. It is then annealed in He (400 sccm) at 1.66 Torr at 500 °C for 5 hours to relax residue stress and reduce dislocations from processing.

Before presenting the synthesis results on Pd leaves, it is valuable to validate the analyses and modeling in section 3.1.2 and quantify the synthesis strategy proposed in Figure 3.7. Here, we heat the Pd leaf/SiO₂/Si catalyst at 1100 °C while flowing 10 sccm CH₄ and 400 sccm He in low pressure. Carbon concentration in Pd for dwelling time $t_g = 5, 10, 20, 30, 45$ and 60 s are compared by secondary ion mass spectroscopy (SIMS, PEI Trift-III TOF). Figure 3.13 displays the SIMS depth profiles. The measurements show that $t_g > 30$ s gives almost uniform carbon distribution throughout Pd leaf thickness.

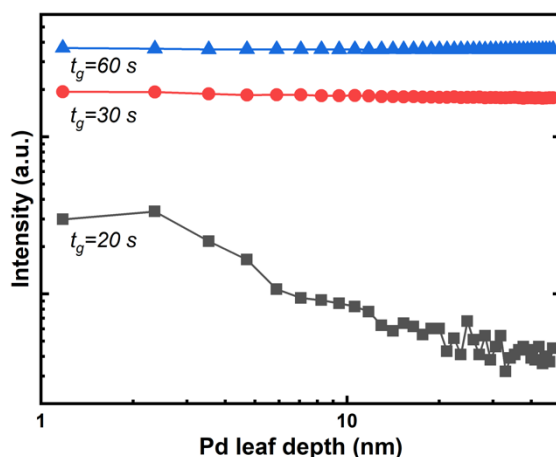


Figure 3.13. SIMS depth profiles show that the carbon concentration in Pd leaf becomes uniform as growth time increases.

Similar to synthesis with deposited Ni films, we heat the Pd leaves at 1100 °C while flowing the gases listed in Table 3.2. We have validated the proposed carbon diffusion and precipitation scenarios in the previous section by direct comparison to synthesis experiments:

Table 3.2. Recipes for CVD synthesis on Pd leaves (thickness ~ 150 nm) at 1100 °C

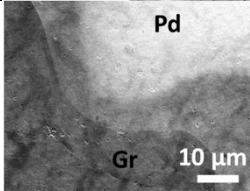
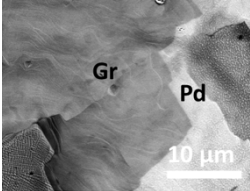
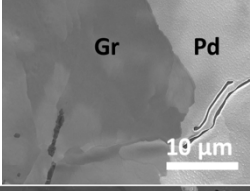
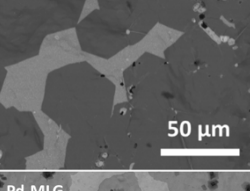
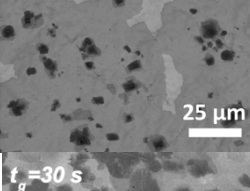
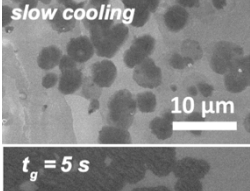
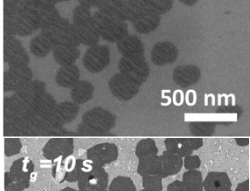
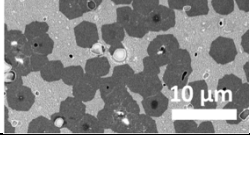
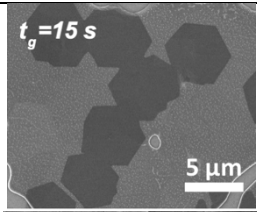
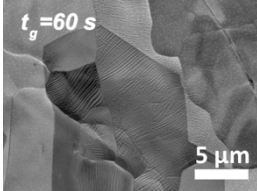
Label	Heating		Cooling		Growth time (s)	Cooling rate	SEM image
	Carbon precursor (sccm)	Other gases (sccm)	Carbon precursor (sccm)	Other gases (sccm)			
I	CH ₄ 10	He 400	-	He 400	30	Fast cooling	
II	CH ₄ 10	He 400	CH ₄ 10	He 400	30	Fast cooling	
III	CH ₄ 10	He 400	CH ₄ 50	He 400	30	Fast cooling	
IV	CH ₄ 50	He 400	CH ₄ 50	He 400	30	Fast cooling	
V	CH ₄ 50	He 400	CH ₄ 50	He 200	30	Fast cooling	
VI	CH ₄ 10	He 400	CH ₄ 50	He 400	30	Slow cooling	
VII	CH ₄ 10	He 400	CH ₄ 50	He 400	5	Fast cooling	
VIII	CH ₄ 10	He 400	CH ₄ 50	He 400	10	Fast cooling	

Table 3.2 (cont.).

IX	CH ₄ 10	He 400	CH ₄ 50	He 400	15	Fast cooling	
X	CH ₄ 10	He 400	CH ₄ 50	He 400	60	Fast cooling	

- For scenario I, hydrocarbon concentration on Pd surface (c_s) decreases during cooling and graphene nucleates with a diffusion flux J'_d . SEM image in Table 3.2 case I confirm that a large number of discrete graphite with fuzzy edges and dark regions of allomerated carbon along Pd grain boundaries are obtained.
- For scenario II, c_s is constant during heating and cooling. There is no net diffusion flux but a precipitation flux $J_{prec.}$ after incubation time. Synthesis result in case II confirms the formation of larger graphene coverage area, with sparse multilayer islands and more regular crystalline edges than in case I.
- For scenario III, c_s boosts up during cooling, triggers the carbon precipitation and graphene nucleation at higher temperature. SEM image in case III displays large and uniform monolayer graphene with hexagonal edges.
- It is expected that nucleation at high temperatures is the key to achieve high quality graphene, while there should be a “optimal range” of carbon segregation flux to Pd surface determining the number of graphene layers. In case IV, we increase c_s during cooling to achieve earlier precipitation. Large and hexagonal-like graphene domains can be produced

and eventually merge into a monolayer. Whereas, in case V, $J_{prec.}$ becomes out of range and leads to the nucleation of multilayer graphene domains underneath the monolayer.

- As analyzed in Figure 3.4, slow cooling leads to longer carbon incubation time and lower graphene nucleation temperature on Pd. SEM image in case VI with slower cooling rate illustrate small flakes with irregular and fuzzy edges.
- To validate the proposed kinetic model (e.g. Equation 3.5 and Figure 3.3) and synthesis strategy in Figure 3.7, we fix the hydrocarbon concentration c_s but vary the growth time t_g in case VII to X. Observations from SEM images suggest the expansion and evolution of graphene nuclei into large hexagonal-like domains. This can be explained by the sufficient segregation of dissolved carbon in Pd with longer t_g .

As-grown graphene layer can be readily transferred from a Pd leaf to a clean SiO₂/Si substrate via the electrochemical gas “bubbling” method.²⁹ Figure 3.14a shows a typical transferred result. We compare the Raman spectra of graphene grown on Pd leaf and transferred to SiO₂/Si. As shown in Figure 3.14b, graphene on Pd shows a weak Raman signal due to the known strong interaction between graphene and Pd.³⁰ $I_{2D}/I_G \sim 3$ from the transferred sample confirms the monolayer structure of graphene.

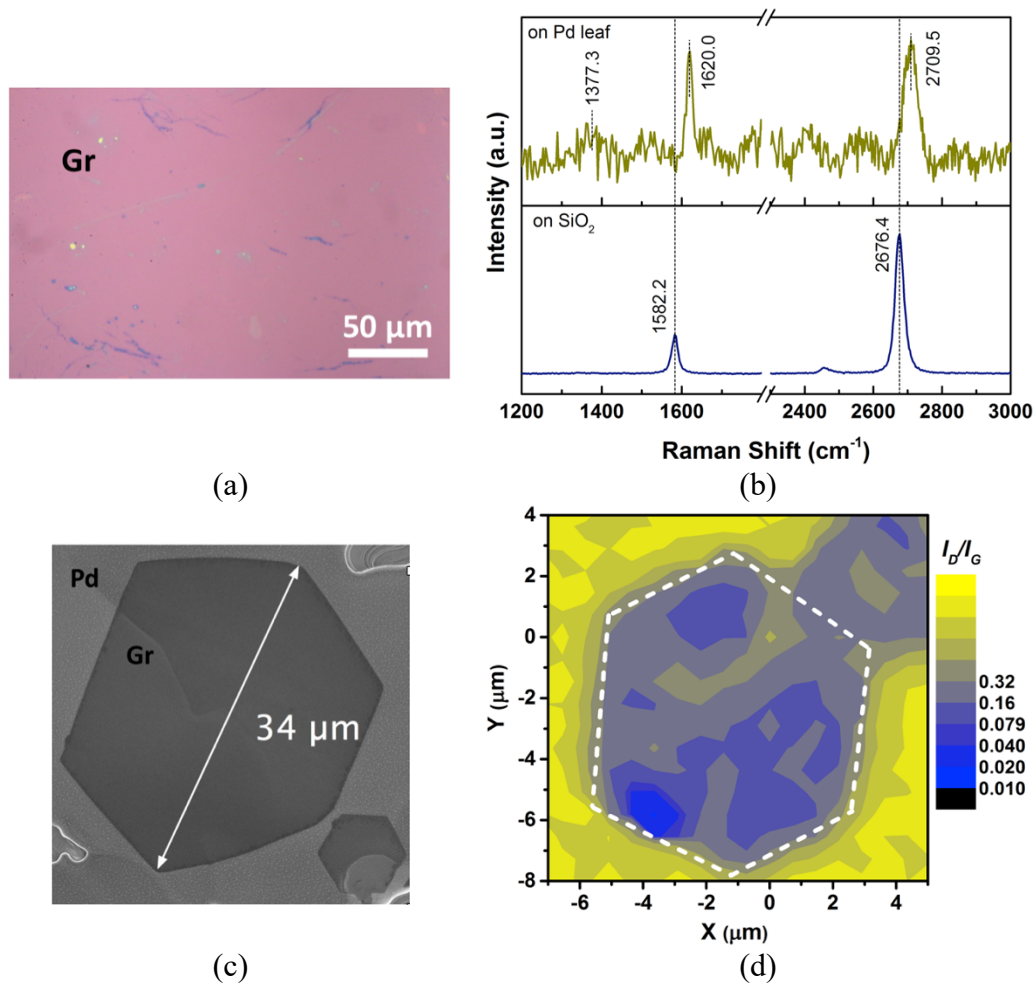


Figure 3.14. Raman analysis of as-grown Gr. (a) Optical image of transferred Gr on SiO₂/Si using bubbling method reported in ref²⁹. (b) Raman spectra of as-grown graphene on Pd leaf and transferred Gr. (c) SEM image of PdGr with growth condition V. (d) Raman spectroscopy map showing I_D/I_G of a single Gr crystal transferred on SiO₂/Si

Quality of this monolayer graphene is evaluated by I_D/I_G from Raman mapping. Firstly, for quality within a single hexagonal-like domain, only edge region has $I_D/I_G > 0.1$, implying the defect scarce graphene domain, see Figure 3.14c and 3.14d. Second, for the large merged area, a $23 \mu\text{m} \times 23 \mu\text{m}$ region Raman mapping and the statistical intensity ratios are used to compare the quality for different growth conditions. We observe a significant increase of quality represented

by the exponential decay in average I_D/I_G from case I to IV, shown in Figure 3.15a. This confirms the SEM observations in Table 3.2 that increasing hydrocarbon concentration c_s during cooling gives larger regular graphene domains. On the other hand, case V with precipitation flux out of optimal range leads to large variation in graphene crystal size as well as I_D/I_G . The average I_{2D}/I_G for II to IV is ≈ 3 , indicating monolayer graphene, whereas I_{2D}/I_G for I and V shows distribution below 2 suggesting the multilayer graphene sites, which agrees well with the synthesis results and kinetic model.

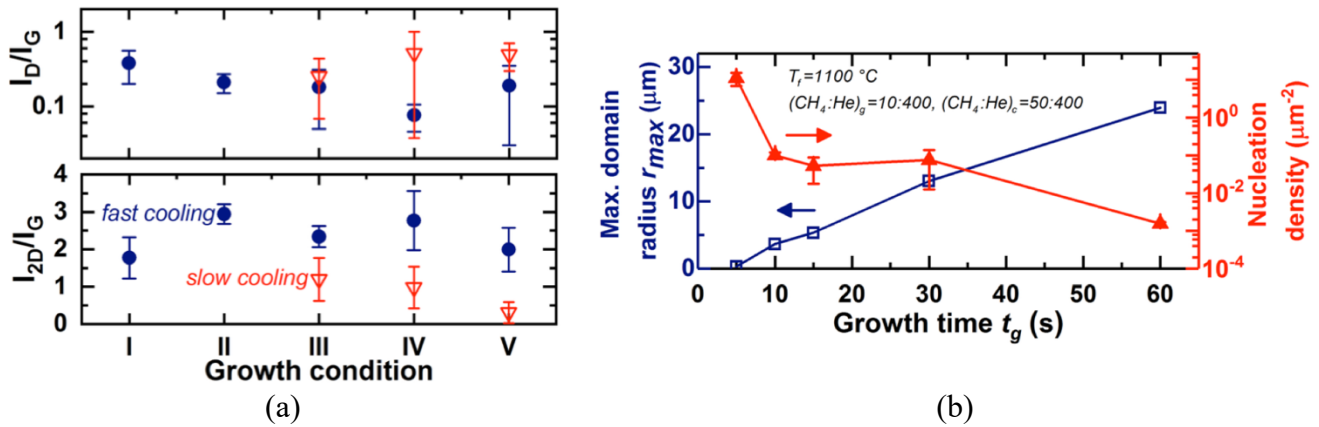


Figure 3.15. (a) Raman intensity ratios of I_D/I_G and I_{2D}/I_G for different growth conditions. (b)

Dependence of the maximum Gr domain radius ($\sqrt{A_{Gr}/\pi}$) and nucleation density on growth time.

The quality of graphene can also be evaluated based on the size of graphene domains, which is related to the nucleation density. We use growth case III to illustrate the trends of the maximum domain size (defined as $\sqrt{A_{Gr}/\pi}$, A_{Gr} is domain area) and graphene nucleation density with growth time. Figure 3.15b shows the size of the graphene domains on Pd leaf linearly increases with t_g and the growth rate for case III is $\approx 25 \mu\text{m min}^{-1}$, which is among the highest in the literature and twice the growth rate (≈ 10 - $15 \mu\text{m min}^{-1}$) of graphene on copper foil.^{31, 32} This can

be explained by considering the homogeneous dispersion of carbon throughout the Pd leaf with sufficient diffusion time as discussed in Figure 3.7. This also effectively reduces the nucleation density displayed in Figure 3.15b.

3.4. Conclusions

In summary, rapid low pressure CVD synthesis (<1 min) of high-quality and uniform graphene monolayer is achieved, for the first time, on the ultrathin Pd leaves providing a freestanding and cost-effective graphene-metal thin film composites. Pd leaves exhibit several qualities that make them suitable for graphene nucleation and growth at elevated temperatures despite their nanoscale thinness. We proposed a kinetic model to consider the carbon segregation and precipitation driven by gradient dynamic temperature and precursor concentration variations. The understanding and experiments developed herein pave the route to the rational design of ultrathin graphene-metal composites. As-grown graphene layers is shown to be highly crystallized, of low defect density and predominantly monolayer in thickness. This offers a starting point to probe the mechanical behaviors of as-grown graphene-metal composites.

3.5. References:

1. Li, X.; Cai, W.; An, J.; Kim, S.; Nah, J.; Yang, D.; Piner, R.; Velamakanni, A.; Jung, I.; Tutuc, E.; Banerjee, S. K.; Colombo, L.; Ruoff, R. S. *Science* **2009**, 324, (5932), 1312-1314.
2. Bae, S.; Kim, H.; Lee, Y.; Xu, X.; Park, J.-S.; Zheng, Y.; Balakrishnan, J.; Lei, T.; Ri Kim, H.; Song, Y. I.; Kim, Y.-J.; Kim, K. S.; Özyilmaz, B.; Ahn, J.-H.; Hong, B. H.; Iijima, S. *Nature Nanotechnology* **2010**, 5, 574.
3. An, X.; Liu, F.; Jung, Y. J.; Kar, S. *The Journal of Physical Chemistry C* **2012**, 116, (31), 16412-16420.
4. Gao, L.; Ren, W.; Xu, H.; Jin, L.; Wang, Z.; Ma, T.; Ma, L.-P.; Zhang, Z.; Fu, Q.; Peng, L.-M.; Bao, X.; Cheng, H.-M. *Nature Communications* **2012**, 3, 699.
5. Ma, D.; Liu, M.; Gao, T.; Li, C.; Sun, J.; Nie, Y.; Ji, Q.; Zhang, Y.; Song, X.; Zhang, Y.; Liu, Z. *Small* **2014**, 10, (19), 4003-4011.
6. Suk, J. W.; Kitt, A.; Magnuson, C. W.; Hao, Y.; Ahmed, S.; An, J.; Swan, A. K.; Goldberg, B. B.; Ruoff, R. S. *ACS Nano* **2011**, 5, (9), 6916-6924.
7. Giovannetti, G.; Khomyakov, P. A.; Brocks, G.; Karpan, V. M.; van den Brink, J.; Kelly, P. J. *Phys Rev Lett* **2008**, 101, (2), 026803.
8. Xu, Z.; Buehler, M. J. *Journal of Physics: Condensed Matter* **2010**, 22, (48), 485301.
9. Yazyev, O. V.; Pasquarello, A. *Physical Review Letters* **2008**, 100, (15), 156102.
10. Baraton, L.; He, Z. B.; Lee, C. S.; Cojocaru, C. S.; Châtelet, M.; Maurice, J. L.; Lee, Y. H.; Pribat, D. *EPL (Europhysics Letters)* **2011**, 96, (4), 46003.
11. R.W. Balluffi; S.M. Allen; Carter, W. C., *Kinetics of Materials*. Wiley & Sons: NJ, 2005.
12. Yokoyama, H.; Numakura, H.; Koiwa, M. *Acta Materialia* **1998**, 46, (8), 2823-2830.
13. *COMSOL Heat Transfer Module User's Guide*, 5.2a, June 17, **2016**; 2016.
14. *COMSOL Chemical Reaction Engineering Module User's Guide*, 5.2a, June 17, **2016**; 2016.
15. Kim, H.; Mattevi, C.; Calvo, M. R.; Oberg, J. C.; Artiglia, L.; Agnoli, S.; Hirjibehedin, C. F.; Chhowalla, M.; Saiz, E. *ACS Nano* **2012**, 6, (4), 3614-3623.
16. Weatherup, R. S.; Dlubak, B.; Hofmann, S. *ACS Nano* **2012**, 6, (11), 9996-10003.
17. Vlassioug, I. V.; Stehle, Y.; Pudasaini, P. R.; Unocic, R. R.; Rack, P. D.; Baddorf, A. P.; Ivanov, I. N.; Lavrik, N. V.; List, F.; Gupta, N.; Bets, K. V.; Yakobson, B. I.; Smirnov, S. N. *Nature Materials* **2018**, 17, (4), 318-322.
18. Thompson, C. V. *Annual Review of Materials Research* **2012**, 42, (1), 399-434.
19. Gadkari, P. R.; Warren, A. P.; Todi, R. M.; Petrova, R. V.; Coffey, K. R. *Journal of Vacuum Science & Technology A* **2005**, 23, (4), 1152-1161.
20. Thompson, C. V. *Annual Review of Materials Science* **1990**, 20, (1), 245-268.
21. Lee, C. H.; Kim, D. R.; Zheng, X. *Nano Letters* **2011**, 11, (8), 3435-3439.
22. Mohiuddin, T. M. G.; Lombardo, A.; Nair, R. R.; Bonetti, A.; Savini, G.; Jalil, R.; Bonini, N.; Basko, D. M.; Galiotis, C.; Marzari, N.; Novoselov, K. S.; Geim, A. K.; Ferrari, A. C. *Physical Review B* **2009**, 79, (20), 205433.
23. Robinson, J. A.; Wetherington, M.; Tedesco, J. L.; Campbell, P. M.; Weng, X.; Stitt, J.; Fanton, M. A.; Frantz, E.; Snyder, D.; VanMil, B. L.; Jernigan, G. G.; Myers-Ward, R. L.; Eddy, C. R.; Gaskill, D. K. *Nano Letters* **2009**, 9, (8), 2873-2876.
24. Gupta, A.; Chen, G.; Joshi, P.; Tadigadapa, S.; Eklund. *Nano Letters* **2006**, 6, (12), 2667-2673.
25. Oddy, W. A. *Endeavour* **1991**, 15, (1), 29-33.

26. Bray, W., 16 - Techniques of gilding and surface-enrichment in pre-Hispanic American metallurgy. In *Metal Plating and Patination*, Butterworth-Heinemann: 1993; pp 182-192.
27. Darque-Ceretti, E.; Felder, E.; Aucouturier, M. *Matéria (Rio de Janeiro)* **2011**, 16, 540-559.
28. <https://www.goodsjapan.com/>.
29. Gao, L.; Ren, W.; Xu, H.; Jin, L.; Wang, Z.; Ma, T.; Ma, L. P.; Zhang, Z.; Fu, Q.; Peng, L. M.; Bao, X.; Cheng, H. M. *Nat Commun* **2012**, 3, 699.
30. Usachov, D. Y.; Davydov, V. Y.; Levitskii, V. S.; Shevelev, V. O.; Marchenko, D.; Senkovskiy, B. V.; Vilkov, O. Y.; Rybkin, A. G.; Yashina, L. V.; Chulkov, E. V.; Sklyadneva, I. Y.; Heid, R.; Bohnen, K.-P.; Laubschat, C.; Vyalikh, D. V. *ACS Nano* **2017**, 11, (6), 6336-6345.
31. Wu, T.; Zhang, X.; Yuan, Q.; Xue, J.; Lu, G.; Liu, Z.; Wang, H.; Wang, H.; Ding, F.; Yu, Q.; Xie, X.; Jiang, M. *Nature Materials* **2015**, 15, 43.
32. Wu, T.; Ding, G.; Shen, H.; Wang, H.; Sun, L.; Jiang, D.; Xie, X.; Jiang, M. *Advanced Functional Materials* **2013**, 23, (2), 198-203.

CHAPTER 4: NANOMECHANICS AT THE GRAPHENE-METAL INTERFACE

Abstract

The interfaces between graphene and the metal substrates are of critical importance not only in applications of graphene in electronic devices, but also in the mechanical behavior of graphene-metal composites. It is well-established that a small band gap opens in the electronic structure of graphene synthesized on some metals such as Pd. However, the intricate mechanics of the graphene-metal interface are usually overlooked. In this chapter, we focus on two fundamental aspects of graphene-metal interactions when graphene nucleates and grows on the metal substrate. The first is the conformability of CVD grown graphene on metal grains. The multi-frequency atomic force microscopy is used to spatially map the elastic properties and topography of graphene on metal grain boundaries. Using this technique, we reveal that effective reinforcement is achieved when graphene conforms and bridges the grain texture due to synthesis, whereas transferring graphene onto the metal thin film leads to non-conformably attached graphene on the Ni. Our second focus is the lattice strain associated with the epitaxy of graphene grown on the metal substrate. Raman spectroscopy is used to isolate strain effect due to lattice and thermal expansion mismatch in graphene-metal system, and from doping effect caused by strong graphene-metal interaction. The native strain in as-grown graphene is strongly dependent on the different metal crystal orientations. We also found that the Raman peak shift is significantly different for graphene on smooth metal grains than from those grains which undergo surface reconstructions during synthesis. This indicates that surface reconstruction in the metal grains is a mechanism to release the strain energy in the graphene during synthesis.

4.1. Conformability of CVD-grown graphene on polycrystalline thin metal films

Graphene conforms to the surface topography of the polycrystalline catalyst substrate during CVD synthesis. It is common to have individual graphene grains larger than the underlying metal grains and spanning many grains, as shown in Figure 4.1. A conformal graphene-metal interface can efficiently leverage the superb mechanical and electrical properties of graphene in the graphene-metal interaction and results in prominent enhancement in thermal conductivity and mechanical strength.¹⁻⁴ In this study, the amplitude-modulated frequency-modulated atomic force microscopy (AMFM-AFM) is used to characterize the conformability of the graphene-metal interface. This novel technique allows the measurement of not only the topography but also the relative variation of the substrate's modulus with nanoscale spatial resolution. The measurements give relative changes in surface modulus by tracking the changes in the second resonant frequency of a multi-frequency driven cantilever.⁵ Here, we compare two kinds of graphene-metal surfaces: (i) as-grown Ni thin film (155 nm) multilayer graphene (referred to as Ni-MLG) via CVD processes and (ii) MLG layer transferred onto an annealed sputtered Ni (referred to as MLG-on-Ni). As discussed in the previous chapter, both Ni-MLG and annealed Ni thin films exhibit the average grain size of 589 nm after high temperature treatment and surface roughness of 40 nm.

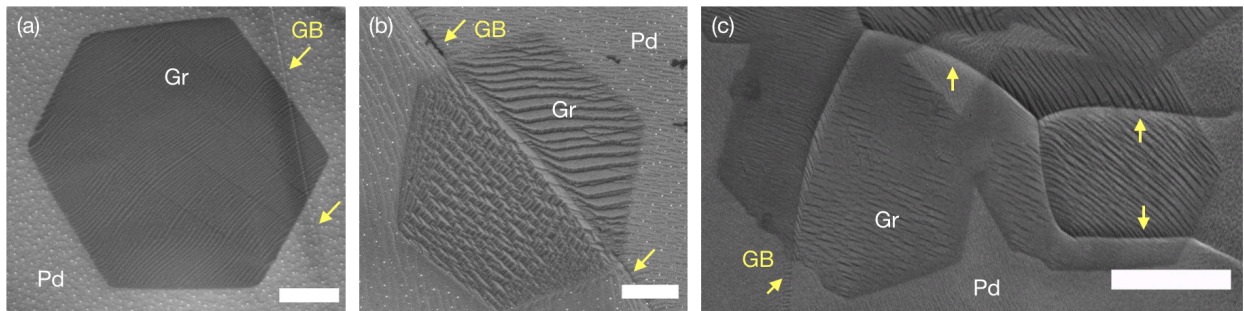


Figure 4.1. Example SEM images of the single graphene domain grown across Pd grain boundaries (GB, marked by arrows) via CVD. Scale bar: (a) 2 μm , (b) 1 μm , (c) 5 μm .

Figure 4.2 compares the AFM topography of the Ni-MLG and the MLG-on-Ni surfaces. For Ni-MLG, the grown graphene layers follow the surface structures of Ni after synthesis, as shown in Figure 4.2a and 4.2b. When graphene layers are transferred onto bare Ni surface, it is mostly suspended across the peaks of different Ni grains due to nanoscale surface roughness, see Figure 4.2c and 4.2d. We can compare graphene conformability more clearly in AFM line profiles in Figure 4.2e and 4.2f. Line profiles h1 and h3 for Ni-MLG surface “recreate” the surface microstructures of underlying Ni grains, except for the tiny sharp bumps related to the graphene wrinkles. On the contrast, line profiles h2 and h4 for MLG-on-Ni surface just exhibit general topography with much larger microstructure size than the actual Ni grain size measured in SEM.

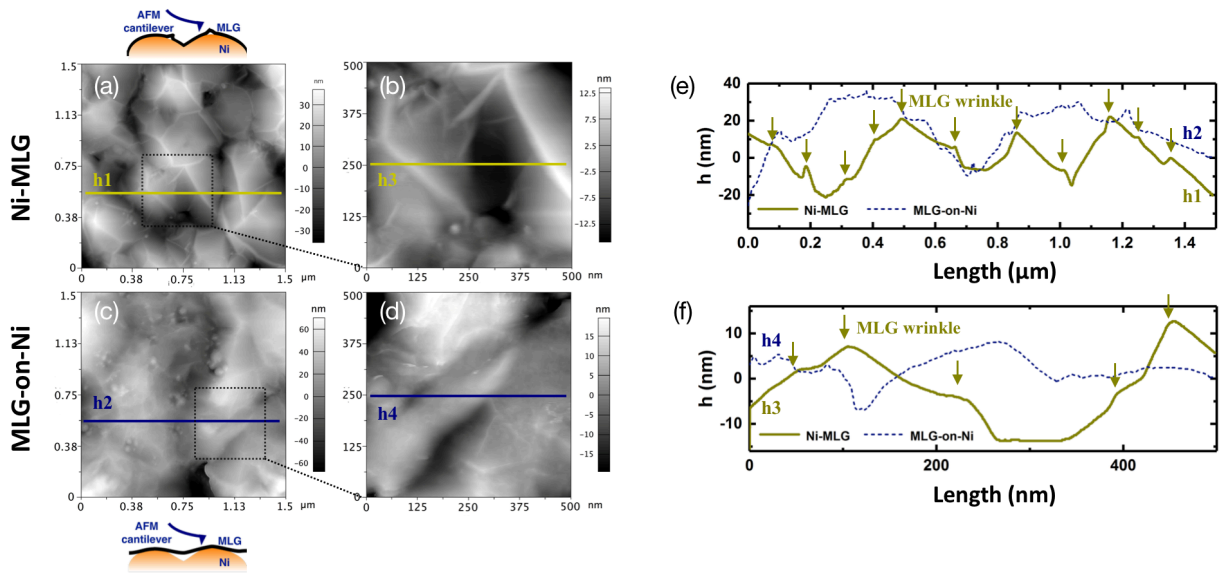


Figure 4.2. AFM topography of Ni-MLG and MLG-on-Ni composites. (a-b) Topography of Ni-MLG. (c-d) Topography of MLG-on-Ni. (e) Topographic line profiles along line h1 for Ni-MLG and h2 for MLG-on-Ni. (f) Topographic line profiles along line h3 (Ni-MLG) and line h4 (MLG-on-Ni). Red arrows point the graphene wrinkles.

Qualitative insights can be obtained by comparing the topography to the surface modulus for each graphene-Ni surface. The Ni grains, which possess varying moduli based on their crystalline orientations, are responsible for the background fluctuations in AFM 2nd mode resonance frequency which is related to the surface modulus in Figure 4.3a and 4.3b for Ni-MLG case. On the other hand, when graphene layer is transferred onto Ni, the graphene-Ni contact in MLG-on-Ni is not as conformal as that in Ni-MLG, see Figure 4.3c and 4.3d. A close look at line profiles f1 and f3 displayed in Figure 4.3e and 4.3f indicate that surface modulus change on Ni-MLG surface reflects the expected variations in the modulus of the Ni grains due to their crystallographic orientations. Notably, the negative spikes in the surface modulus line profiles can be correlated with the local graphene wrinkles, which are marked by the arrows in both Figure 4.2 and 4.3. The average surface modulus for MLG-on-Ni surface (line profiles f2 and f4) is significantly lower than that for Ni-MLG. This is indicative of a suspended graphene layer across the metal grains. It is reasonable to conclude that this non-conformal graphene-metal interface resulting from nanoscale surface roughness reduces the strengthening and toughening effects in graphene-metal composites in general. Detailed experimental results will be discussed in the following chapters.

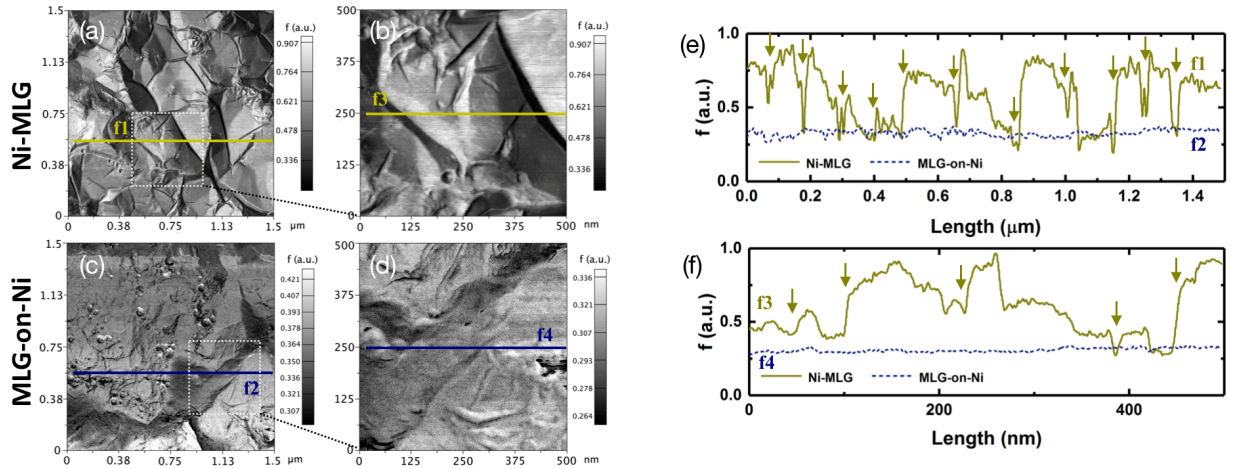


Figure 4.3. (a-b) Relative contact stiffness of Ni-MLG from 2nd mode resonance frequency. (c-d) Relative contact stiffness of MLG-on-Ni. (e) Surface modulus profiles along line f1 (Ni-MLG) and line f2 (MLG-on-Ni). (f) Surface modulus profiles along line f3 (Ni-MLG) and line f4 (MLG-on-Ni).

4.2. Interfacial strain of CVD grown graphene on thin Pd films

4.2.1. Raman spectroscopy characterization of graphene on Pd leaves

The properties of graphene depend sensitively on its epitaxy on the metal catalyst, and the atomic scale mechanics at this interface. From the thermodynamic perspective, these mechanics arise from the electronic interaction of the carbon atoms with the Pd atoms, and the stresses due to lattice mismatch and thermal stresses during growth. Moreover, due to the kinetics associated with growth of graphene at high temperature followed by cooling, the final configuration of the interface is complex and rich with phenomena such as peculiar surface reconstructions. The stress state of graphene on the metal substrate is tailored during CVD synthesis processes, and this interface tunes the final graphene-metal composites mechanical properties. Raman spectroscopy is a powerful and non-destructive tool for characterizing the local properties of

graphene.⁶ Doping and hydrostatic strain in graphene can lead to a shift of the Raman modes.⁷ Correlation analysis of the characteristic peaks for graphene in Raman spectroscopy has been recently used for accessing the local strain configuration of graphene on various substrates.⁸⁻¹⁰ Here, we systematically characterize the stress state of as-grown graphene on the metal substrate with respect to the relaxed graphene using Raman spectroscopy. We focus on monolayer graphene grown on Pd leaf (referred to PdGr). As discussed in Chapter 3, upon cooling of Pd substrate from synthesis temperature (e.g. 1100°C), graphene starts nucleating by carbon segregation and precipitation towards Pd surface. Due to the mismatch between the thermal expansion coefficients of graphene ($-8.0 \pm 0.7 \times 10^{-6} K^{-1}$)¹¹ and Pd ($11.8 \times 10^{-6} K^{-1}$), Pd substrate contracts while graphene expands during cooling process, as displayed in Figure 4.4. As a result, the kinetics of the process always lead to the relative increase in compression during cooling. Furthermore, the graphene-metal interface tends to relax such strain if it reaches excessive compression values by graphene folding, bending and even the graphene-metal interface reconstruction.^{12, 13} We also observed that for freestanding graphene prepared by etching the metal substrate or other electrochemical transferring method after synthesis, the installed strain will be released leaving an unstrained graphene layer. The main idea in this study, as shown in Figure 4.4, is to compare the Raman peak shift between the transferred unstrained graphene to that in as-grown PdGr to determine the local strain configuration at the graphene-Pd interface.

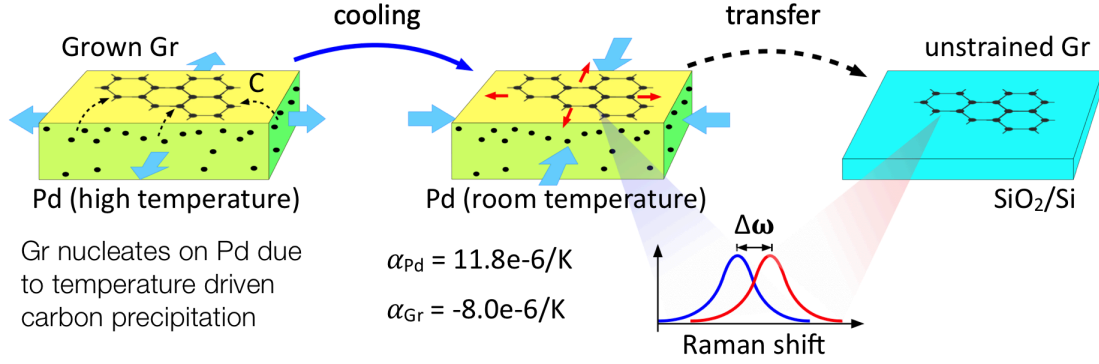


Figure 4.4. Schematics of strain developed during CVD-grown graphene on Pd substrate.

Figure 4.5a displays a typical optical microscope (OM) image of the grown PdGr leaf. We choose a hexagonal graphene pattern and transfer it onto a SiO₂(300nm)/Si substrate using a bubbling transfer method.¹⁴ Figure 4.5b shows the OM image of the transferred graphene hexagons (darker purple) and Figure 4.5c displays the Raman spectra (with a 100 X objective at 532 nm laser excitation, 30s) corresponding to the locations marked in 4.5b. As-grown graphene hexagon exhibits high 2D-G intensity ratio ($I_{2D}/I_G \sim 3.0$) and visually imperceptible D peak, expect for locations close to the edge (#d and #e). This suggests the high-quality graphene monolayer achieved via the proposed rapid CVD processes in the previous chapter. The comprehensive insights can be obtained from Raman mapping on this monolayer graphene hexagon. We use the I_G map to locate the outline of hexagonal graphene, see Figure 4.5c. And the I_D/I_G map shown in Figure 4.5d highlights the low defect density inside of graphene domain but strong intensity ratios on the hexagonal edge, which can be caused by the relative position of the laser spot with respect to the edge and amount of edge disorder.¹⁵ The I_{2D}/I_G map gives the uniform intensity ratios around 2.9 confirming the monolayer nature.¹⁶

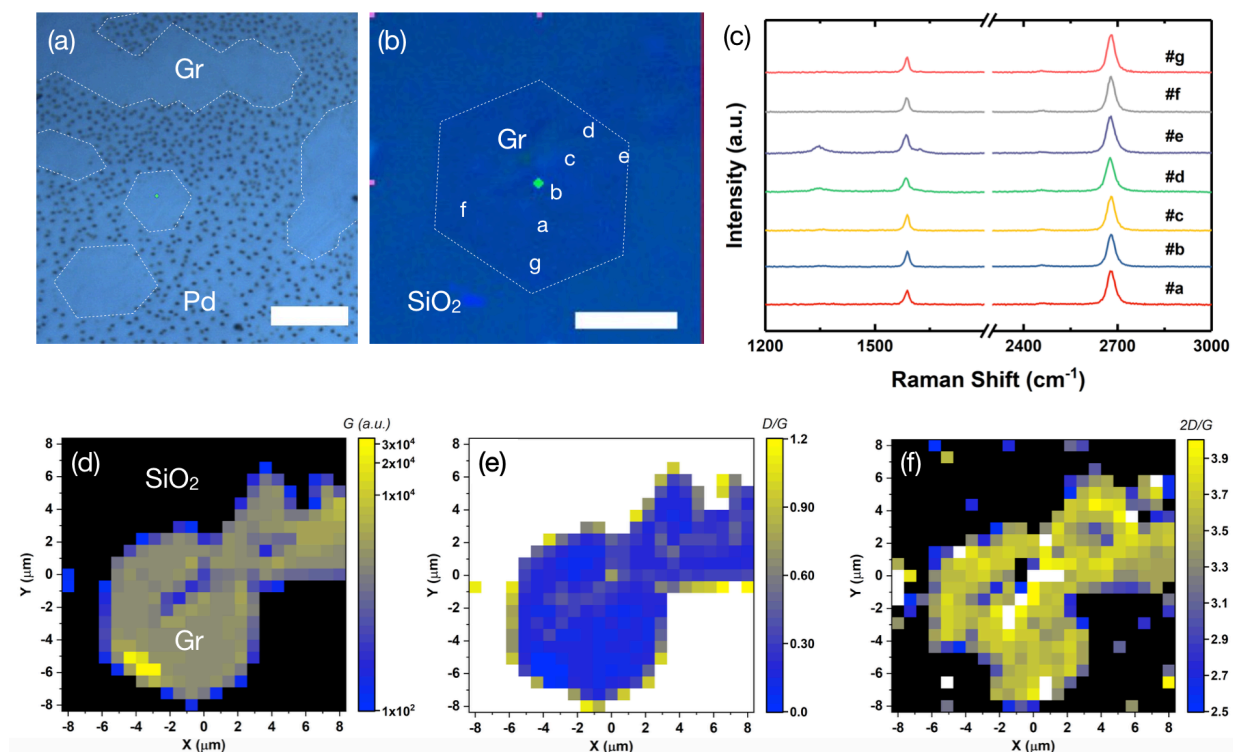


Figure 4.5. Raman spectroscopy of transferred Gr on SiO₂. (a) OM image of the single crystal graphene grown on Pd leaf. Scale bar: 10 μm. (b) OM image of a transferred single crystal Gr on the SiO₂/Si substrate. Scale bar: 5 μm. (c) Representative Raman spectra corresponding to the locations in (b). Laser: 532 nm. (d-f) Raman maps of G peak, intensity ratio I_D/I_G and I_{2D}/I_G indicating high-quality graphene monolayer.

Raman mapping can also be obtained from as-grown PdGr leaf. Figure 4.6 compares the graphene characteristic Raman frequencies (ω) and the corresponding full width at half maximum (Γ) of the transferred graphene on SiO₂ and those of as-grown graphene on Pd leaf. Notably, it is mentioned earlier in the previous chapter that Raman signal from monolayer graphene on Pd leaf is much weaker than that on SiO₂. This is due to the strong interaction of CVD grown graphene with metal catalysts like Pd. Hybridization of the π orbitals of graphene and the d electrons of metals modifies the Dirac cone, therefore suppresses Raman scattering.¹⁷

¹⁸ The average $\overline{\omega_G}$ and $\overline{\omega_{2D}}$ for the transferred graphene on SiO₂ lie at 1585.3 cm⁻¹ and 2680.3 cm⁻¹, respectively, which agree well with the reported pristine graphene with no strain and no doping.⁸ For the graphene on Pd case, $\overline{\omega_G} = 1614.4$ cm⁻¹ and $\overline{\omega_{2D}} = 2688.5$ cm⁻¹, showing obvious blue shifts and broadening in 2D peak.

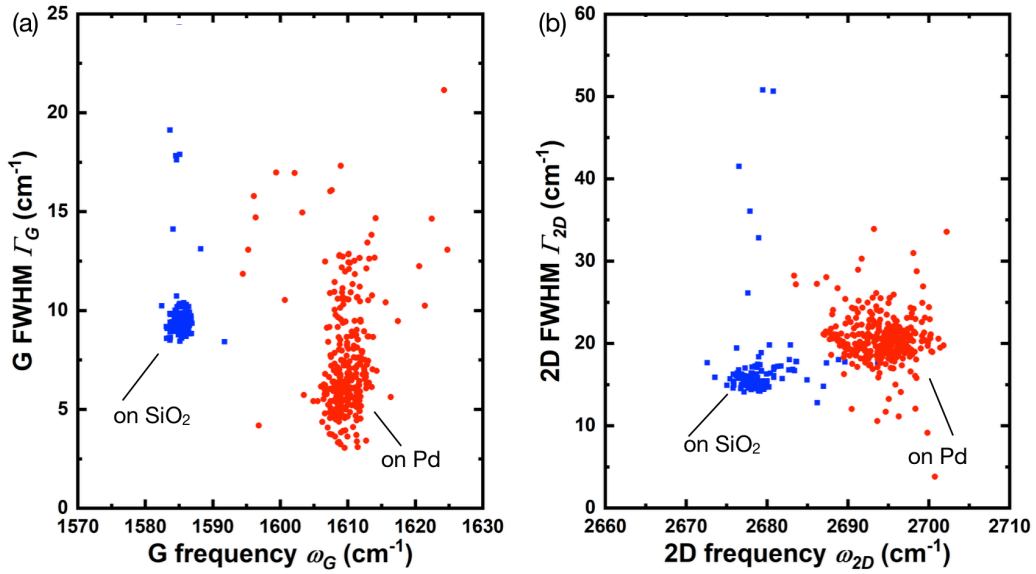


Figure 4.6. Comparison of the transferred graphene and as-grown graphene on Pd in Raman spectroscopy G peak (a) and 2D peak (b).

Compressive strain in graphene has been reported on other metals such as copper.^{12, 13, 19} What is interesting for PdGr system is, graphene layer is compressed when it sits on Pd lattice due to lattice mismatch. Based on density function theory (DFT) calculation, such initial biaxial compressive strain can be up to 3.3 % for the epitaxial PdGr configuration.²⁰ We expect the graphene-Pd interface has high strain which can contribute to mechanical behaviors in PdGr thin film composites.

4.2.2. Load transfer of as-grown PdGr leaf composites

Here, we first study the load transfer in between graphene and the Pd ultrathin leaves using the aforementioned Raman spectroscopy. After CVD synthesis, freestanding PdGr leaves can float on the surface of water due to the intercalation of water between the SiO₂ substrate and the bottom surface of the Pd. This allows us to transfer the Pd leaves with the grown graphene on the top to the surface of a poly(methylmethacrylate) (PMMA) bar, where it is also glued by a thin layer of PMMA. The PMMA bar with PdGr leaf is subjected to three-point bending, while Raman spectra (100 X, 532 nm, 30 s) are recorded in situ, as sketched in Figure 4.7. The size of PdGr leaf is much smaller than the PMMA bar, suggesting a uniform uniaxial strain in the section measured in Raman spectroscopy. The maximum tension strain applied to PdGr leaf is around 0.6 % before thin film delamination from PMMA substrate. We take Raman spectrum of the flat PdGr leaf on an unbent PMMA bar as the reference zero strain in graphene layer. Uniaxial tension graphene by Raman spectroscopy is widely used to test graphene's behavior under external mechanical loads.^{9, 21} In brief, as shown in Figure 4.7, the doubly degenerate optical mode splits in two components: one polarized along the uniaxial strain and the other orthogonal. This can split the G peak into two sub-peaks, G^+ and G^- . By tracking this Raman peak shifting, we can know the onset of graphene sliding on Pd substrate.

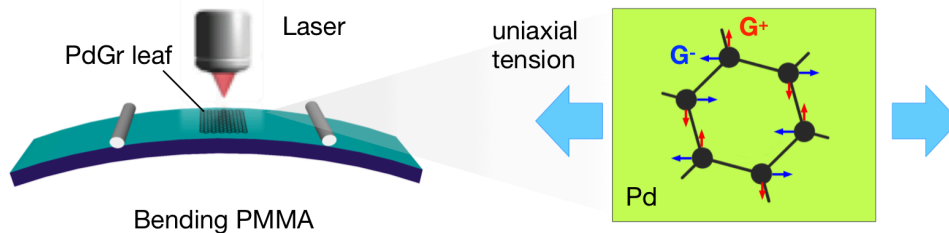


Figure 4.7. Schematics of uniaxial tension applied on PdGr thin film composite using three-point bending. Phonon eigenvectors G^- and G^+ are orthogonal to each other.

Figure 4.8a displays the experimental results in which clear redshift and splitting of the G peak are observed when PdGr leaf is stretched by the bending setup. This provides solid evidence that uniaxial tension has been transferred to graphene layer on top of Pd leaf. The G peak is split into two sub-peaks with the shift rates $\partial\omega_{G^+}/\partial\varepsilon \approx -14.0 \text{ cm}^{-1}/\%$ and $\partial\omega_{G^-}/\partial\varepsilon \approx -31.8 \text{ cm}^{-1}/\%$, while the 2d peak shifts with the rate of $\partial\omega_{2D}/\partial\varepsilon \approx -30.5 \text{ cm}^{-1}/\%$, as shown in Figure 4.8b and 4.8c. Importantly, the G peak shifts in as-grown PdGr in this study are similar to those observed in the exfoliated graphene monolayers. The corresponding Gruneisen parameter $\gamma(G) \approx 2.27$, also matches the upper values estimated in literature.²² Overall, the large linear shift of the G peak suggests the strong adhesion of graphene on Pd and the more efficient stress transfer than that in graphene on polymer and copper.

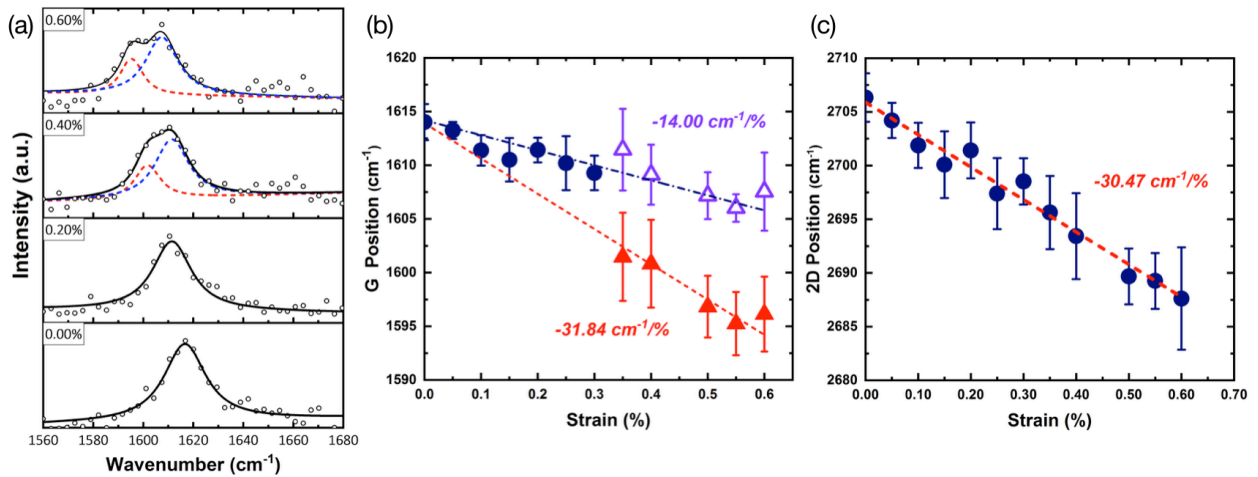


Figure 4.8. Stress transfer in as-grown PdGr thin film composite. (a) The evolution of Raman spectra of PdGr thin film when strained uniaxially under three-point bending. Redshift in the G peak and splitting into two sub-peaks indicate the uniaxial tension in graphene layer. (b) The G peak shift under tension for various level of strain in PdGr. (c) Corresponding 2D peak shift to

(b).

4.3. Orientation dependent interfacial stresses in graphene on Pd substrate

4.3.1. Orientation dependent surface reconstructions on PdGr leaves

Importantly, the uniaxial strain discussed in Figure 4.8 is the relative strain applied on a PdGr thin film composite with respect to its unbent state, in which graphene is biaxially strained due to CVD synthesis. As described in Figure 4.4, it is known that graphene is under intrinsic strain due to growth in this unbent reference state, and that the strain is dependent on the crystalline structure of the underlying metal.^{13, 23} Moreover, in addition to homogeneous strains due to lattice mismatch, the strains can lead to surface reconstruction in the graphene covered regions on Pd leaves. The morphologies of such terrace structures show strong correlation to Pd crystalline orientations. Figure 4.9a displays an example of a fully graphene grown region on Pd leaf with a secondary hexagonal graphene layer. We characterize the underlying Pd orientations using the electron backscattering diffraction (EBSD, 30 kV). Corresponding inverse pole figure (IPF) in Figure 4.9b verifies two Pd orientations in the region. The surface having an average miscut angle $\alpha = 3.6^\circ$ to Pd (010) is very smooth without visible surface steps or terrace. While on Pd (111) surface, small wavy steps can be observed, especially in the hexagonal bilayer area. This observation agrees with the reported studies in Cu-Gr system that low index surfaces (e.g. $\{111\}$ and $\{100\}$) remain smooth after graphene growth.²⁴ However, for high index surfaces, synthesizing a monolayer graphene can cause complex surface reconstructions. Figure 4.9c and 4.9d display a hexagonal graphene monolayer grown across two Pd grains. The surface with a small miscut angle ($\alpha = 4.2^\circ$) to Pd (110) has obvious and almost unidirectional steps, whereas a large miscut angle ($\alpha = 11.5^\circ$) surface shows a different crosshatched step pattern. More interestingly, the symmetry of a hexagonal graphene monolayer can be broken on the different Pd orientations. Figure 4.9e and 4.9f show a hexagonal graphene monolayer grown across a low

index and a high index Pd surfaces. Graphene remains hexagonal edges on Pd (110) ($\alpha = 17.7^\circ$) with obvious steps, however, it shows square edges on Pd (010) ($\alpha = 2.6^\circ$) with a much smoother surface topography. Figure 4.9 just lists three typical types of Pd surface reconstruction patterns caused by monolayer and bilayer graphene. Actually, surface microstructure change after CVD synthesis of graphene monolayer wide varies over different Pd orientations. Basically, three phenomenological conclusions can be obtained: (i) low index PdGr surfaces (e.g. Gr grown on $\{111\}$ and $\{100\}$ Pd surfaces) show shallow and wavy steps; (ii) high index PdGr surfaces show hierarchical sharp steps or terraces, with unidirectional or crosshatched main steps, as well as orthogonal secondary steps in the spacing between two main steps (Figure 4.9g); (iii) surface microstructures can be different in the stacked graphene regions, e.g. bilayer graphene, from those in the basal layer, see Figure 4.9a and 4.9h.

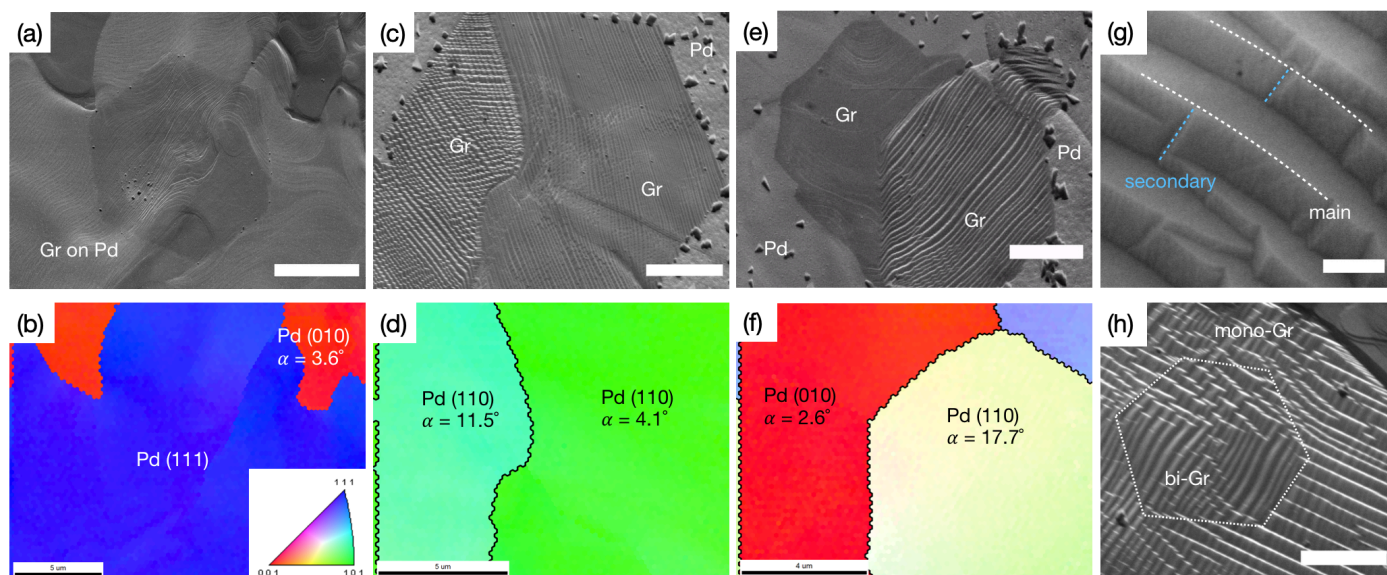


Figure 4.9. Correlation of Pd substrate orientation and PdGr surface morphology. (a) Graphene grown on Pd (111) and Pd (010) with a miscut $\alpha = 3.6^\circ$. Scale bar: 5 μm . (b) Corresponding IPF to (a). (c) Graphene grown on Pd {110} with miscuts of $\alpha = 11.5^\circ$ and $\alpha = 4.1^\circ$. Scale bar: 3 μm . (d) Corresponding IPF to (c). (e) Graphene grown on Pd (010) ($\alpha = 2.6^\circ$) and on Pd (110) ($\alpha = 17.7^\circ$). Scale bar: 3 μm . (f) Corresponding IPFs to (e). (g) Zoomed-in SEM image on the step region showing secondary steps orthogonal to and between two main steps. Scale bar: 200 nm. (h) SEM image showing a hexagonal bilayer graphene can change surface microstructure. Scale bar: 2 μm .

Here, we ask the origins of these abrupt surface reconstructions on PdGr surfaces and their relation to the graphene-metal interfacial stress. Typically, for the polycrystalline metal substrates, which are typically used for most of CVD synthesis, metal surface would facet to minimize its surface free energy at high temperatures. Extremely small surface steps / pyramids are formed during annealing with lateral size of <10 nm in the bare metal without graphene synthesis.²⁵ These surface steps are driven by atomic metal surface diffusion, and different from

what the patterns displayed in Figure 4.9. Figure 4.10 gives a close look at the height profiles of PdGr surface reconstructions using atomic force microscopy (AFM). In Figure 4.10a, a clear hexagonal edge between bare Pd region and the graphene monolayer region can be observed. Height profile across this edge (Figure 4.10b) shows two kinds of surface roughness. Bare Pd which has undergone high temperature treatment exhibits uniform and shallow surface microstructures with about 4.3 nm in height. While in graphene grown region, surface becomes very rough with hierarchical structures and larger lateral size. A zoomed in scanning in Figure 4.10c and 4.10d show directional uniform ridges with height of ~ 20.4 nm and period of ~ 223.0 nm. Notably, there is no graphene wrinkles or graphene-Pd delamination seen in AFM images. As-grown graphene layer should conformably follow the roughness in Pd. There is over 380 % rise in Pd surface roughness due to graphene monolayer synthesis. Such abrupt change in surface microstructures on the same sample requires a large energy input, and we think it could be from the elastic strain energy in graphene.

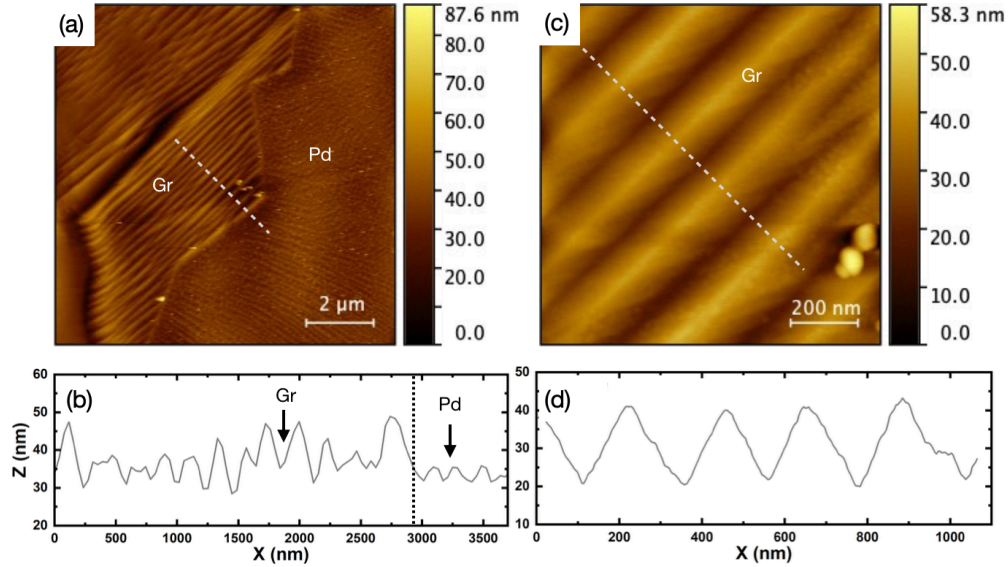


Figure 4.10. (a) AFM topographic image of as-grown graphene monolayer on Pd leaf. (b) AFM height profile of the dash line marked in (a). (c) The zoomed-in AFM topographic image of the graphene grown region in (a). (d) Height profile of the dash line in (c).

4.3.2. Strain at the graphene-Pd interface probed by Raman spectroscopy

To study the strain at CVD grown graphene-Pd interfaces, it is important to firstly ask the configuration of graphene when carbon atoms register on the Pd surface at the synthesis temperature. For example, Figure 4.11 displays the most stable symmetric configuration of graphene sitting on the Pd (111) surface according to the first-principles simulation.²⁶ Comparing the cell parameter – presented by the red dash line – of graphene before and after interacts with Pd atoms, it is found that graphene is initially in compression ($\sim 3.4\%$) with this stable configuration.²⁰ Notably, this simulation is at zero temperature, and in a real case at extremely high synthesis temperatures, Pd lattice spacing will expand. As a result, the newly-formed graphene layer on Pd may be stretched, and the epitaxial configuration shown in Figure 4.11 may not hold. In either case, the compression stress will apply on graphene due to thermal contraction

in Pd and thermal expansion in graphene during CVD cooling process, as described in Figure 4.4. Therefore, graphene on the Pd surface can be in either in tension or in compression. Non-zero temperature first principles simulation for the stable graphene configuration on the Pd surface is needed to validate.

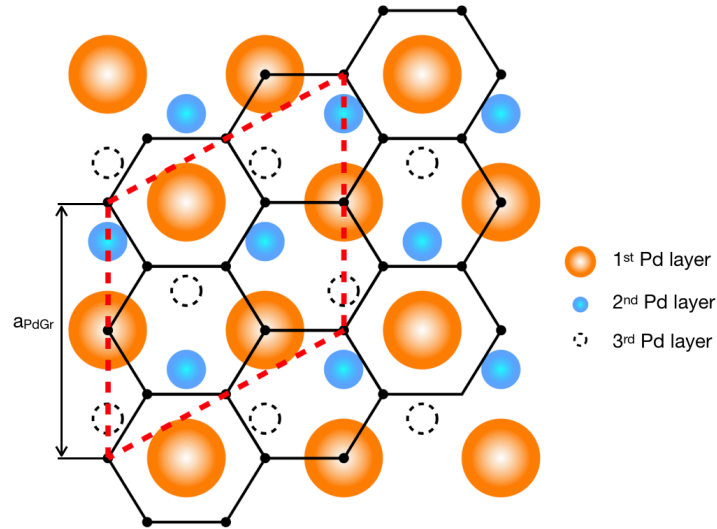


Figure 4.11. The most stable symmetric configuration of graphene on Pd (111) at zero temperature. The red dash line represents the cell parameter of the surface unit cells for graphene

$$\text{on Pd: } a_{PdGr} = 4.76 \text{ \AA}.^{20, 26} \text{ Notably, } a_{Gr-Gr} = 4.92 \text{ \AA}.$$

There are extensive studies on extracting the native strain in graphene using Raman spectroscopy.^{8, 9, 12, 13, 27} On a weak interacting catalyst, like Cu, there is negligible doping shift in graphene Raman spectrum.^{8, 13} However, on a strong interacting catalyst, like Ni, p-type doping effect has been observed.¹⁷ We expect PdGr system in this study would exhibit doping shifts in its Raman signal. We verify the doping effect from Pd substrate by comparing Raman spectra (532 nm, 15s) of a transferred graphene on SiO₂ and on Pd substrate, as shown in Figure 4.12. The blue squares are correlation of ω_G and ω_{2D} from a hexagonal graphene monolayer

transferred on SiO₂ substrate shown in Figure 4.5 (region I). They are very close to the reported pristine graphene with no strain and no doping under 532 nm Raman spectroscopy.²⁸ The black solid line represents the strain only effect,⁹ while the blue line stands for the p-type doping only effect in graphene from literature.^{28,29} Raman signals for another graphene monolayer transferred onto a clean Pd substrate (region II) are shown as the red circles and within $\varepsilon = 0 - 0.1\%$ region in Figure 4.12. This is reasonable given the lack of atomic conformability of a transferred graphene on polycrystalline Pd substrate. Raman signals reflect the phonon scattering modes in graphene layer and indicate the absence of graphene-substrate interaction. In some areas, graphene appears to be slightly stretched (similar to discussions in section 4.2) which could be due to the formation of anchoring points during the transfer process. Annealing at 300°C for one hour helps to increase the conformability at the graphene-Pd interface and hence relax the tension in graphene, as shown as the green stars. Notably, some graphene-Pd contact points show blue shift along the doping line with the electron concentration $n = 1 - 2 \times 10^{13} \text{ cm}^{-2}$. In light of this observation, we can quantify the strain configuration of as-grown graphene on Pd leaf by isolating its Raman signals from the Pd doping. This doping effect for the Pd substrates can be identified from the $\omega_G - \omega_{2D}$ correlation by offsetting the strain line along the p-type doping line to $1 - 2 \times 10^{13} \text{ cm}^{-2}$.

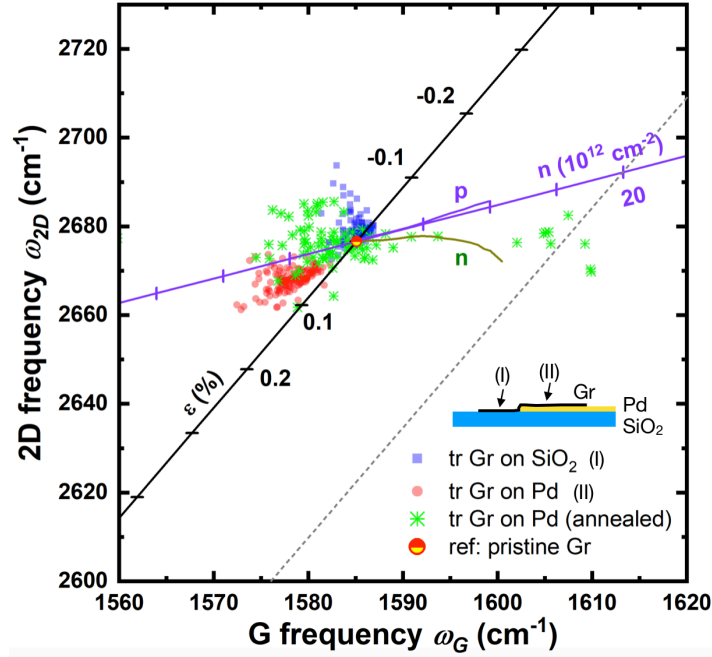


Figure 4.12. Correlation between the frequencies of the G and 2D Raman modes of graphene.

The data are obtained from Raman mapping of transferred graphene (tr Gr) on SiO₂ and Pd substrate. Green stars are from the same area of tr Gr on Pd substrate but has been annealed at 300°C for one hour. Here, we take $\omega_G = 1585.1 \text{ cm}^{-1}$ and $\omega_{2D} = 2676.6 \text{ cm}^{-1}$ for pristine Gr with no strain and no doping.²⁸ Solid P-type and n-type doping lines and the blue doping line are extracted from reference, assuming $\frac{\partial \omega_{2D}}{\partial \omega_G|_{h^+}} = 0.55$.²⁸ The black strain line is from first principle

$$\text{calculation assuming } \frac{\partial \omega_G}{\partial \varepsilon} = -58 \text{ cm}^{-1}/\%, \text{ and } \frac{\partial \omega_{2D}}{\partial \varepsilon} = -144 \text{ cm}^{-1}/\%.$$

Firstly, we compare the native strain in graphene monolayer grown on a low index Pd surface (flat region, map-1) and that on a high index surface (step region, map-2) on the same PdGr sample, as shown in Figure 4.13. The data points are clearly clustered into two groups. The blue squares which represent graphene on map-1 have a strain distribution from -0.1 to 0.2 %, whereas the red rectangles for map-2 lie between 0.2 to 0.4 %. This suggests graphene is in

tension within most of the locations on both maps, and is stretched more on the areas having surface reconstruction steps. While this experimental result - namely that graphene is in interfacial tension - may appear contradictory to theoretically predicted strain of graphene on Pd (111),²⁰ the polycrystalline Pd grain structure provides a possible explanation. Graphene can be in tension on some crystalline orientations of Pd, but unfortunately, to date this has not been theoretically studied to our knowledge. At the time of writing this dissertation, our research group started collaborating with Prof. Harley Johnson from UIUC to make these theoretical calculations. Nonetheless, based on experimental data, we can measure the presence of tension in graphene. This tension can be qualitatively explained by comparing the total energy – namely the elastic energy in graphene and surface energy at the Pd-Gr interface - in these two regions, see schematics in Figure 4.14. Given that Pd substrate contracts during the CVD cooling step after growth, and based on measurement of interfacial tension at room temperature, graphene must have been in higher tension at high temperature as well as the carbon crystallizes into graphene on Pd lattice. During cooling, graphene tends to relax its elastic strain while it interacts with the faceted Pd substrate. If a flat PdGr configuration (Pd orientation II in Figure 4.14) has less total energy (strain + surface) than that in a ridged PdGr (orientation I), Pd surface would remain flat and graphene can relax more tension strain until it becomes neutralized. On the other hand, if a ridged PdGr configuration has less total energy, tiny roughness on Pd surface would bunch and form larger steps or terrace. And in this case, pre-stretched graphene which conforms on Pd surface, cannot be fully relaxed, resulting in residual tension strain in it on step region. Notably, the observed hierarchical steps with a dominant direction would break the biaxial straining in graphene. As a result, graphene can contract or expand in the orthogonal direction, helping to form secondary small surface steps.

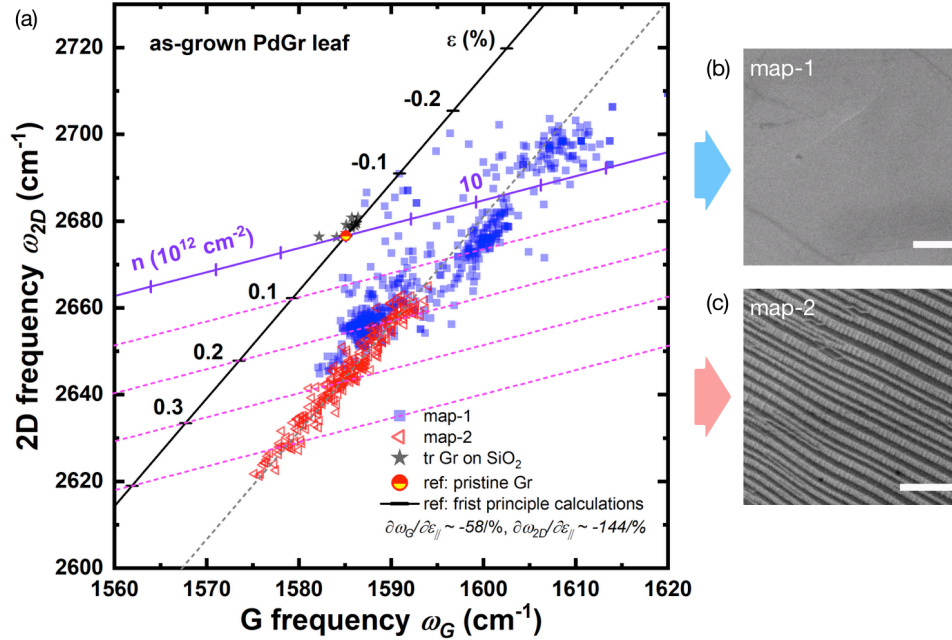


Figure 4.13. Correlation between the frequencies of the G and 2D Raman modes of graphene grown on Pd leaf. Inset SEM images show that the flat region on PdGr surface has larger ω_G and ω_{2D} than those in the terrace region. Scale bars: 1 μm . The strain line is from first principle calculation assuming biaxial strain with $\frac{\partial\omega_G}{\partial\epsilon} = -58\%$ and $\frac{\partial\omega_{2D}}{\partial\epsilon} = -144\%$.⁹ Solid P-type and n-type doping lines and the blue doping line are extracted from reference, assuming $\frac{\partial\omega_{2D}}{\partial\omega_G|_{h^+}} =$

$$0.55.^{28}$$

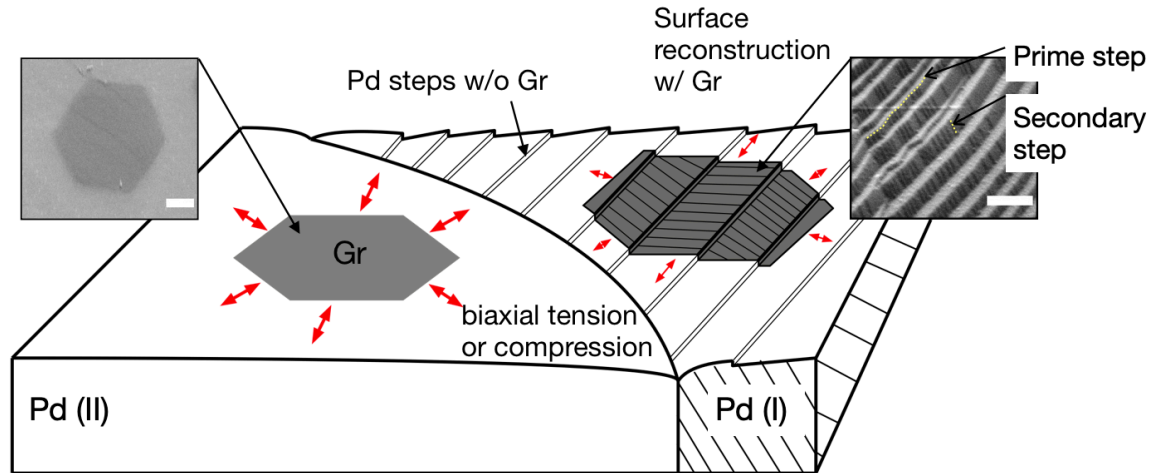


Figure 4.14. Schematic of surface reconstruction on PdGr and strain relaxation in graphene on polycrystalline Pd substrate. Insets are typical example SEM images for the flat and step-bunched PdGr surfaces. Scale bar for Pd II case: 1 μm and for Pd I case: 500 nm.

This observation is quite consistent on as-grown PdGr thin film composites in this study. Figure 4.15 gives another example of graphene monolayer across Pd ($\bar{2}\bar{1}1$) (with a miscut angle $\alpha = 9.9^\circ$) and Pd (010) ($\alpha = 6.5^\circ$). Figure 4.15a and 4.15b compare the frequencies (ω) and full width at half maximum (FWHM, Γ) for G and 2D Raman modes respectively. Region II shows larger frequencies in both modes and a little wider FWHM. This is clear sign that Region II is in compression with respect to tension in region I. Correlation of SEM image (Figure 4.15c) with the strain map (Figure 4.15d) confirms this.

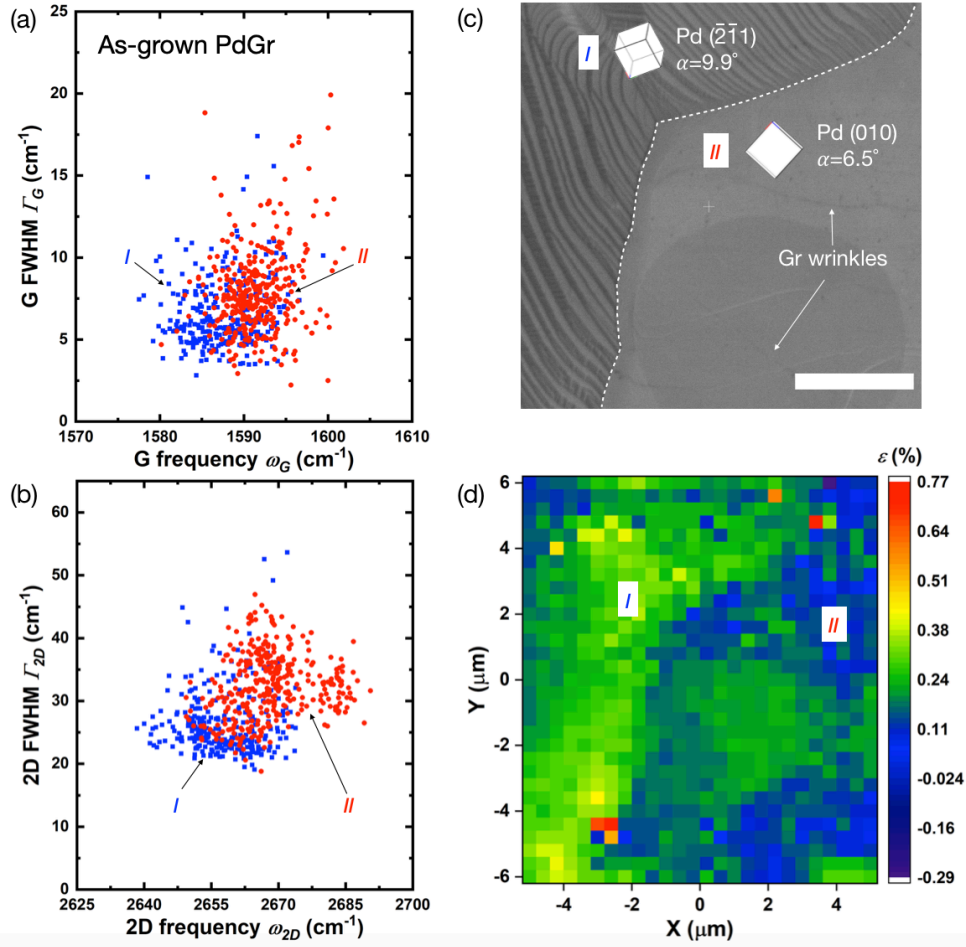


Figure 4.15. Strain relaxation of CVD grown graphene on polycrystalline Pd. (a) $\Gamma_G - \omega_G$ correlation shows region II has comparable FWHM but higher frequency compared to region I. (b) $\Gamma_{2D} - \omega_{2D}$ shows region II has wider FWHM and higher frequency compared to region I. (c) SEM image of region I and II. Scale bar: 2 μm . (d) Corresponding strain map assuming biaxial strain with $\frac{\partial \omega_G}{\partial \varepsilon} = -58/\%$ and $\frac{\partial \omega_{2D}}{\partial \varepsilon} = -144/\%$ and a reference location at $\omega_G = 1589.8 \text{ cm}^{-1}$.

In addition, we have started characterization of the cross sections of PdGr surface reconstructions in TEM for more insights. The preliminary results for a graphene covered region on the Pd leaf are displayed in Figure 4.16. It can be clearly observed that Pd surface becomes faceted after graphene covered (Figure 4.16a and 4.16b). The dimensions of surface steps in Figure 4.16b

agree with the observations in AFM presented in Figure 4.10. A selected area electron diffraction (SAED) shown in Figure 4.16c for this sample confirms the single crystal structure in Pd substrate. A zoomed-in look at the PdGr step surface shows the secondary steps which are formed probably due to the graphene elasticity. Interestingly, the newly-formed rising surfaces of these tiny steps are on Pd $\{111\}$ planes. These observations need to be compared with simulations results from Prof. Harley Johnson to drive more comprehensive understanding of the graphene-metal interfacial interactions.

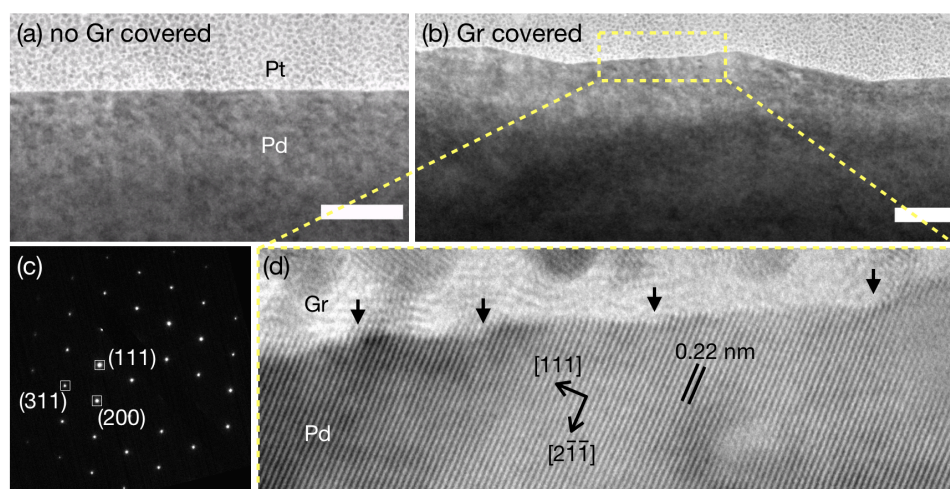


Figure 4.16. (a-b) Cross sectional TEM images show the flat Pd surface for non-graphene-covered region and the reconstructed PdGr surface for graphene-covered region. Scale bar: 50 nm. (c) SAED corresponding to (b), showing single crystal structure near Pd surface after graphene synthesis. (d) Zoomed-in TEM image showing the secondary steps. Notably, the nearly-formed step surfaces (the secondary steps which marked by arrows) are on Pd $\{111\}$.

4.4. Conclusions

Graphene-metal interface conformability is a multiscale problem spanning the grainsize (microscale) to the atomic scale, and results in a rich plethora of strain configurations. We have studied these problems by synthesizing pristine graphene monolayers on a strongly interacting metal, namely Pd. AMFM-AFM and Raman spectroscopy are used to characterize the interface conformability and native strain level in graphene. Biaxial tension up to 0.4 % is observed in graphene grown on Pd leaves. This straining is caused by free energy minimization in PdGr system including the surface and elastic energies, and is strongly related to the kinetics of the graphene's pretension relaxation during CVD cooling stage.

4.5. References:

1. Huang, B.; Koh, Y. K. *Carbon* **2016**, 105, 268-274.
2. Zhang, K.; Poss, M.; Chen, P.-J.; Tawfick, S. *Advanced Engineering Materials* **2017**, 19, (12), 1700475.
3. Kim, Y.; Lee, J.; Yeom, M. S.; Shin, J. W.; Kim, H.; Cui, Y.; Kysar, J. W.; Hone, J.; Jung, Y.; Jeon, S.; Han, S. M. *Nat Commun* **2013**, 4, 2114.
4. Chen, Y.; Zhang, X.; Liu, E.; He, C.; Shi, C.; Li, J.; Nash, P.; Zhao, N. *Scientific Reports* **2016**, 6, 19363.
5. Labuda, A.; Kocun, M.; Meinhold, W.; Walters, D.; Proksch, R. *Beilstein Journal of Nanotechnology* **2016**, 7, 970-982.
6. Malard, L. M.; Pimenta, M. A.; Dresselhaus, G.; Dresselhaus, M. S. *Physics Reports* **2009**, 473, (5), 51-87.
7. Mueller, N. S.; Heeg, S.; Alvarez, M. P.; Kusch, P.; Wasserroth, S.; Clark, N.; Schedin, F.; Parthenios, J.; Papagelis, K.; Galiotis, C.; Kalbáč, M.; Vijayaraghavan, A.; Huebner, U.; Gorbachev, R.; Frank, O.; Reich, S. *2D Materials* **2017**, 5, (1), 015016.
8. Ding, F.; Ji, H.; Chen, Y.; Herklotz, A.; Dörr, K.; Mei, Y.; Rastelli, A.; Schmidt, O. G. *Nano Letters* **2010**, 10, (9), 3453-3458.
9. Mohiuddin, T. M. G.; Lombardo, A.; Nair, R. R.; Bonetti, A.; Savini, G.; Jalil, R.; Bonini, N.; Basko, D. M.; Galiotis, C.; Marzari, N.; Novoselov, K. S.; Geim, A. K.; Ferrari, A. C. *Physical Review B* **2009**, 79, (20), 205433.
10. Zabel, J.; Nair, R. R.; Ott, A.; Georgiou, T.; Geim, A. K.; Novoselov, K. S.; Casiraghi, C. *Nano Letters* **2012**, 12, (2), 617-621.
11. Yoon, D.; Son, Y.-W.; Cheong, H. *Nano Letters* **2011**, 11, (8), 3227-3231.
12. Kang, J. H.; Moon, J.; Kim, D. J.; Kim, Y.; Jo, I.; Jeon, C.; Lee, J.; Hong, B. H. *Nano Lett* **2016**, 16, (10), 5993-5998.
13. Li, B.-W.; Luo, D.; Zhu, L.; Zhang, X.; Jin, S.; Huang, M.; Ding, F.; Ruoff, R. S. *Advanced Materials* **2018**, 30, (10), 1706504.
14. Gao, L.; Ren, W.; Xu, H.; Jin, L.; Wang, Z.; Ma, T.; Ma, L.-P.; Zhang, Z.; Fu, Q.; Peng, L.-M.; Bao, X.; Cheng, H.-M. *Nature Communications* **2012**, 3, 699.
15. Casiraghi, C.; Hartschuh, A.; Qian, H.; Piscanec, S.; Georgi, C.; Fasoli, A.; Novoselov, K. S.; Basko, D. M.; Ferrari, A. C. *Nano Letters* **2009**, 9, (4), 1433-1441.
16. Graf, D.; Molitor, F.; Ensslin, K.; Stampfer, C.; Jungen, A.; Hierold, C.; Wirtz, L. *Nano Letters* **2007**, 7, (2), 238-242.
17. Usachov, D. Y.; Davydov, V. Y.; Levitskii, V. S.; Shevelev, V. O.; Marchenko, D.; Senkovskiy, B. V.; Vilkov, O. Y.; Rybkin, A. G.; Yashina, L. V.; Chulkov, E. V.; Sklyadneva, I. Y.; Heid, R.; Bohnen, K.-P.; Laubschat, C.; Vyalikh, D. V. *ACS Nano* **2017**, 11, (6), 6336-6345.
18. Dahal, A.; Batzill, M. *Nanoscale* **2014**, 6, (5), 2548-2562.
19. Kiraly, B.; Jacobberger, R. M.; Mannix, A. J.; Campbell, G. P.; Bedzyk, M. J.; Arnold, M. S.; Hersam, M. C.; Guisinger, N. P. *Nano Letters* **2015**, 15, (11), 7414-7420.
20. Khomyakov, P. A.; Giovannetti, G.; Rusu, P. C.; Brocks, G.; van den Brink, J.; Kelly, P. J. *Physical Review B* **2009**, 79, (19), 195425.
21. Na, S. R.; Wang, X.; Piner, R. D.; Huang, R.; Willson, C. G.; Liechti, K. M. *ACS Nano* **2016**, 10, (10), 9616-9625.

22. Frank, O.; Tsoukleri, G.; Parthenios, J.; Papagelis, K.; Riaz, I.; Jalil, R.; Novoselov, K. S.; Galiotis, C. *ACS Nano* **2010**, 4, (6), 3131-3138.
23. Frank, O.; Vejpravova, J.; Holy, V.; Kavan, L.; Kalbac, M. *Carbon* **2014**, 68, 440-451.
24. Yi, D.; Luo, D.; Wang, Z.-J.; Dong, J.; Zhang, X.; Willinger, M.-G.; Ruoff, R. S.; Ding, F. *Physical Review Letters* **2018**, 120, (24), 246101.
25. Kaghazchi, P.; Jacob, T.; Ermanoski, I.; Chen, W.; Madey, T. E. *Journal of Physics: Condensed Matter* **2012**, 24, (26), 265003.
26. Giovannetti, G.; Khomyakov, P. A.; Brocks, G.; Karpan, V. M.; van den Brink, J.; Kelly, P. *J. Phys Rev Lett* **2008**, 101, (2), 026803.
27. Neumann, C.; Reichardt, S.; Venezuela, P.; Drögeler, M.; Banszerus, L.; Schmitz, M.; Watanabe, K.; Taniguchi, T.; Mauri, F.; Beschoten, B.; Rotkin, S. V.; Stampfer, C. *Nature Communications* **2015**, 6, 8429.
28. Froehlicher, G.; Berciaud, S. *Physical Review B* **2015**, 91, (20), 205413.
29. Lee, J. E.; Ahn, G.; Shim, J.; Lee, Y. S.; Ryu, S. *Nature Communications* **2012**, 3, 1024.

CHAPTER 5: ELASTIC PROPERTIES OF GRAPHENE-COATED THIN METAL FILMS

Abstract

Successful synthesis of high-quality graphene on ultrathin metal films allows us to investigate the mechanical reinforcement from graphene layer in thin film composites. We firstly adopt the widely used membrane nanoindentation method to test the elastic behaviors of the circularly clamped as-grown multilayer graphene-Ni (Ni-MLG) thin films. For monolayer graphene-metal, like PdGr leaf by rapid CVD synthesis, we use a modified Hertz contact model to analyze the shallow (≤ 1 nm) indentation via atomic force microscope (AFM) on the supported PdGr thin film on SiO₂ substrate. Furthermore, we develop a numerical analysis route to precisely extract the elastic properties of freestanding thin films via microbridge nanoindentation. Specially, we synthesize high-quality graphene on freestanding ultrathin Pd films (30 – 300 nm thickness) via the rapid CVD process which has been developed in Chapter 3, and discuss the size effects on PdGr elastic properties. It is found that the elastic modulus of an ultrathin Pd film can be significantly enhanced by merely monolayer-bilayer graphene synthesis. And this elastic enhancement is inversely dependent of thin film thickness. We attribute this extraordinary elastic enhancement to the considerable graphene-metal interfacial stresses installed during CVD synthesis, which has been discussed in Chapter 4. It is known that surface and residual stress can effectively boost up the elastic modulus in the material on atomic scales, whereas this stress tuning effect is usually imperceptible on most thin film materials as the thickness is beyond 10 nm. In this chapter, we demonstrate the surface stress effect in thin Pd film within 200 nm by merely graphene synthesis.

5.1. Introduction to the elasticity of thin film materials

5.1.1. Surface stress effect in nanoscale elasticity

Materials with reduced dimensions such as nanowires, nanotubes and ultrathin films are suitable for applications requiring folding and stretching, since the flexural rigidity decreases cubically with thickness.¹ By virtue of this stretchable geometry, ultrathin interconnects and electrical lines shaped like springs are finding applications in almost all novel flexible devices like flexible display, electronic textile, health care, human–machine interaction, to name a few.¹⁻³ It is hence important to understand the mechanical behavior of ultrathin film materials and more specifically, to design new thin films having precisely controlled elastic properties. Mechanical degradation or failure of thin metal connections in flexible electronics would lead to a shorter lifetime or make device vulnerable to complete failure. In addition to design complex stretchable wavy structures, ultrathin film materials mechanical property reinforcement may guarantee a device’s long lifetime intrinsically. Strain-engineering of crystalline catalyst materials such as Pd is also another novel use of very thin films⁴ where it is found that large compressive strains imparted due to interfacial energy can strongly tune the chemical reactivity.

On one hand, materials exhibit exceptional mechanical behaviors when the dimensions of the structure approach some critical length scale of the material. Wong et al. have measured the elastic bending stiffness of SiC nanorods and multiwall carbon nanotubes (MWNTs) and observed spring force constant dependence on material diameters.⁵ Poncharal et al. have also measured the increased elastic bending moduli of MWNTs with reduced diameters.⁶ As for metals, Cuenot et al. have measured the elastic moduli of silver and lead nanowires and noticed increase in the elastic modulus as the wire diameter decreases.⁷ For hard materials like diamond, Banerjee et al. recently

demonstrated the increase in the elastic strain limit by 9% by shrinking the diamond rod diameter to nanoscale.⁸ These experiments provide direct evidence for what is known as “scale effects” where the elastic properties of materials depend on size in the nanometer range. For materials with macroscopic sizes, the mechanical properties are controlled by the elastic strain energy, whereas at sub nanometer length scales, due to the increasing surface-to-volume ratio, surface effects including surface stresses^{7,9,10} and surface toughness⁸ become predominant and can significantly modify material properties. It should be noted that surface elasticity of a solid body -related to surface stresses or tractions- is the reversible work per unit area needed to elastically stretch a preexisting surface and is a function of -but not equivalent to- material’s surface energy.¹¹ Bare elementary crystals usually have low surface energies, e.g. Ni (110): 2.44 Jm⁻², Mo (110): 2.07 Jm⁻², Si (110): 1.39 Jm⁻².¹² Pd (110) has surface energy around 1.6 J m⁻²,^{12, 13} and imperceptible thickness dependence when Pd is thicker than 10 nm.¹¹ However, as demonstrated in this study, the effective surface modulus of graphene-coated metals can reach higher values than the surface energy leading to greater increase in the measured bulk modulus.

In this study, we propose a new route to reinforce the elastic constant of thin metal nanoribbons by directly growing graphene on the metal surface. We synthesize high-quality graphene wrapping around ultrathin palladium (Pd) nanoribbons via a rapid Chemical Vapor Deposition (CVD) process which has been developed in our previous study,¹⁴ and observe the size dependent elastic modulus in palladium graphene (PdGr) composite thin films. Graphene is a 2D surface of sp²-hybridized carbon atoms, has an extremely high in-plane mechanical stiffness. Incorporating high quality graphene on the surface of metal structures as a laminated composite is a promising way to exploit its properties for applications.¹⁵⁻¹⁷ In this case, the graphene acts as an increased surface

modulus of the nanoribbons and due to its high modulus, it affects the mechanical stiffness of the nanoribbons. Further, the interface between the Pd and the graphene experiences residual stresses due to the mismatch between the lattice spacing and the thermal expansion coefficients of graphene and the metal.¹⁸⁻²¹ For example, the synthesis-induced pre-strain in graphene can be up to 0.40 % compression in graphene-Cu epitaxial region like Cu (111).²¹ We exploit the higher interfacial stress in lattice mismatched systems, like graphene-Pd and exploit this large surface stresses in seed metal to modulate the elastic moduli of the composite nanoribbon.

5.1.2. Mechanical property measurement for thin film materials

To verify thin film mechanical properties, there are extensive studies on testing the mechanical behaviors at nanometer to micrometer scale either they are free-standing^{22, 23} or on substrates.^{24, 25} Nanoindentation measurements have been successfully used to acquire the elastic and fracture properties of ultrathin materials like graphene monolayer membrane,²⁶ graphene ribbons,²⁷ graphene oxide sheets²⁸ and ultrathin metal films^{24, 29, 30} for its high spatial resolution and load sensitivity. A nonlinear load-displacement dependence is used to fit the indentation data and derive the elastic Young's modulus and other mechanical properties. Nevertheless, three factors may cause the uncertainty in the indentation data analysis for graphene-metal thin film composites. Firstly, when indenting on the supported graphene-metal thin films on the rigid substrate, the high inhomogeneity of this composition and the anisotropy between graphene's in-plane and perpendicular-to-the-plane properties can make the traditional Hertz contact mechanics not suitable to model the deformation between the indenter tip and graphene-metal surface, because the Hertz contact model is originally valid only for isotropic half-spaces.³¹ Second, for freestanding circularly clamped graphene-metal membrane or doubly clamped microbridge, sample's slackness

or graphene wrinkles in the beginning of indentation may cause softening effect to data analysis. The third factor, especially for metallic materials, is the strain hardening effect due to inelastic deformation in thin films with large deformation. The existing load-displacement dependence for the elastic membrane bending-stretching deformation fails to yield reliable modulus values from indentation data affected by the last two factors. In this study, we firstly adopt the widely used circularly clamped membrane indentation method to test the elastic behaviors of as-grown Ni-MLG thin film discussed in the previous chapter. For monolayer graphene-metal, like PdGr leaf by rapid CVD synthesis, we use a modified Hertz contact model³² to analyze the shallow (<1 nm) indentation via atomic force microscope (AFM) on the supported PdGr thin film on SiO₂ substrate. Furthermore, we develop a modified numerical analysis route to precisely extract the elastic properties of a freestanding ultrathin film. We synthesize high-quality graphene on freestanding ultrathin Pd films via a rapid CVD process which has been developed in previous study,¹⁴ and analyze the size effects on PdGr elastic properties.

5.2. The elasticity enhancement in CVD grown Ni-MLG thin film composites

As discussed in Chapter 2, the CVD-grown Ni-MLG films can be delaminated from the SiO₂ substrate by slowly submerging into water, and then transferred onto a rigid substrate with $\phi 160$ μm perforation. We use a spherical diamond indenter having 5 μm diameter and cone angle of 60° to indent the center of the clamped freestanding Ni-MLG membrane, as sketched in Figure 5.1. The force (load) and membrane deflection (displacement) are directly measured from the Hysitron TI-950 Triboindenter. The transducer resolution is 1 nN for load and 0.02 nm for displacement. Load-control mode is used with pre-loading of 2 μN and loading rate of 80 $\mu\text{N s}^{-1}$.

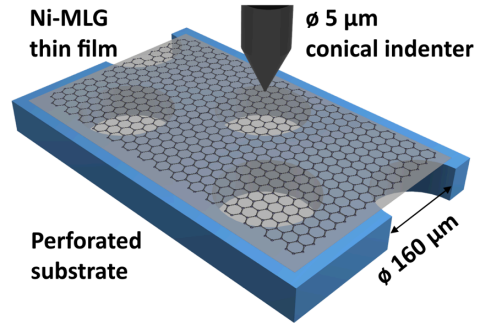


Figure 5.1. Schematic of nanoindentation on a circularly clamped freestanding Ni-MLG thin film.

Figure 5.2 shows the loading-unloading behaviors of as-grown Ni-MLG thin film with peak loads of 20, 30 and 100 μN . From the shape of unloading curves, we identify that a load below 20 μN and displacement less than 1000 nm retains the elastic deformation in membrane. Higher loads than this, like #3, demonstrate measureable hysteresis that we attribute to limited Ni plasticity, slip within MLG layers and interfacial slip between MLG and underlying Ni. In order to investigate the mechanics at graphene and Ni interface, we test the as-grown Ni-ML, MLG (i.e. Ni etched from Ni-MLG using FeCl_3/HCl etchant) and the control samples of deposited Ni by sputtering (thickness: 155.2 nm) and Ni-C (i.e. MLG etched Ni-MLG using O_2 reactive ion etching (RIE)).

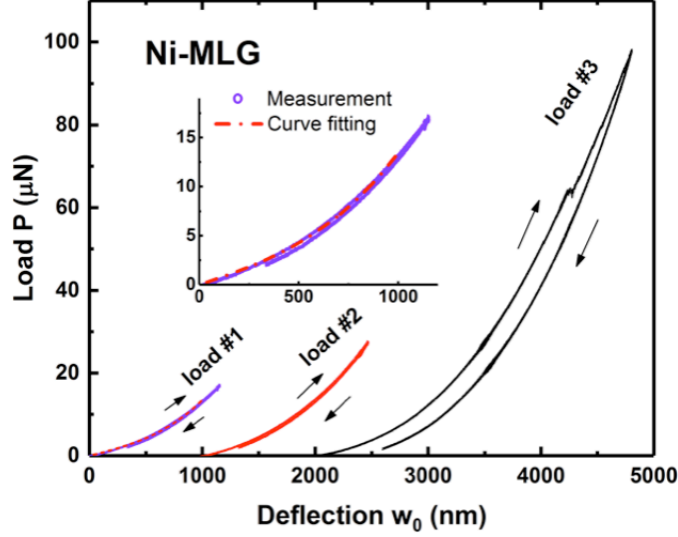


Figure 5.2. Typical loading-unloading curves for freestanding Ni-MLG membrane, showing the elastic regime for curve fitting and hysteresis at large membrane deflections. (Load #1: 0-20 μN , load #2: 0-30 μN and load #3: 0-100 μN . There is 1 μm offset in w_0 between different loading cycles.)

Figure 5.3a and 5.3b display the typical load-displacement curves of freestanding Ni-MLG, MLG and bare Ni. We carry out extensive nanoindentation studies using loads ranging from 20 to 800 μN , all the way until membrane fracture. In this chapter, we mainly focus on the loading-displacement curves in the elastic regime ($w_0 < 1000$ nm). Notably, in the range where the ratio of indenter tip diameter (c) to membrane diameter (a) is small ($c/a \ll 1$), the analytical description of a clamped circular thin film under central point load with a prestrain (due to residual stress in transfer process) can apply for analysis.³³ A continuum mechanics model capturing the bending-stretching deformation in thin films can be expressed as Equation 5.1:

$$P = \frac{4\pi E h^3}{3(1-\nu^2)a^2} w_0 + \frac{2\pi\sigma_0 h}{\ln(a/c)} w_0 + \frac{Eh}{a^2 f_v^3} w_0^3 \quad (5.1)$$

where P and w_0 are the applied load and thin film central displacement, a and c are radius of thin film and indenter tip, h is thin film thickness, E and ν are the elastic modulus and the Poisson's ratio, σ_0 is the residual stress in the clamped thin film due to biaxial stretching during transfer process, and f_ν is the function of Poisson's ratio as $1.0491 - 0.1462\nu - 0.1583\nu^2$.³⁴ Equation 5.1 combines plate-bending behavior within the first two linear terms and membrane stretching behavior represented by the third nonlinear term. E and σ_0 are calculated by least square fitting of the measured indentation data. In our experiments, membrane deflection is large due to the large membrane size, small indenter tip and thin sample thickness, thus the nonlinear term in Equation 5.1 turns to be more significant and it governs the curve shape in Figure 5.3a and 5.3b. Figure 5.3c summarizes the calculated elastic moduli for all type of membranes using Equation 1. As-sputtered Ni film has the elastic modulus of $E_{\text{Ni}} = 158.5 \pm 7.4$ GPa, which is 79 % of the bulk values of Ni (200 GPa). This discrepancy can be mainly caused by the surface roughness of the sputtered Ni films resulting in difficulty in accurate estimation of thin film thickness for its mechanics. The tested thin Ni circular membrane in this study have very large diameter to thickness ratio and a large number of columnar grains ($\sim 8.6 \times 10^7$). For the MLG membrane (Ni-etched), the elastic modulus is $E_{\text{MLG}} = 629.3 \pm 3.2$ GPa, which is 62.9 % of the intrinsic modulus of graphene monolayer.²⁶ We believe that the behavior of these MLG films is more indicative measure of the expected behavior of graphene with realistic quality and defect densities. It is notable that at large load values, discontinuities in the load-displacement data indicate the initiation and stable propagation of nanocracks in MLG, shown as the dips in Figure 5.3b. As for as-grown Ni-MLG composites, we use the values calculated from the 10-min synthesis duration, which shows the highest mechanical performance. In this case, the MLG thickness is 10.9 nm, which corresponds to Ni-MLG composite having 7.4 vol % MLG. The result is $E_{\text{Ni-MLG}} = 285.2.3 \pm 13.6$ GPa,

representing 79.9 % increase over those for bare Ni, indeed confirming reinforcement beyond the rules of mixture bounds. To further understand the origin of these enhancement, we test Ni-C (MLG etched) and obtain very close elastic modulus value of $E_{\text{Ni-C}}$ compared to E_{Ni} , but ~6.1 % increase in strength than that of as-sputtered Ni (we will discuss this in the following chapter). The difference between Ni-C and Ni can be attributed to carbon solid solution strengthening by dissolved carbon atoms and carbide phase formation (will be discussed later in this chapter). In addition, the MLG-on-Ni thin film (transferred MLG onto Ni-C), with absence of graphene-metal interfacial strength, also exhibits very similar elastic modulus as E_{Ni} . These observations clearly suggest that the observed elastic enhancement in Ni-MLG composites stems from superb properties of graphene including the graphene-metal interface from CVD synthesis. We will discuss this in more details in Pd-Gr system in this chapter.

The mechanical properties of Ni-MLG composites with different MLG thickness are also investigated. Figure 5.3d shows the dependence of $E_{\text{Ni-MLG}}$ on MLG thickness. We observe a trend that films having 10.9 nm average MLG thickness (10-min growth case in Chapter 3) have the highest elastic modulus. This is because of the reason that shorter growth time (< 10 min) cannot yield fully covered MLG on Ni, while the longer growth usually results in non-uniformities in MLG.

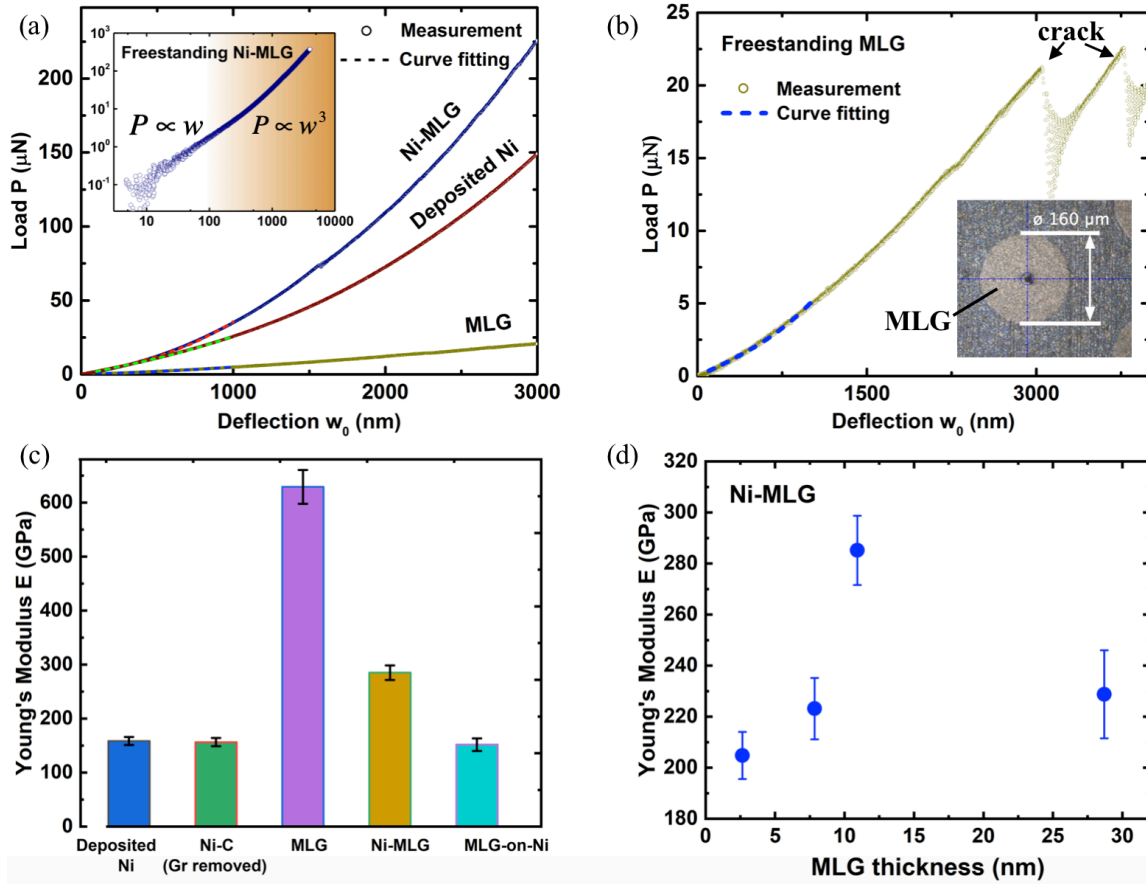


Figure 5.3. Mechanical behaviors of freestanding Ni-MLG membranes. (a) raw loading-displacement (central point) curves for freestanding Ni-MLG, bare Ni and MLG membranes. Note the difference between their thicknesses. Curve fitting using Equation 1 is used to extract the Young's modulus, and the logarithmic scale inset plot shows the slope change transition from bending-dominated deformation to membrane stretching as loading increases. (b) Load-displacement and curve fitting for freestanding MLG, in which micro-cracks initiate at high membrane deflections ($> 3 \mu\text{m}$). (c) Summary of the measured elastic moduli in the designed thin films. (d) Dependence of E of as-grown Ni-MLG on MLG thickness.

What should be mentioned is, we verify that Equation 5.1 can be applied to analyze the homogenized elastic properties of all of our films, including Ni-MLG laminated composites. In

Figure 5.4, we compare Equation 5.1 with finite element method (FEM) simulations using COMSOL,³⁵ and we verify that the difference between the homogenized composite and the multilayered composite membranes is small compared to other variations and experimental errors, which validates the applicability of Equation 5.1 for our analysis.

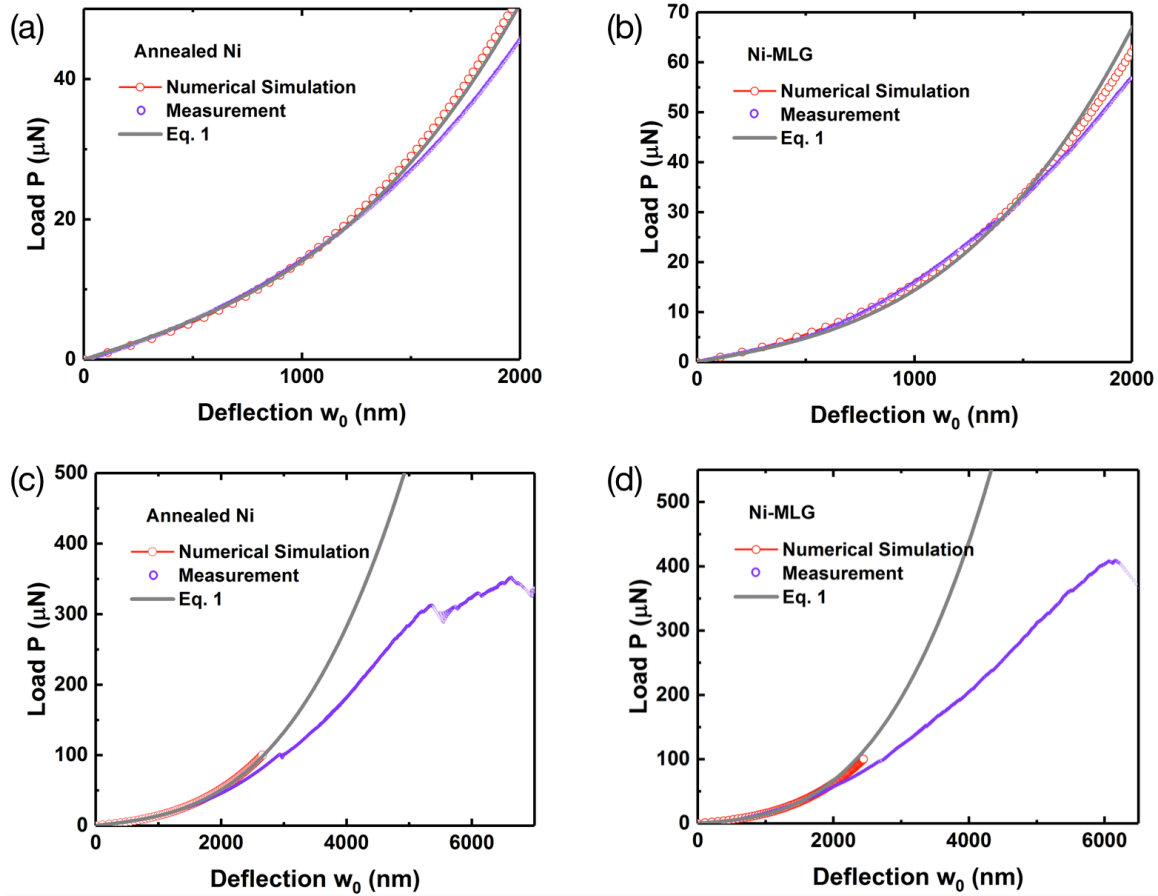


Figure 5.4. Comparison of load-displacement curves between nanoindentation experiments, COMSOL simulations and analytical calculations using Equation 1 for (a) annealed thin Ni film (removing graphene from Ni-MLG), (b) as-grown Ni-MLG thin film, (c) annealed Ni beyond the elastic regime, (d) Ni-MLG beyond the elastic regime. (Parameters used in calculations: 137.8 nm-thick Ni, 10.9 nm thick MLG, $E_{Ni} = 156.6$ GPa, $\nu_{Ni} = 0.31$, $\sigma_{0 Ni} = 32.8$ MPa, $E_{MLG} = 629.3$ GPa, $\nu_{MLG} = 0.16$, $\sigma_{0 NiMLG} = 30.0$ MPa)

5.3. The elasticity enhancement of CVD grown PdGr thin film composites

5.3.1. Indentation modulus increase by graphene monolayer synthesis

The possible interlayer sliding within MLG layer³⁶ and non-uniformity and high defect density in MLG³⁷ can cause additional softening effect to mechanical behaviors of graphene-metal nanocomposites. Considering this, we turn to Pd-monolayer graphene (Pd-Gr) leaf produced via the rapid CVD synthesis in chapter 3 for the following mechanical characterizations. Pd is selected as the metal substrate for graphene-metal thin film composites for the following reasons: (i) Pd has high melting point and high carbon solubility at the graphene synthesis temperatures. These properties allow us to synthesize high-quality graphene via a rapid CVD process without thin film dewetting.¹⁴ (ii) A large in-plane lattice mismatch between graphene and Pd ($\sim 3.3\%$ strain in Pd substrate) and large thermal expansion difference (Pd: $11.8 \times 10^{-6} \text{ K}^{-1}$ and Gr: $(-8.0 \pm 0.7) \times 10^{-6} \text{ K}^{-1}$)³⁸ which drive large residual surface stresses and give rise to interesting mechanical behavior.

Firstly, the elastic perpendicular-to-the-plane response of as-grown PdGr leaf is measured by indenting with a diamond-coated probe via AFM. Figure 5.5 shows the geometry of the AFM probe having a tip diameter of 100 nm.

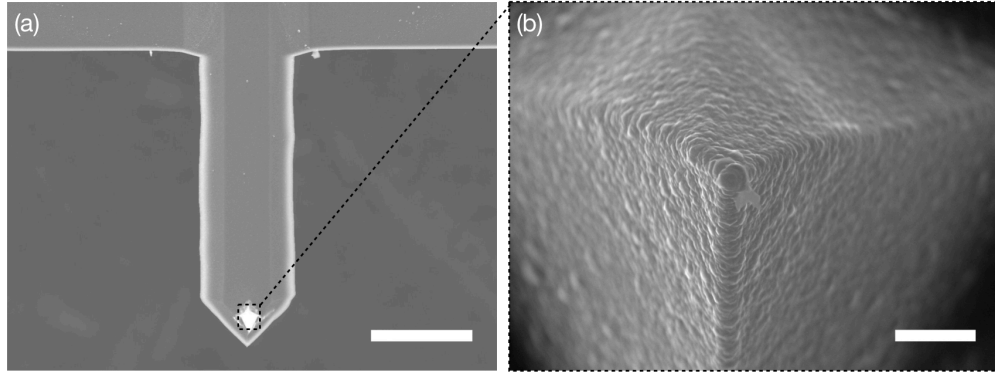


Figure 5.5. (a) SEM image of the AFM probe tip, which is made of diamond coated silicon. Scale bar: 50 μm . (b) The zoomed-in image showing the tip radius R of ~ 50 nm. Scale bar: 1 μm .

Figure 5.6a shows the force curves of bare Pd leaf, PdGr and PdC (no graphene covered region on PdGr sample). In this study, we present results using small loads of less than 150 nN, ensuring the elastic deformation at indentation displacement of less than 1 nm. The bare Pd leaf shows negligible hysteresis between loading and unloading curves, while PdGr composites show limited hysteresis possible due to PdGr interfacial slip. For sub-nm indentation, a continuum mechanics model based on Hertz contact theory³² can be utilized to estimate the effect perpendicular-to-the-plane elasticity from the unloading data: $F = \frac{4}{3} E_r \sqrt{R} \delta^{3/2}$, where F is the indentation load, δ is the displacement. $E_r = \left(\frac{1-\nu^2}{E} + \frac{1-\nu_t^2}{E_t} \right)^{-1}$, with $E_t = 1050$ GPa, $\nu_t = 0.2$ being the Young's modulus and the Poisson's ratio of the diamond tip. The effective modulus of PdGr leaf is 223.6 ± 23.4 GPa, which is close to 2.5-fold increase over the as-received bare Pd leaf, as shown in Figure 5.6b. This is an impressive stiffening effect considering that it is due to only a single monolayer added on the surface of an already stiff material ($E_{\text{Pd}} \sim 121$ GPa). We also report the effective modulus of areas on the same leaf, which underwent the CVD synthesis but have not been covered

with graphene, referred to as PdC. PdGr is stiffer than PdC by ~60 %. The origin of these difference is clearly from superb mechanical property of as-grown graphene monolayer and the defect-scarce Pd-Gr interfacial bonding.

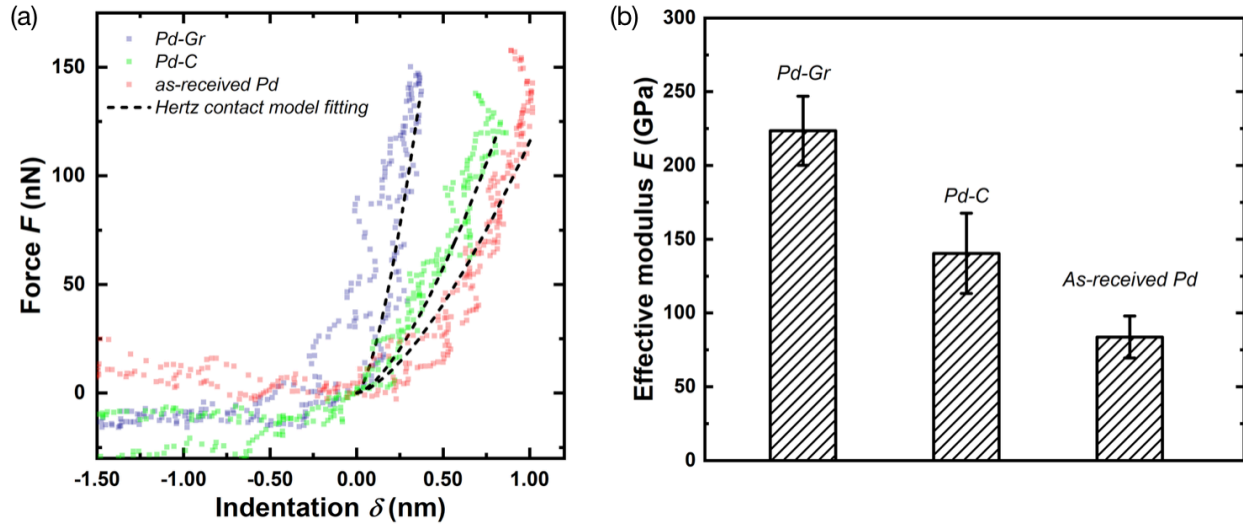


Figure 5.6. Mechanical behavior of as-grown PdGr leaves under AFM indentation. (a) Typical force curves of as-received Pd leaf, annealed PdC leaf and as-grown PdGr leaf. (b) The effective elastic moduli measured from AFM indentation, showing significant reinforcement in Pd thin film by monolayer graphene growth.

5.3.2. Fabrication of freestanding PdGr thin film composites

Pd is used as the metal substrate for graphene-metal composite nanoribbons for the following reasons: (i) Pd is an excellent catalyst, has a high melting point and high solid carbon solubility which makes it suitable for segregation-driven graphene synthesis. These properties allow us to fabricate high-quality graphene via a rapid CVD process while avoiding solid-state dewetting which challenges the stability of thin films at high temperatures.¹⁴ (ii) Graphene-Pd has large lattice mismatch (~ 3.3 % theoretically-predicted lattice mismatch compressive strain on Pd (111) surface)³⁹ and large thermal expansion mismatch (Pd: $11.8 \times 10^{-6} \text{ K}^{-1}$ and Gr: $(-8.0 \pm$

$0.7) \times 10^{-6} \text{ K}^{-1}$).³⁸ Figure 5.7 illustrates the fabrication processes of freestanding Pd-graphene (PdGr) composite nanoribbon for microbridge testing. A series of 4 μm -wide, 20 μm spaced thin Pd nanoribbon arrays with the thickness ranging from 36 nm to 300 nm are sputtered on a SiO_2 (300 nm)/Si substrate with deposition rate of 0.7 \AA s^{-1} at room temperature, as sketched in Figure 5.7a. The Pd nanoribbons are annealed at $550 \text{ }^\circ\text{C}$ for 3 hours in Helium environment. The annealing step leads to uniform columnar grain structures.¹⁷ We use PMMA as a carrier layer to transfer the Pd nanoribbon arrays on a SiO_2/Si TEM grid.⁴⁰ Notably, Pd films can readily delaminate from SiO_2 surface by dipping into 0.3 vol % hydrofluoric acid solution, due to the weak Pd- SiO_2 interfacial bonding. The TEM grid is made of SiO_2/Si and has a through slot with a 110 μm wide gap. The transferred Pd nanoribbon arrays are aligned and bridge the slot (Figure 5.7b). After transfer, the PMMA carrier layer can be removed by Ar- O_2 reactive ion etching (RIE), leaving the suspended ultrathin Pd nanoribbons on the slotted TEM grid. The whole sample is then loaded in a high temperature furnace ($1100 \text{ }^\circ\text{C}$) for graphene synthesis using a rapid CVD process, which has been developed in our previous study (Figure 5.7c).¹⁴ Scanning electron microscope (SEM) images in Figure 5.7d and 5.7e present the uniform morphologies of as-grown PdGr nanoribbons suspended over the TEM grid. We confirm that graphene coating wraps around freestanding Pd nanoribbons using transmission electron microscope (TEM) and Raman spectroscopy, as shown in Figure 5.7f and 5.7g. TEM images show that we get continuous bilayer graphene coating the Pd, and they conformably wrap the Pd surface. In some localized regions we see three layers but they are not continuous and their contribution to the overall behavior is minimal. At the same spot shown in Figure 5.7f, the characteristic Raman feature, the so-called G peak, lies at 1573 cm^{-1} confirming the sp^2 hybridized carbon on Pd nanoribbon.

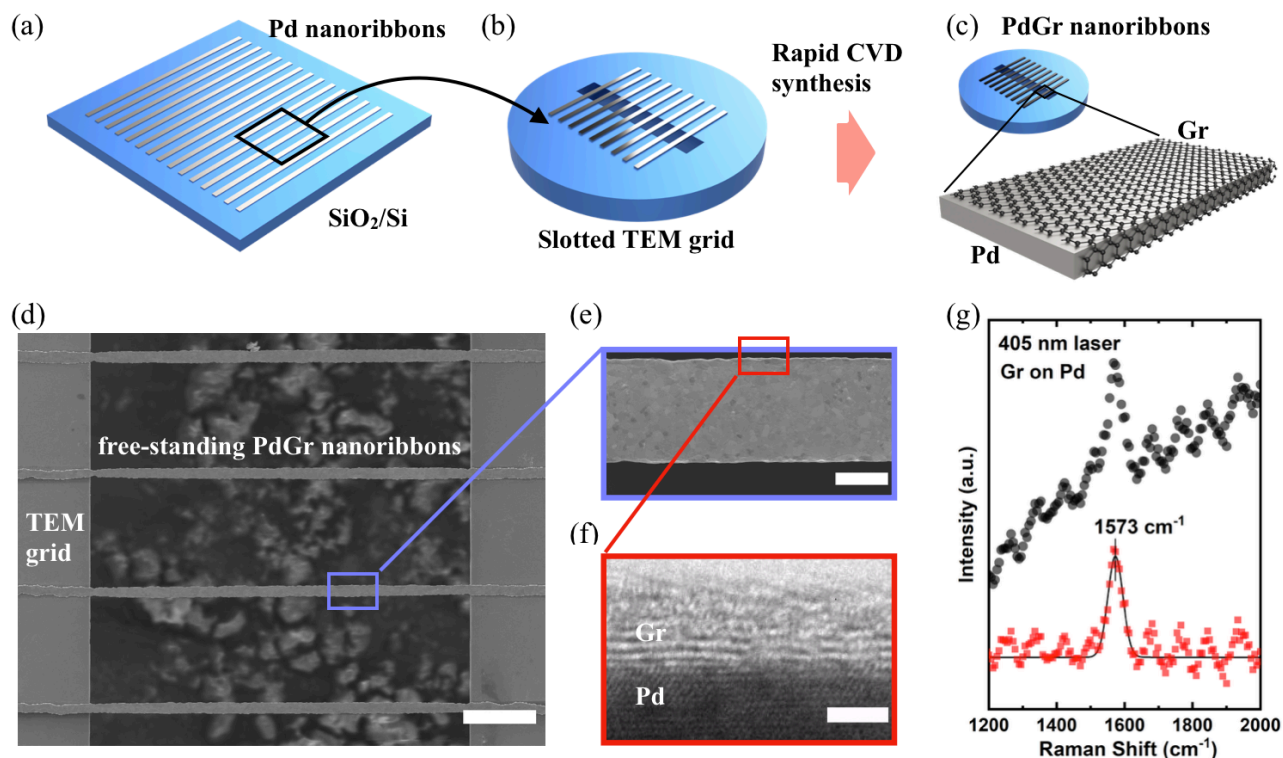


Figure 5.7. Fabrication of freestanding PdGr nanoribbons. (a) Schematic of the sputtered Pd nanoribbons on SiO₂/Si substrate. (b) Pd nanoribbons are transferred using PMMA carrier layer onto a TEM grid with a rectangular aperture opening. Transferred Pd nanoribbons are suspended across the slot and the PMMA layer can be removed by reactive ion etching (RIE). (c) Graphene is synthesized by Chemical Vapor Deposition (CVD) and wraps the freestanding Pd nanoribbons. (d) Scanning Electron Microscopy (SEM) image of the grown PdGr nanoribbons. Scale bar: 20 μm. (e) Higher magnification SEM. Scale bar: 2 μm. (f) Top view TEM image confirms that the nanoribbon is locally covered by continuous bilayer graphene conformable to the Pd surface, and a third layer is seen in some regions. Scale bar 2 nm. (g) Raman spectrum of the grown PdGr with G peak frequency at 1573 cm⁻¹ with excitation wavelength of 405 nm. Note that graphene's Raman signal is very weak when epitaxially layered on Pd.

Table 5.1. Dimensions of freestanding Pd and PdGr thin films measured in TEM (freestanding length: 105-110 μm)

Material	Width (μm)	Sample thickness (nm)	Gr thickness (nm)
Pd-1	4.8	38 ± 4	-
Pd-2	4.5	66 ± 6	-
Pd-3	4.2	80 ± 3	-
Pd-4	5.0	151 ± 6	-
Pd-5	4.7	253 ± 6	-
Pd-6	4.5	289 ± 8	-
PdGr-1	4.5	36 ± 3	0.65
PdGr-2	4.2	71 ± 5	0.65
PdGr-3	4.5	84 ± 5	0.97
PdGr-4	4.5	190 ± 5	1.28
PdGr-5	4.5	256 ± 8	0.65
PdGr-6	4.5	298 ± 7	0.65

5.3.3. Deflection of Pd and PdGr thin films in microbridge nanoindentation

We developed and validated a model to precisely determine the elastic modulus of nanoribbons in a non-ideal microbridge geometry. Freestanding Pd nanoribbons shown in Figure 1b usually have some slack on the TEM grid resulting during transfer. We measured the 3D profiles of freestanding Pd nanoribbons using a confocal laser profilometer (Keyence VK-X1000), as displayed in Figure 5.8a. Figure 5.8b shows a typical z-profile of a slack bare Pd nanoribbon. A wedge indenter (200 \pm 50 nm tip radius, 15 μm edge, 30° defining angle, Micro Star Tech.) applies a line loading in the

middle of a freestanding nanoribbon for the microbridge testing. On the other hand, stresses produced during the CVD synthesis remove the slack and result in slight taut nanoribbons, possibly due to thermal expansion mismatch between Pd and the SiO₂/Si substrate. Figure 5.8c and 5.8d show the 3D and z-profiles of as-grown PdGr nanoribbons with relatively taut morphology. Straining the slack of Pd nanoribbons during nanoindentation can cause a displacement drift Δh in load-displacement ($P - h$) measurement that can effectively soften the apparent stiffness during data analysis. This measurement uncertainty is nontrivial but frequently ignored in testing of freestanding thin films. In this study, we consider such displacement drift in microbridge nanoindentation model and develop a numerical analysis method to extract the elastic properties from indentation data properly.

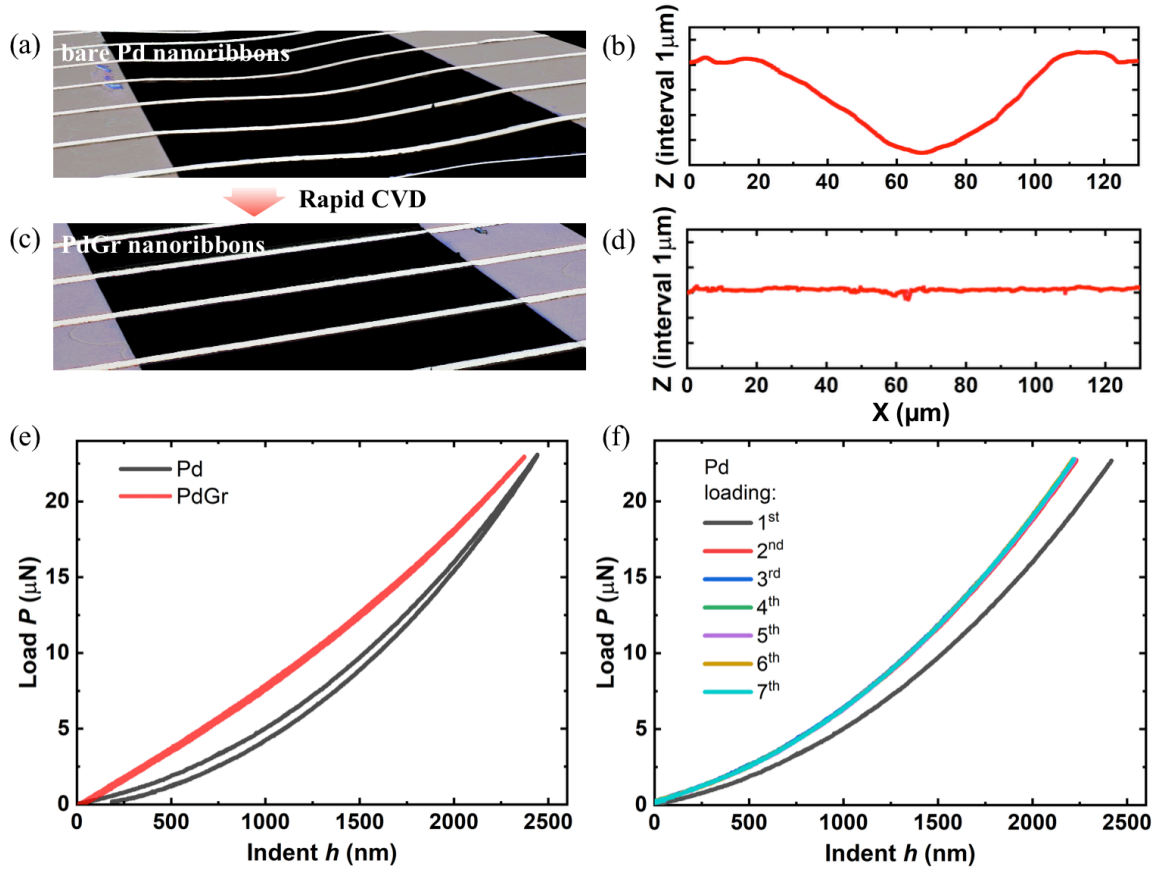


Figure 5.8. Nanoindentation on freestanding nanoribbons. (a) Measured 3D profile of freestanding Pd nanoribbons before CVD synthesis by laser confocal microscope. A wedge indenter applies line loading in the middle of each nanoribbon. (b) Typical Z-profile of a slack Pd nanoribbon. (c) 3D profile of freestanding PdGr nanoribbons after CVD synthesis, showing relatively straight morphologies. (d) Typical Z-profile of a PdGr nanoribbon. (e) Typical loading-unloading curves of bare Pd and PdGr nanoribbons. The hysteresis between loading and unloading curves for Pd nanoribbon is from experimental artifact³⁰ and straightening of the slack nanoribbon during indentation. PdGr shows negligible hysteresis due to nanoribbon self-straightening after high temperature growth. (f) Cyclic loading curves on the same Pd nanoribbon. There is negligible variance in $P - h$ behavior after the first loading cycle.

Figure 5.8e presents the typical $P - h$ curves from nanoindentation measurements on a Pd nanoribbon and a PdGr nanoribbon. Deformation of the slack geometry causes a noticeable hysteresis in the first one or two cycles of loading and unloading curves for Pd, however, this is negligible for PdGr and PdC. This hysteresis can add additional uncertainty in displacement measurement and affect the fitting results. To minimize such measurement uncertainty, we applied cyclic loadings on Pd, as shown in Figure 5.8f. After the first loading cycle (the black line), the subsequent loading curves almost coincide which indicates that the slack nanoribbon aligns itself perpendicularly to the indenter edge and the nanoribbon deflection becomes normal.

The elastic properties of a freestanding pre-strained nanoribbon can be extracted from the $P - h$ behaviors using the reported indentation models.³⁰ However, in this study, the slack in the freestanding nanoribbon needs to be taken into consideration. We analyze the deformation of a freestanding slack Pd nanoribbon, as sketched in Figure 5.9a. The dark black line represents the Z-profiles of a Pd nanoribbon before CVD synthesis. The slack of the bare Pd nanoribbon is $h_0 = 0.8 \mu\text{m}$. The nanoribbon self-aligns to the load applied by a wedge indenter by straightening the slack geometry. Depending on the initial slack geometry, a Pd nanoribbon is subjected to flexural and tension deformation during straightening. The light gray line l_1 in Figure 5.9a illustrates how the nanoribbon becomes taut with a deflection h_1 , and from this point onward, stretching along the length direction dominates the nanoribbon load-deformation. As indentation proceeds, the nanoribbon deflects to h_2 , as shown in Figure 5.9a line l_2 . Previous studies have shown that, except for a very small range of initial deformation, the bending deformation does not affect the calculation of the elastic properties in microbridge testing and can be ignored for ultrathin film materials.^{28, 30} In this study, we focus on the nanoribbon's deflection from h_1 to h_2 with the

following assumptions: the bending moment can be ignored, nanoribbon is in tension and elastic during indentation, nanoribbon is well clamped on a rigid substrate without sliding. A new analysis is carried out to accurately extract the modulus from the nanoindentation load displacement of nanoribbon having slack, and more details are presented as follows:

The strain from h_1 to h_2 can be expressed as shown in Eq. 5.2:

$$\begin{aligned}\sin(\theta_2) &= \frac{2h_2}{l_2} = \frac{2h_2}{l_1 + \Delta l}; \\ \tan(\theta_2) &= \frac{2h_2}{l_0}; \\ \varepsilon_{1 \rightarrow 2} &= \frac{\Delta l}{l_1} = \frac{2h_2}{\sin(\theta_2)l_1} - 1\end{aligned}\tag{5.2}$$

The tension in nanoribbon at h_2 is:

$$N_2 = \frac{P_2}{2\sin(\theta_2)} = A(E\varepsilon_{1 \rightarrow 2} + \sigma_1); \text{ while } \sigma_1 \text{ is the stress installed in nanoribbon at } h_1.$$

And the applied load from wedge indenter:

$$P_2 = 2\sin(\theta_2)AE\varepsilon_{1 \rightarrow 2} + 2A\sigma_1\sin(\theta_2) = \frac{4AEh_2}{l_1} - 2AE\sin(\theta_2) + 2A\sigma_1\sin(\theta_2);$$

The Taylor series of $\sin(\theta_2)$ gives $\sin\left[\tan^{-1}\left(\frac{2h_2}{l_0}\right)\right] = \frac{2h_2}{l_0} - \frac{4h_2^3}{l_0^3}$,

$$P_2 = \left(\frac{8AE}{l_0^3} - \frac{8A\sigma_1}{l_0^3}\right)h_2^3 + \left(-\frac{4AE}{l_0} + \frac{4AE}{l_1} + \frac{4A\sigma_1}{l_0}\right)h_2\tag{5.3}$$

Notably, due to the slack, h_2 is greater than the real indentation-induced displacement of the Pd nanoribbon. In addition, there is a preload in nanoindentation for zero-deflection point detection. In this study, the preload is around $2\ \mu\text{N}$. h_2 can be expressed as the sum of the measured deflection data and slack height h_0 as well as the pre-deflection h_{pre} .

$$h_2 = h + h_0 + h_{\text{pre}} = h + h_1\tag{5.4}$$

$$P_2 = P + P_{\text{pre}};$$

$$P = \left(\frac{8AE}{l_0^3} - \frac{8A\sigma_1}{l_0^3} \right) h^3 + \left(\frac{24AEh_1}{l_0^3} - \frac{24A\sigma_1 h_1}{l_0^3} \right) h^2 + \left(\frac{24AEh_1^2}{l_0^3} - \frac{24A\sigma_1 h_1^2}{l_0^3} + \frac{4A\sigma_1}{l_0} - \frac{4AE}{l_0} + \frac{4AE}{l_1} \right) h + \frac{8AEh_1^3}{l_0^3} - \frac{8A\sigma_1 h_1^3}{l_0^3} - \frac{4AEh_1}{l_0} + \frac{4A\sigma_1 h_1}{l_0} + \frac{4AEh_1}{l_1} - P_{\text{pre}} \quad (5.5)$$

$$P = f_1 h^3 + f_2 h^2 + f_3 h + f_4 \quad (5.6)$$

Instead of the cubic-linear relation in the membrane model reported in previous studies,^{28, 30} here we use a full 3rd order polynomial function (Eq. 5.6) to analyze the P – h data. The elastic modulus of a slack Pd nanoribbon can be determined from least square fitting of the measured P – h curve using Eq. 5.7.

$$\Rightarrow h_1 = \frac{f_2}{3f_1} \text{ and } l_1 = 2\sqrt{\frac{l_0^2}{4} + h_1^2} = 2\sqrt{\frac{l_0^2}{4} + \left(\frac{f_2}{3f_1}\right)^2};$$

$$\Rightarrow \begin{cases} E = \frac{l_1}{4A} \left(f_3 - \frac{f_2^2}{3f_1} + \frac{f_1 l_0^3}{2} \right) \\ \sigma_1 = \frac{8AE - f_1 l_0^3}{8A} \end{cases} \quad (5.7)$$

As mentioned earlier, this previous analysis is relevant for the Pd nanoribbons without graphene. On the other hand, after graphene synthesis, the slack Pd nanoribbons can be stretched and even turn to be in uniaxial tension due to thermal expansion mismatch between Pd and the TEM substrate during high temperature CVD processes. Freestanding PdGr nanoribbon is straight before indentation, hence we can modify Eq. 5.4 as:

$$h_0 \rightarrow 0, h_1 = h_{\text{pre}}, N'_2 = \frac{P'_2}{2\sin(\theta_2)} = A(E\varepsilon_{0 \rightarrow 2} + \sigma_r);$$

$$P'_2 = \left(\frac{8AE}{l_0^3} - \frac{8A\sigma_r}{l_0^3} \right) h_2^3 + \frac{4A\sigma_r}{l_0} h_2 \quad (5.8)$$

Eq. 5.8 is similar to the reported membrane model.³⁰ Considering the preload for zero-deflection point, load-displacement relation can be rewritten as:

$$P' = \left(\frac{8AE}{l_0^3} - \frac{8A\sigma_r}{l_0^3} \right) h^3 + \left(\frac{24AEh_1}{l_0^3} - \frac{24A\sigma_r h_1}{l_0^3} \right) h^2 + \left(\frac{24AEh_1^2}{l_0^3} - \frac{24A\sigma_r h_1^2}{l_0^3} + \frac{4A\sigma_r}{l_0} \right) h + \frac{8AEh_1^3}{l_0^3} - \frac{8A\sigma_r h_1^3}{l_0^3} - \frac{4AEh_1}{l_0} + \frac{4A\sigma_r h_1}{l_0} - P_{\text{pre}} = f'_1 h^3 + f'_2 h^2 + f'_3 h + f'_4 \quad (5.9)$$

Eq. 5.9 also gives a fully polynomial function for nanoindentation data processing, while the elastic modulus of a pre-strained PdGr can be extracted using Eq. 5.10 as below:

$$\Rightarrow h_1 = h_{\text{pre}} = \frac{f_2}{3f_1};$$

$$\Rightarrow \begin{cases} E = \frac{f_1 l_0^3}{8A} + \frac{l_0}{4A} \left(f_3 - \frac{f_2^2}{3f_1} \right) \\ \sigma_r = \frac{l_0}{4A} \left(f_3 - \frac{f_2^2}{3f_1} \right) \end{cases} \quad (5.10)$$

The difference between Eq. 5.7 and Eq. 10, especially for the modulus is l_1 term. When h_0 is small, $l_1 \rightarrow l_0$ and two equations will lead to the same results.

The elastic modulus of the suspended nanoribbons can be determined by fitting the measured $P - h$ loading or unloading curves using Eq. 5.10. However, the proposed load-displacement mathematical models accurately fit the measured data only in the range where the assumptions of the model hold: the nanoribbon which was originally slack became taut due to the indentation load. We observe that the uncertainty in zero-displacement significantly affects the fitting results since a small displacement drift can lead to large uncertainty in the elastic modulus due to the cubic term in Eq. 5.3 and Eq. 5.5. For nanoindentation measurement on slack nanoribbons, we need to avoid the early stage in $P - h$ data ($h < h_1$) which corresponds to nanoribbon straightening deformation and fit the stretching dominated region which can be captured in the aforementioned analysis. Moreover, the nanoribbons can plastically deform at large strains in nanoindentation.¹⁷ Fitting the full range of $P - h$ data using the elastic deformation models could hence lead to errors. To solve

these limitations, a careful selection of the fitting range of raw $P - h$ data can be used to precisely determine the elastic modulus using the proposed indentation model, and this method is validated numerically.

Figure 5.9b illustrates the strategy to determine the elastic modulus of Pd thin films. The whole data is fitted using Eq 5.6 at various fitting ranges (FR) and varying starting points (SP), shown as the red dashed line in Figure 5.9b. Varying these two enables the determination of the taut configuration and extracts only the elastic modulus respectively. We calculate the root mean square error (RMSE) of the least square fitting to examine the goodness of curve fitting and use Eq. 5.7 to determine the elastic modulus for Pd. We first validate this fitting approach using finite element analysis (FEA) data. We model in COMSOL various nanoribbons having initial slack with different geometries and indent them to extract a numerical $P - h$ curve, then apply the fitting approach to this data (see Figure 5.10-5.12). Figure 5.9c displays the calculated moduli using the proposed numerical fitting method on the simulated $P - h$ data (Figure 5.11a) using Eq. 5.7 with varying SPs and FRs. Figure 5.9d shows that the mean value of the curve fitted modulus corresponds to the modulus used in the FEA simulations (103 GPa) with less than 4% error. To get more insights into the variations in fitted modulus, as shown in Figure 5.11b, for a specific fitting range, e.g. $FR = 1.3 \mu\text{m}$, too small SP leads to high RMSEs which indicate poor goodness of fitting due to the slack. On the other hand, when the SP is too large, the nanoribbon is under initial tensile stress at the assumed zero-point which is not taken into account correctly. Moreover, if the fitting range is too large, plastic behavior at the end of nanoindentation will affect the goodness of fit. As a result, the calculated moduli with small or large SP show unrealistic and inconsistent values from the given property (103 GPa) in FEA, as shown in Figure 5.9c. Notably,

there is a fitting range with the intermediate SPs and FRs yielding consistent modulus and the minimum RMSE. Converting Figure 5.9c into modulus histogram displayed in Figure 5.9d, we can determine the mean calculated modulus of 107.1 GPa, which has less than 4% error compared to the 103 GPa used as the input modulus in FEA. We have extensively validated the reliability of the proposed curve fitting method for the microbridge testing data analysis. COMSOL structural mechanics module³⁵ is used to generate the P – h behavior of a slack freestanding Pd strip when indented by a wedge indenter in the middle, as show in Figure 5.10a. According to the 3D profile measurements mentioned in the manuscript, we select a slackness $h_0 = 2 \mu\text{m}$, and strip width of $4 \mu\text{m}$ and length of $110 \mu\text{m}$, thickness of 150 nm . A line loading of $25 \mu\text{N}$ is applied to the middle of strip. The elastic modulus of Pd material is 103 GPa and the yield strength is 225 MPa. Figure S1 shows the Finite Element Analysis (FEA) models of freestanding Pd nanoribbons used in the validation of the indentation approach. Figure 5.10a represents the slack nanoribbons similar to the experiments, and Figure 5.10b is a more general case with a “S” shape. Both ribbons are indented in the middle with a line loading. Figure 5.11a displays the simulated P – h data for the strip with geometry shown in Figure 5.10a. Figure S2b shows the RMSE map in a SP and FR space. There is intermediate SPs and FRs leading to low RMSE values and a consistent modulus value. We obtain the mean modulus value of 107.1 GPa as shown in Figure 5.9c and 5.9d.

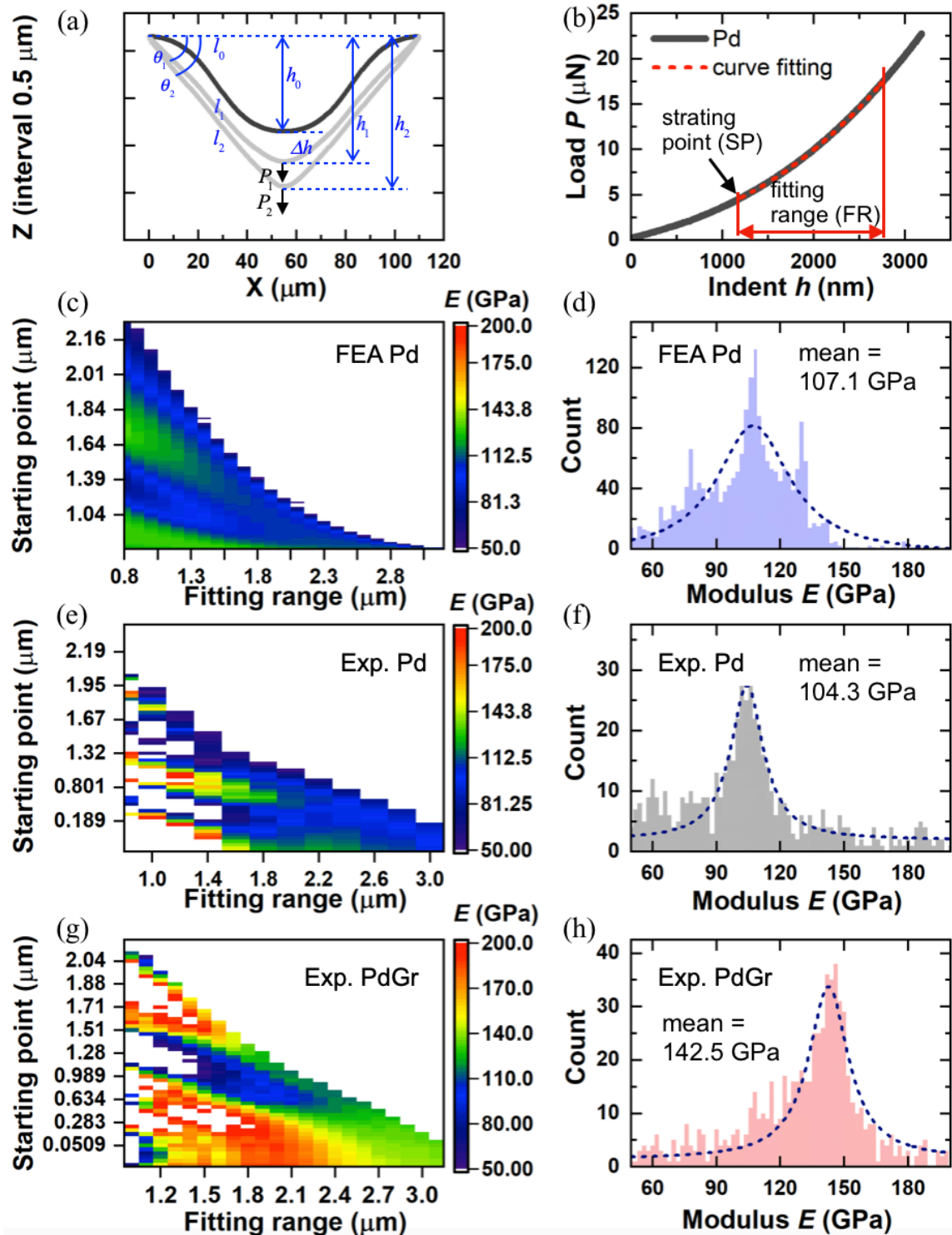


Figure 5.9. The elastic modulus measurement approach, numerical validation and experimental data. (a) Schematic of the straightening and stretching of a slack Pd nanoribbon. (b) Curve fitting of a typical $P-h$ data of a Pd nanoribbon, with a varying fitting range (FR) and starting point

Figure 5.9 (cont.)

(SP). (c) Validation of numerical fitting method using the simulated $P - h$ data from COMSOL.

The distribution of calculated elastic modulus E . (d) Histogram of calculated E in the range of 50-200 GPa, with a mean value of 107.1 GPa. (e) The distribution of calculated elastic modulus E of the experimentally measured $P - h$ data of a bare Pd nanoribbon. Pd thickness: 66 nm. (f)

Corresponding histogram of measured E to (e), with a mean value of 104.3 GPa. (g) The distribution of calculated elastic modulus E of PdGr nanoribbon. (h) Corresponding histogram of E to (g).

A more general slack geometry with “S” shape as shown in Figure 5.11b is also analyzed. Figure 5.12a shows the corresponding simulated $P - h$ data. Figure 5.12b shows the calculated E histogram with the mean value of 107.8 GPa. Notably, the slack geometry in this case needs longer time to be straightened (see Figure S5a and the inset z -profile evolution). The mean modulus matches well with the input property used in COMSOL simulation. These analyses suggest that the fitting method adopted can properly extract the elastic modulus of the ultrathin Pd films.

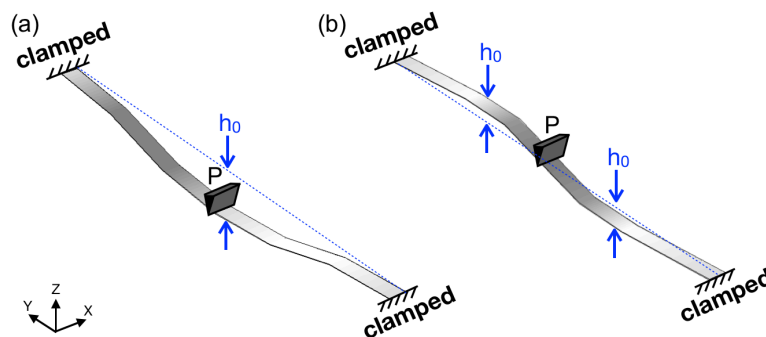


Figure 5.10. (a) A COMSOL simulation model of a freestanding thin Pd nanoribbon with a slackness of h_0 and doubly clamped ends. A line load (P) is applied to the middle of the nanoribbon. (b) A COMSOL model of a “S” shape slack Pd nanoribbon.

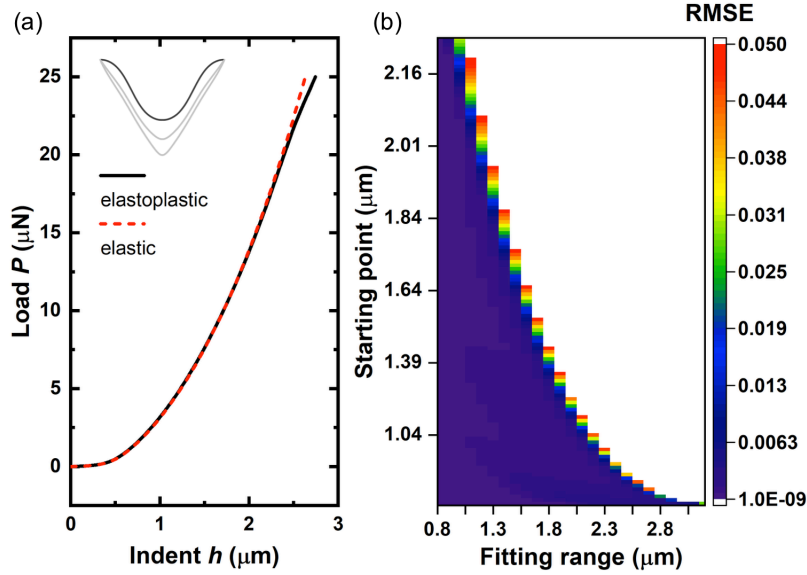


Figure 5.11. Validation of numerical fitting method-1. (a) Simulated $P - h$ behavior of a slack Pd nanoribbon. COMSOL solid mechanics interface is used in order to represent the elastoplastic behaviors (the black line) of ultrathin metal ribbons during microbridge testing. This plastic deformation in freestanding nanoribbons cannot be captured using the elastic models (the red dash line) at large indent region. Inset: evolution of Pd ribbon from slack to stretching state. (b) Distribution of curve fitting RMSE with varying SP and FR.

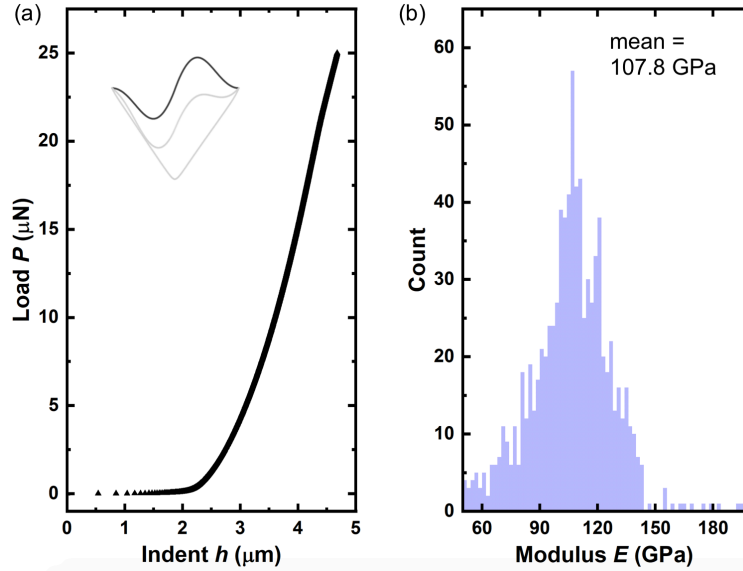


Figure 5.12. Validation of numerical fitting method-2. (a) Simulated $P - h$ behavior of a slack Pd nanoribbon with a “S” shape. (b) Histogram of calculated elastic modulus. The mean value is 104.8 GPa, which is very close to the input property (103 GPa) in FEA simulation.

This approach is used to measure the moduli of Pd and PdGr nanoribbons from indentation of suspended microbridges such as the ones shown in Figures 5.7 and 5.8. Figure 5.9e and 5.9f display the curve fitting results with the measured $P - h$ data of a slack Pd nanoribbon in the microbridge testing. The means values and the data distributions are shown in Figure 5.9f and 5.9h, and the moduli of Pd and PdGr are found to be 104.3 GPa (66 nm thick) and 142.5 GPa (71 nm thick) respectively. Similarly, we gain more insights by inspecting the roles of SP and FR on the measured mean modulus. Figure 5.9e and 5.9g show the existence of a fitting range in which the calculated elastic modulus is stable relative to variations in SP or FR, while also maintaining low RMSE (Figure 5.13a). A small SP or FR, e.g. FR = 1.8 μm , leads to high RMSE and fluctuating modulus, which indicates poor goodness of fitting due to the geometry of slack and deformation in Pd nanoribbon at the beginning of nanoindentation. While a large SP or FR, e.g. FR = 2.2 μm ,

gives the decaying modulus as SP increases due to plasticity effects taking place at large deflections. Notably, there is a plateau in E that is independent of SP and FR and reflects the real elastic property of the nanoribbon, see the zoomed-in inset in Figure 5.13b. This plateau in E coincides with the mean modulus value of 104.3 GPa shown in Figure 5.9f. For the $P - h$ region where the elastic theoretical model applies, consistent E and low RMSE are expected. Figure 5.13c presents the correlation of calculated E and RMSE.

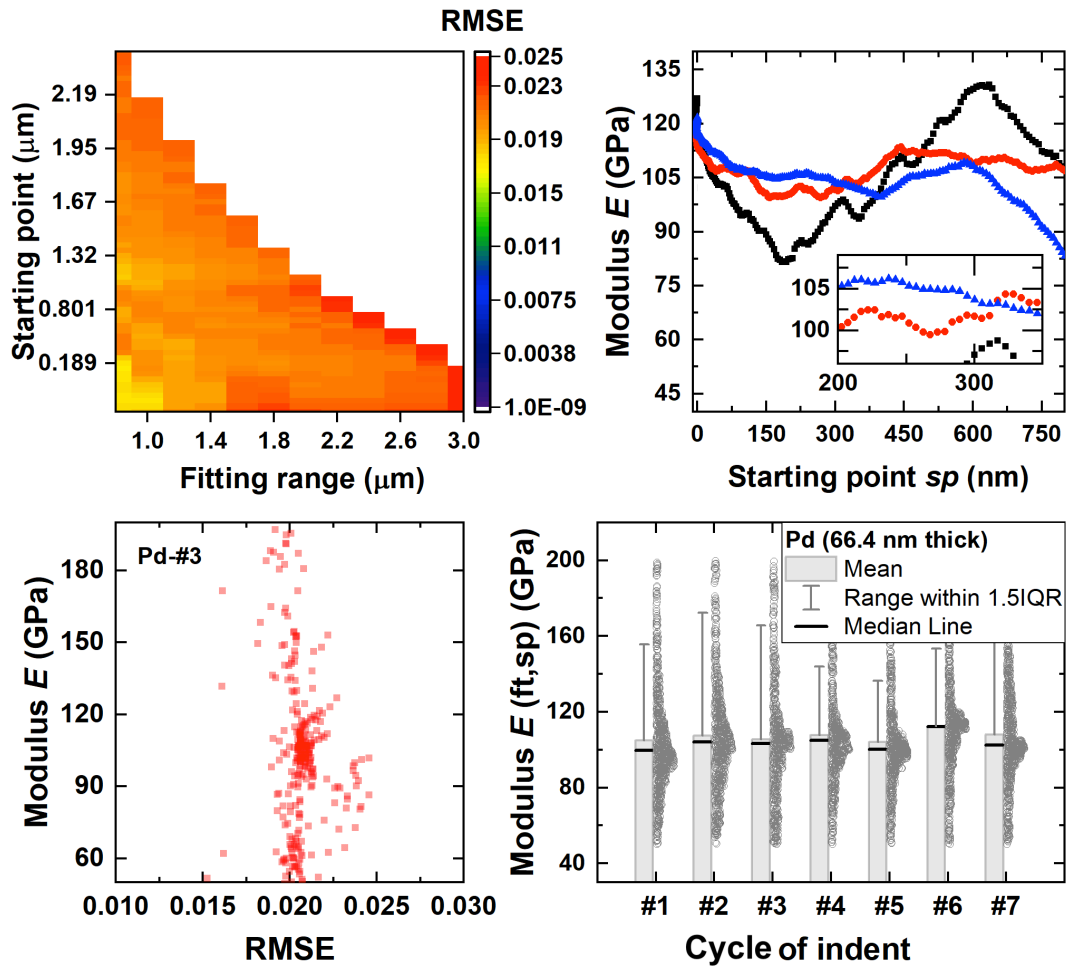


Figure 5.13. Example of indentation data processing of bare Pd nanoribbons. Pd thickness: 66 nm. (a) RMSE map with varying SP and FR. (b) Typical dependence of calculated modulus on SP, with selected FRs. (c) Correlation of calculation modulus E and RMSE. Starting with the

Figure 5.13 (cont.)

lowest RMSE, E starts to stabilize at around $\text{RMSE} = 0.02$ with $E \approx 104$ GPa. This agrees with the fitting results in the main manuscript. (d) Distribution of calculated modulus for cyclic indentations, showing $E = 103.2 \pm 1.1$ GPa.

Similar to fitting analysis for bare Pd strips, we can extract the elastic modulus of an as-grown PdGr strip, see Figure 5.14. Notably, since the strips are stretched and the slackness is reduced during graphene synthesis processes, there is more consistent data with small SPs.

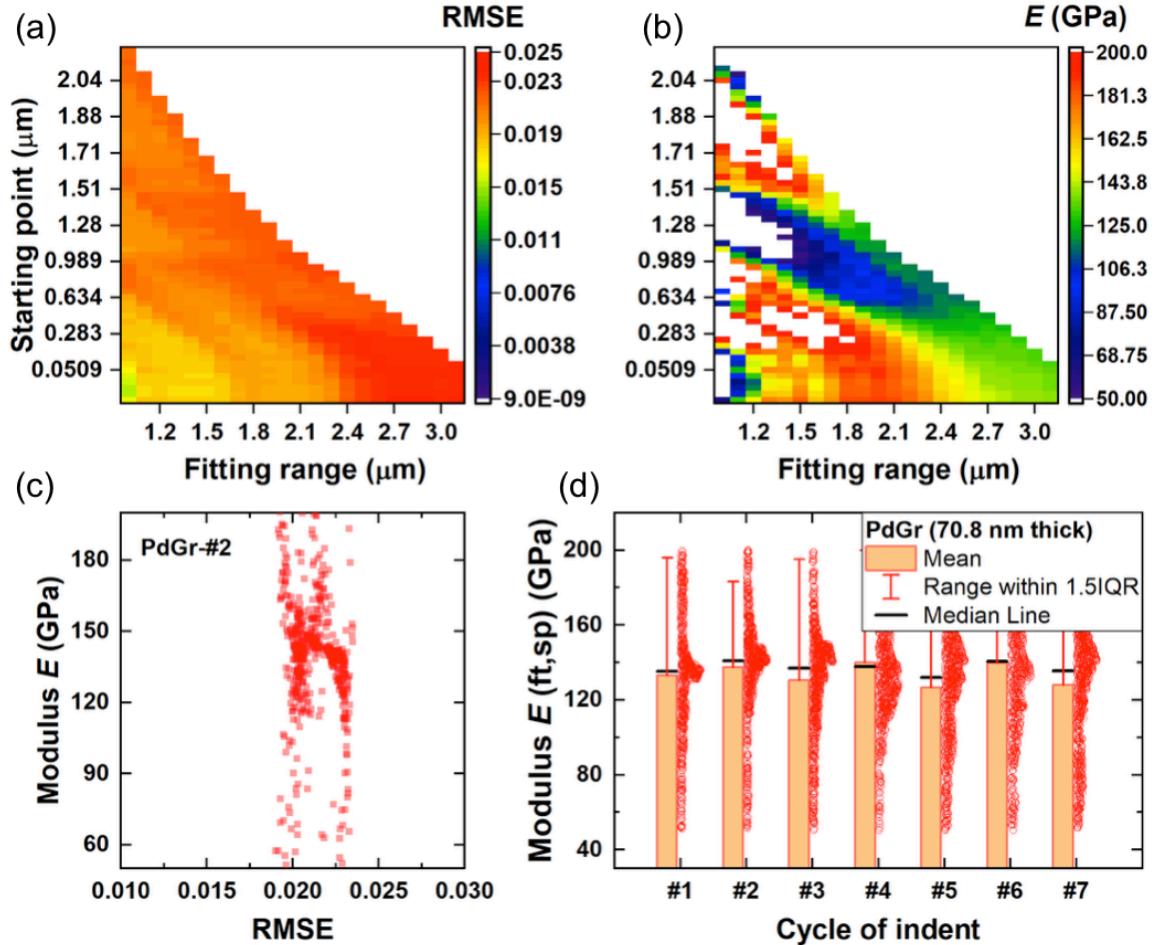


Figure 5.14. Microbridge testing data processing of the grown PdGr nanoribbons. PdGr thickness: 71 nm. (a) RMSE map with varying SP and FR. (b) Distribution of calculated

Figure 5.14 (cont.)

modulus associated to (a). Results are presented in the range of 50 to 200 GPa. (c) Correlation of calculation modulus E and RMSE. Starting with the lowest RMSE, E starts to stabilize at around $\text{RMSE} = 0.02$ with $E \approx 142$ GPa. This also agrees with the fitting results in the main manuscript.

(d) Distribution of calculated modulus for cyclic indentations, showing $E_{\text{PdGr}} = 140.1 \pm 1.1$ GPa.

The indentation of graphene-coated Pd (PdGr) shows a significant increase in the measured modulus compared to Pd. Figure 5.9g and 5.9h display the E distribution in the fitting space and the corresponding E histogram for one indentation data for a PdGr nanoribbon. Figure 5.14 also displays the corresponding RMSE and E distributions for cyclic loading, from which we can determine the mean E_{PdGr} value at 142.5 ± 1.1 GPa for a 71 nm thick PdGr film. Notably, there is over 35 % increase of E in the Pd nanoribbon due to bilayer graphene ($\sim v_{\text{Gr}} = 0.92$ vol %) on the surface. Graphene is expected to have strong interfacial adhesion on Pd so we assume that there is no interfacial slip within the elastic regime.⁴¹ The results can also be affected by changes in the Pd during synthesis¹⁴ where carbon diffuses into interstitial sites and could alter the elastic properties of the nanoribbon. We hence isolate the graphene reinforcement effect by removing the graphene layers from the same PdGr sample with RIE and testing the nanoribbon (also named as PdC to indicate that the Pd contains carbon). The elastic modulus of a 71 nm thick PdC film is measured by indentation and is found to be 119.8 ± 1.4 GPa. This confirms that the significant increase in PdGr can be partially attributed to the changes during CVD leading to the transformation of Pd into PdC. This approach allows us to precisely study the contribution of as-

grown bilayer graphene to the composite elasticity while examining the role interfacial mechanics on the elastic behavior of the nanoribbons.

It is known that Pd strongly interacts with graphene as also manifested by the small separation between the Pd and C atoms (0.23 - 0.25 nm on Pd (111) surface), a value smaller than the interlayer separation in graphite and smaller than the separation between graphene and other transition metals.^{41, 42} The interfacial mechanics is governed by in-plane strain mismatch between graphene and Pd (111) for instance is $\sim 3.3\%$ in compression.³⁹ The sputtered Pd thin films after annealing are predominantly (111), see electron backscattering diffraction (EBSD) analyses in Figure 5.15. Moreover, due to mismatch between the thermal expansion coefficients of graphene and the seed metal, graphene is usually in strain after synthesis.

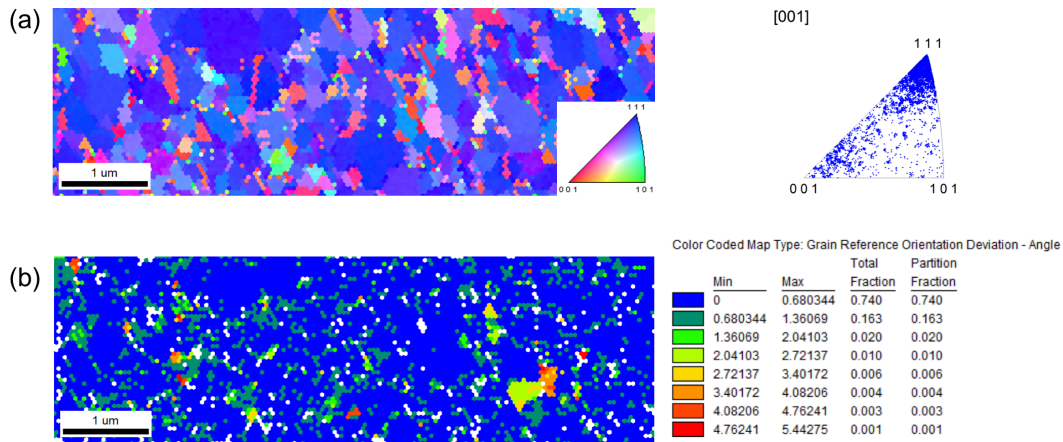


Figure 5.15. EBSD maps of a freestanding Pd nanoribbon. (a) Inverse pole figure (IPF) shows polycrystalline structure in Pd nanoribbons. The average grain size is 158 nm. Notably, there is considerable number of grains with small misorientation angles to Pd (111). (b) Grain reference orientation deviation (GROD) shows the small orientation deviation to the average for the grain.

5.3.4. *Effect of mismatch interfacial stress on the elastic modulus of PdGr thin film composites*

The interfacial strain in as-grown PdGr nanoribbons can be characterized using Raman spectroscopy because it affects the orbital hybridization of the carbon atoms hence it shifts the G and 2D peak frequencies. Figure 5.16a shows the Raman spectroscopy of PdGr nanoribbons clamped on a TEM grid and used for indentation. We observe two types of Raman spectra. Firstly, on the clamped region where the PdGr is supported on SiO₂/Si TEM grid, Raman spectroscopy shows single sharp G peak at $\sim 1606.3 \text{ cm}^{-1}$ and 2D peak at $\sim 2695.4 \text{ cm}^{-1}$. Whereas, there is an obvious red shift in G mode frequency to $\sim 1551.6 \text{ cm}^{-1}$ for the freestanding region on the same Pd nanoribbon. It is known that this Raman shift is due to not only the strain in graphene but also the doping effect from metallic substrates.^{43, 44} We can extract the strain effect in graphene by isolating the Pd substrate effect from Raman frequencies correlation, as shown in Figure 5.16b. There is an offset in the correlation of Raman $\omega_G - \omega_{2D}$ frequencies between the pristine graphene (with no strain no doping) and as-grown graphene on the Pd substrate. It has been investigated that graphene supported on strongly interacting substrates, e.g. Ni and Pd,^{41, 42} can be doped and show blue shifts in Raman frequencies compared to the pristine graphene.⁴⁴ The purple line in Figure 5.16b represents the $\omega_G - \omega_{2D}$ correlation of graphene with different doping levels but in the same strain state. As a result, graphene grown on the supported Pd area is slightly compressed. This can be attributed to the lattice mismatch strain (ϵ_{mis}) between graphene and Pd, as well as the polycrystalline substrate texture.²¹ Notably, there is obvious red shift in $\omega_G - \omega_{2D}$ correlation of graphene grown on the freestanding region of a PdGr nanoribbon, indicating that graphene is stretched in these region.⁴³ The apparent slope in Figure 5.16b is the strain slope, where the data points at the bottom left corner are under the largest tensile mismatch strains. This agrees with the straightening of the nanoribbons and the associated decrease in slack observed in the 3D profile

measurements. The exact absolute value of the strain cannot be precisely determined from these measurements since it requires calibration to the Raman spectrum of graphene sitting epitaxially on Pd but without any mismatch strain. We use the results of Figure 5.16 to qualitatively demonstrate the tensile strains in the graphene in the suspended nanoribbons.

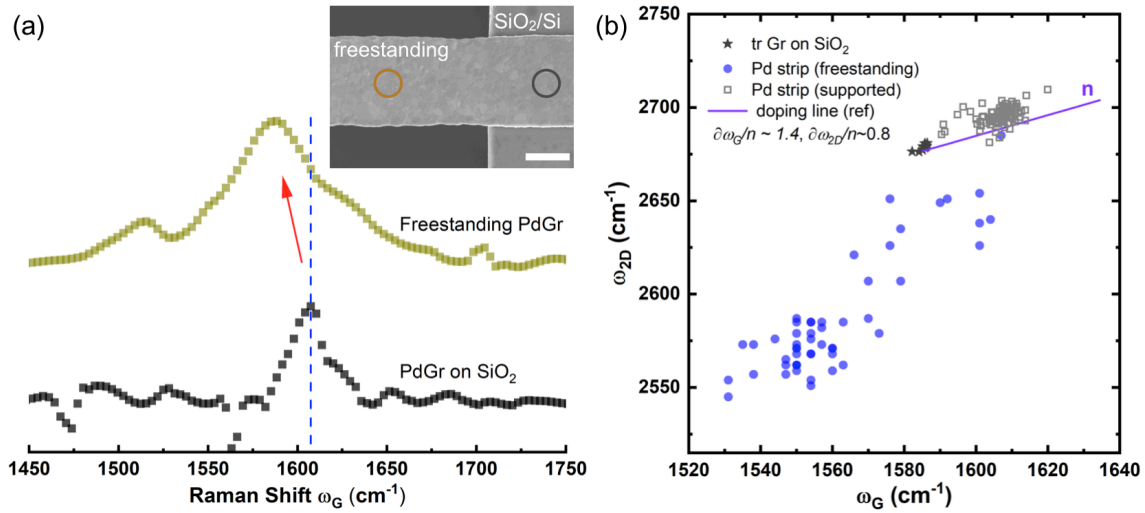


Figure 5.16. Raman spectroscopy in a freestanding PdGr thin film. (a) Raman spectra of freestanding PdGr nanoribbon and clamped PdGr on SiO₂. The G peak in freestanding region is subjected to red shift with respect to that in supported region, representing the tension in graphene on freestanding Pd. Inset SEM image shows the corresponding freestanding and supported region on a PdGr nanoribbon. Scale bar: 2 μm. (b) Correlation of frequencies of G and 2D Raman modes in freestanding PdGr and supported PdGr nanoribbons. Frequency data is collected from Raman maps taken with laser excitation wavelength of 532 nm and exposure time of 15 s. The unstrained and undoped Gr (transferred onto a SiO₂/Si substrate) has the average $\overline{\omega_G}$ at 1607 cm⁻¹ and $\overline{\omega_{2D}}$ at 2696 cm⁻¹. The blue doping line is extracted from reference, assuming

$$\left. \frac{\partial \omega_{2D}}{\partial \omega_G} \right|_{h^+} = 0.55.^{44}$$

Using these insights, we analyze the contributions of the graphene and the interfacial mismatch strains on the measured moduli of PdGr. The tension per unit width in the deflected nanoribbons is

$$N = E_{\text{PdC}} t_{\text{PdC}} (\varepsilon - \varepsilon_{\text{mis}}) + 2nE_{\text{Gr}}^{2\text{D}} (\varepsilon_{\text{mis}} + \varepsilon) + 2nD_{\text{Gr}}^{2\text{D}} (\varepsilon_{\text{mis}} + \varepsilon)^2 + \sigma_{\text{r}}; \quad (5.11)$$

where N is the tensile force per unit width during indentation, t_{PdC} is the nanoribbon thickness, n is the number of graphene layers (for example $n=2$ for bilayer graphene), ε is the uniaxial tensile strain in PdGr composite nanoribbon during nanoindentation, σ_{r} is the residual stress in the nanoribbon due to stretching over the trench during growth, and the factor 2 in Eq. 5.11 accounts for the top and bottom surfaces of the nanoribbon. Here, we ignore the thickness of graphene layer and introduce the 2D elastic constants $E_{\text{Gr}}^{2\text{D}} = 340 \text{ N m}^{-1}$. Since molecular dynamic simulations and experiments suggest that graphene shows quadratic dependence on strain,^{26, 45} we consider the nonlinear elastic behavior of as-grown graphene layer on Pd nanoribbons with a third-order elastic constant $D_{\text{Gr}}^{2\text{D}} = -690 \text{ N m}^{-1}$. The nonlinear elastic constitutive behavior of graphene can be expressed as $\sigma_{\text{Gr}} = E_{\text{Gr}}^{2\text{D}} \varepsilon + D_{\text{Gr}}^{2\text{D}} \varepsilon^2$.²⁶ We define the volume fraction $v \equiv \frac{t_{\text{PdC}}}{t}$. Straining of the Pd surface by graphene synthesis could introduce the surface stress, which can contribute to the measured modulus when the nanoribbon is strained due to the quadratic term.

In this study, we use very small nanoindentation strains so that $\varepsilon \ll \varepsilon_{\text{mis}}$. As a result, we can expand Eq. 5.11 and ignore the resulting ε^2 term, giving:

$$N = \sigma_{\text{r}} + 2nE_{\text{Gr}}^{2\text{D}} \varepsilon_{\text{mis}} + 2nD_{\text{Gr}}^{2\text{D}} \varepsilon_{\text{mis}}^2 - E_{\text{PdC}} t_{\text{PdC}} \varepsilon_{\text{mis}} + \left(E_{\text{PdC}} v + \frac{2nE_{\text{Gr}}^{2\text{D}} + 4nD_{\text{Gr}}^{2\text{D}} \varepsilon_{\text{mis}}}{t} \right) t \varepsilon; \quad (5.12)$$

where the interfacial strain due to growth cancels out $2nE_{\text{Gr}}^{2\text{D}} \varepsilon_{\text{mis}} + 2nD_{\text{Gr}}^{2\text{D}} \varepsilon_{\text{mis}}^2 - E_{\text{PdC}} t_{\text{PdC}} \varepsilon_{\text{mis}} = 0$. The term in the bracket of Eq. (5.12) $E_{\text{PdC}} v + \frac{2nE_{\text{Gr}}^{2\text{D}} + 4nD_{\text{Gr}}^{2\text{D}} \varepsilon_{\text{mis}}}{t}$ is then equivalent to the

measured elastic modulus of PdGr composite nanoribbon as it depends on the applied indentation strain ε . Therefore,

$$E_{\text{PdC}}\nu + \frac{2nE_{\text{Gr}}^{2\text{D}} + 4nD_{\text{Gr}}^{2\text{D}}\varepsilon_{\text{mis}}}{t} = E_{\text{PdGr}};$$

$$\Rightarrow E_{\text{PdGr}} - \nu E_{\text{PdC}} = \frac{2nE_{\text{Gr}}^{2\text{D}} + 4nD_{\text{Gr}}^{2\text{D}}\varepsilon_{\text{mis}}}{t}, \quad (5.13)$$

A couple of crucial insights can be drawn from this analysis: (i) the quadratic modulus of graphene leads to the dependence of the measured modulus on the mismatch strain ε_{mis} ; and (ii) the term $E_{\text{PdGr}} - \nu E_{\text{PdC}}$ can be directly measured and used to analyze the relative contributions of the graphene modulus $2nE_{\text{Gr}}^{2\text{D}}$ and the mismatch strain $4nD_{\text{Gr}}^{2\text{D}}\varepsilon_{\text{mis}}$ on the nanoribbon elastic response. Figure 5.17a shows the measured moduli of Pd, PdGr and PdC with different film thicknesses. Indeed, experimentally, the elastic modulus of bare Pd does not vary within the thickness range from 36 to 300 nm in this study. On the other hand, as discussed before, the elastic modulus of PdGr thin films significantly increase after the synthesis of graphene, and this increase is scale dependent. More specifically, the PdGr modulus increases notably as film thickness reduces. This not only stems from the contribution of high in-plane stiffness of graphene in PdGr composite, but is also affected by the graphene nonlinear elastic term $D_{\text{Gr}}^{2\text{D}}$ and the large Pd-graphene residual interfacial stress. Notably, after etching the graphene layer away, we also release the interfacial elastic energy installed between graphene and Pd. This confirms the nontrivial contribution of the Pd-graphene interfacial stress on the elastic property in PdGr composites.

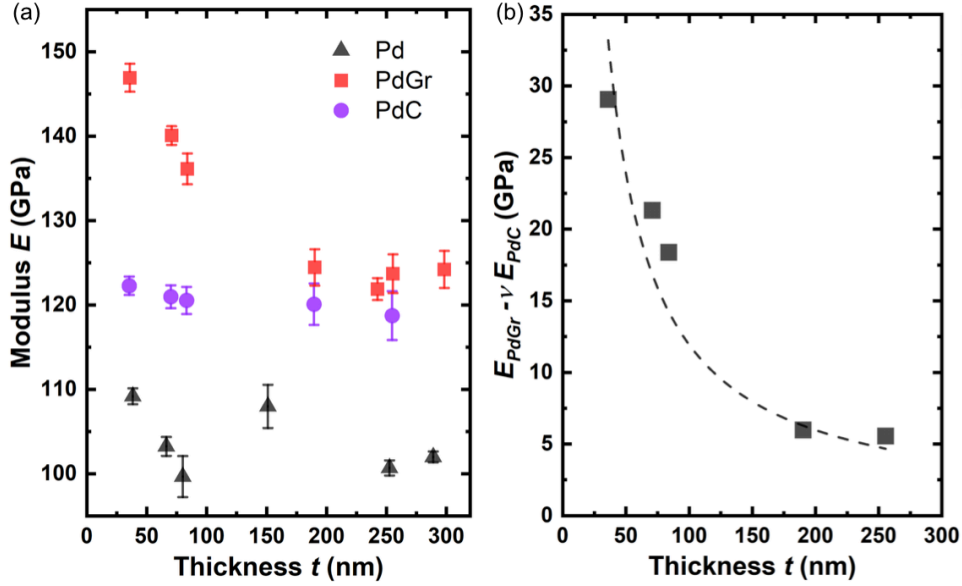


Figure 5.17. Increase in elastic modulus of graphene-coated Pd. (a) Dependence of the elastic moduli of bare Pd, PdGr and PdC on thin film thickness. (b) Dependence of $E_{PdGr} - vE_{PdC}$ on thin film thickness. Dashed line represents the fitted curve in the form of $1251.1/t$.

Figure 5.17b plots the Eq. 13 with the measured E_{PdGr} and E_{PdC} . By the least square fitting, $2nE_{Gr}^{2D} + 4nD_{Gr}^{2D}\epsilon_{mis} \approx 1251.1 \text{ J m}^{-2}$. Using the values from ^{26, 45} and $n=2$ for bilayer graphene, we find a mismatch strain $\epsilon_{mis}=1.97\%$ (tensile). This suggests that graphene-induced surface strain can significantly modify thin film materials' elastic modulus. More generally, it shows that graphene is an effective reinforcement in Pd up to volume fraction of $\sim 0.3\%$.

Next, we analyze the mechanism of increase of the PdC modulus (E_{PdC}) by 14.8 % compared to that of Pd (E_{Pd}) even when the graphene is removed by etching. Besides the expected interstitial carbon reinforcement effect, we also investigated the formation of palladium carbide-like phase close to the Pd surface after graphene growth. Figure 5.18a and Figure 5.19 shows a cross sectional transmission electron microscopy (TEM) image of a PdGr thin film which shows the graphene

layers as well as the fringes associated with the atomic spacings of the Pd. We measured the Pd lattice fringes near the Pd-graphene interface and noted that they are expanded to about 7.2 % in comparison with Pd bulk values. This expansion can be related to carbon incorporation into the Pd lattice especially in the sub-surface sites.⁴⁶ Importantly, carbon atoms in this carbon-rich layer close to the Pd surface have preferred interstitial sites and can form a carbide like Pd-C phase.⁴⁷⁻⁴⁹ The formation process of this Pd-C phase is unclear, nevertheless, there is a number of theoretically reported stable Pd-C phases exhibiting very high stiffness and hardness.⁵⁰ In light of these considerations, it is reasonable to propose a model with Pd/Pd-C/Gr laminated structure for the grown PdGr composite thin film, as shown in Figure 5.18b. In order to confirm the existence of Pd-C layer in Pd subsurface, X-ray photoelectron spectroscopy (XPS) is used to track the core level shift in Pd peaks. XPS measurements are made using a Kratos Axis Ultra X-ray photoelectron spectrometer using monochromatic Al K α radiation (1486.6 eV). The X-ray detection depth is about 10 nm. The binding energies are referenced to the graphitic C 1s signal at 284.4 eV. We tilt the PdGr surface so that more subsurface signal could be collected. Figure 5.18c and 5.18d present the Pd 3d and C 1s XP spectra of as-grown PdGr thin film. As expected, the carbonaceous species shift the binding energy (BE) of surface Pd atoms to the high BE side of the bulk Pd signal (core level of Pd 3d_{5/2} ~ 335.1 eV). The BE for this carbon-rich species is found at about 335.7 eV, which is 0.6-0.8 eV shifted from Pd 3d core level. This agrees well with the experimental and calculated results for the sub-Pd surface Pd-C phase.^{47, 48} In Figure 5.18d, the C 1s peak at BE = 284.4 eV is assigned to graphene related peaks. The peak asymmetry toward lower BE with a low intensity peak at ~283.7 eV is a signature of the presence of carbide, which can be related to Pd-C bonds.

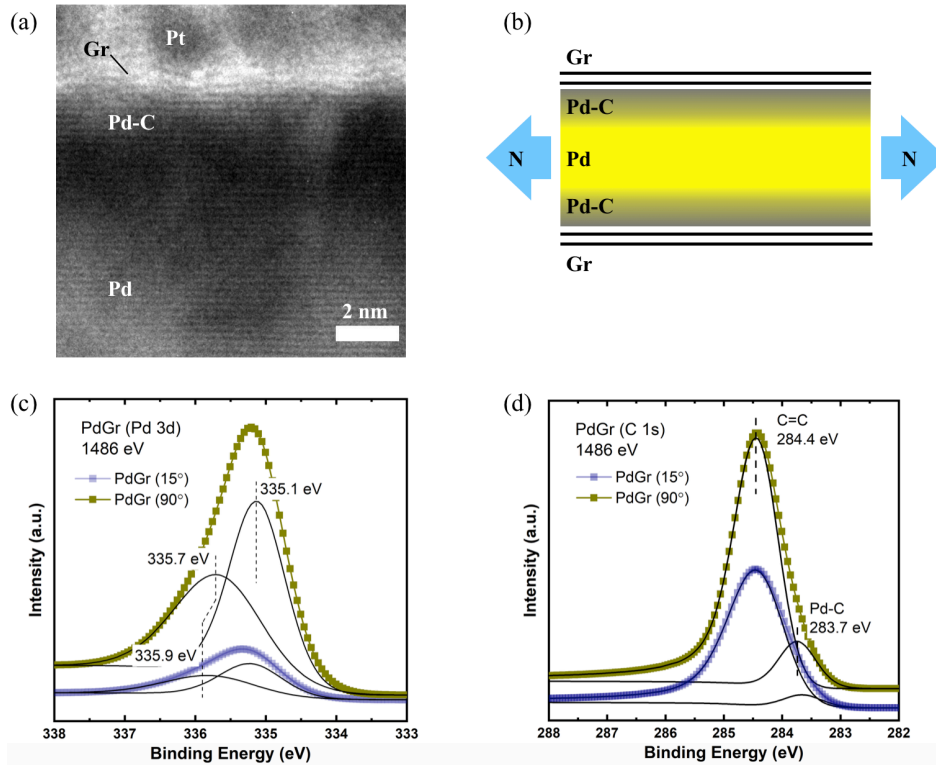


Figure 5.18. Formation of palladium carbide at the Pd-graphene interface during CVD synthesis. (a) TEM image shows the cross section of a PdGr nanoribbon. Pd lattice expands close to the Pd-graphene interface. Scale bar: 2 nm. (b) Schematic of Pd-PdC-Gr laminated composite structure in PdGr thin films. Notably, strong interfacial stress between Pd-graphene layers contribute to the elastic properties of PdGr nanocomposites. (c) Pd $3d_{5/2}$ XP spectra for the grown PdGr thin film using 1486 eV excitation energy. The Pd component at 335.1 eV corresponds to bulk, metallic Pd, whereas the higher binding-energy peak (335.7 eV) represents the core-level shift components including palladium carbide. By tilting the sample to the angle w.r.t beam, the Pd surface properties can be amplified. With 15° tilting angle, higher binding-energy peak (335.9 eV) associated to PdC is observed. (d) C 1s XP spectrum for the grown PdGr thin film. A sharp peak at 284.4 eV confirms the sp^2 hybridized carbon (graphene), while a tiny lower binding-energy indicates the existence of carbide.

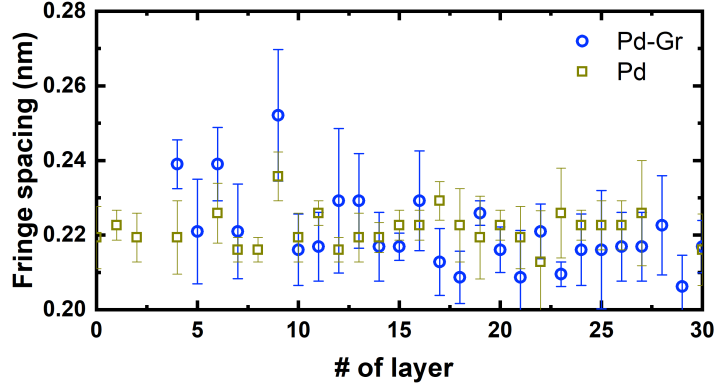


Figure 5.19. Comparison of the TEM fringe spacing of Figure 5.18a near the surfaces of a bare Pd and a PdGr composite nanoribbon. The PdGr lattice expands near thin film surface.

With the presence of the carbide phase near the Pd-graphene interface, we can separate the elastic modulus of PdC into the carbide boundary layer modulus E_S and the pure Pd modulus E_{Pd} with the rule of mixture as $E_{PdC} = E_S v_S + E_{Pd}(1 - v_S)$, where the surface layer thickness is t_S and the volume fraction $v_S \equiv \frac{t_S}{t_{PdC}}$. The thickness of t_S can be estimated from the fringe spacings in the TEM of Figure 5.7. For example, for PdGr-4, $t_S \approx 3.7$ nm and $t_{PdC} = 189$ nm, with the measured $E_{PdC} = 116.8 \pm 2.5$ GPa. Using the measured value of $E_{Pd} = 108.0 \pm 2.6$ GPa, we can estimate the modulus for carbide phase about $E_S = 332.8$ GPa, which is in the range of the reported theoretical results, see Table 5.2.⁵⁰ It is possible that multiple types of stable carbide phases coexist in PdGr thin film. However, this simple analysis leverages the imaging and XPS to rationalize the measured increase in modulus of the nanoribbons even when the graphene layer is etched.

Table 5.2. Theoretical predictions of the elastic constant (C_{11}) of Pd carbides⁵⁰

Pd carbide	E (GPa)
Rocksalt	236.0-411.5

Table 5.2 (cont.)

Zinc blende	171.8
Cesium chloride	260.0
Tungsten carbide	356.0
Nickel arsenide	400.0

5.4. Conclusions

In summary, several indentation modalities have been used to characterize the mechanical behavior of Pd thin films coated by graphene. A useful microbridge nanoindentation method is developed to precisely determine freestanding ultrathin films mechanical properties. The elastic behaviors of Pd thin films and the CVD-grown PdGr thin film composites are compared. 2-3-layer CVD-grown graphene significantly increase the thin metal films' elastic, for example, ~35 % for 66 nm thick Pd. This enhancement not only stems from the high stiffness in graphene layer, but is also attributed to the strong Pd-graphene interfacial stress via CVD synthesis. With high surface straining from graphene growth, PdGr thin film exhibit obvious thickness dependent modulus, which is usually only prominent in atomic scale metal slabs. In addition, a very stiff Pd-C phase is observed near Pd surface after graphene growth. With the help from graphene, Pd-C and Pd-graphene interfacial stress, dislocations are pinned and pile up at the PdGr surface introducing more strain hardening in PdGr than the bare metal. Interestingly, PdGr also exhibits more ductility than Pd. This study suggests a new route to enhance thin film materials' mechanical properties that can be applied in numbers of micro/nano scale functional devices.

5.5. References:

1. Rogers, J. A.; Someya, T.; Huang, Y. *Science* **2010**, 327, (5973), 1603-1607.
2. Jang, K. I.; Chung, H. U.; Xu, S.; Lee, C. H.; Luan, H.; Jeong, J.; Cheng, H.; Kim, G. T.; Han, S. Y.; Lee, J. W.; Kim, J.; Cho, M.; Miao, F.; Yang, Y.; Jung, H. N.; Flavin, M.; Liu, H.; Kong, G. W.; Yu, K. J.; Rhee, S. I.; Chung, J.; Kim, B.; Kwak, J. W.; Yun, M. H.; Kim, J. Y.; Song, Y. M.; Paik, U.; Zhang, Y.; Huang, Y.; Rogers, J. A. *Nat Commun* **2015**, 6, 6566.
3. Zhang, Y.; Wang, S.; Li, X.; Fan, J. A.; Xu, S.; Song, Y. M.; Choi, K.-J.; Yeo, W.-H.; Lee, W.; Nazaar, S. N.; Lu, B.; Yin, L.; Hwang, K.-C.; Rogers, J. A.; Huang, Y. *Advanced Functional Materials* **2014**, 24, (14), 2028-2037.
4. Wang, L.; Zeng, Z.; Gao, W.; Maxson, T.; Raciti, D.; Giroux, M.; Pan, X.; Wang, C.; Greeley, J. **2019**, 363, (6429), 870-874.
5. Wong, E. W.; Sheehan, P. E.; Lieber, C. M. *Science* **1997**, 277, (5334), 1971-1975.
6. Poncharal, P.; Wang, Z. L.; Ugarte, D.; de Heer, W. A. *Science* **1999**, 283, (5407), 1513-1516.
7. Cuenot, S.; Frétigny, C.; Demoustier-Champagne, S.; Nysten, B. *Physical Review B* **2004**, 69, (16), 165410.
8. Banerjee, A.; Bernoulli, D.; Zhang, H.; Yuen, M.-F.; Liu, J.; Dong, J.; Ding, F.; Lu, J.; Dao, M.; Zhang, W.; Lu, Y.; Suresh, S. *Science* **2018**, 360, (6386), 300-302.
9. Miller, R. E.; Shenoy, V. B. *Nanotechnology* **2000**, 11, (3), 139-147.
10. Fedorchenko, A. I.; Wang, A.-B.; Cheng, H. H. *Applied Physics Letters* **2009**, 94, (15), 152111.
11. Cammarata, R. C. *Progress in Surface Science* **1994**, 46, (1), 1-38.
12. Tran, R.; Xu, Z.; Radhakrishnan, B.; Winston, D.; Sun, W.; Persson, K. A.; Ong, S. P. *Scientific Data* **2016**, 3, 160080.
13. Tyson, W. R.; Miller, W. A. *Surface Science* **1977**, 62, (1), 267-276.
14. Zhang, K.; Androulidakis, C.; Chen, M.; Tawfick, S. *Advanced Functional Materials* **2018**, 28, (48), 1804068.
15. Kim, Y.; Lee, J.; Yeom, M. S.; Shin, J. W.; Kim, H.; Cui, Y.; Kysar, J. W.; Hone, J.; Jung, Y.; Jeon, S.; Han, S. M. *Nat Commun* **2013**, 4, 2114.
16. Hwang, B.; Kim, W.; Kim, J.; Lee, S.; Lim, S.; Kim, S.; Oh, S. H.; Ryu, S.; Han, S. M. *Nano Lett* **2017**, 17, (8), 4740-4745.
17. Zhang, K.; Poss, M.; Chen, P.-J.; Tawfick, S. *Advanced Engineering Materials* **2017**, 19, (12), 1700475.
18. He, R.; Zhao, L.; Petrone, N.; Kim, K. S.; Roth, M.; Hone, J.; Kim, P.; Pasupathy, A.; Pinczuk, A. *Nano Letters* **2012**, 12, (5), 2408-2413.
19. Bronsgeest, M. S.; Bendiab, N.; Mathur, S.; Kimouche, A.; Johnson, H. T.; Coraux, J.; Pochet, P. *Nano Letters* **2015**, 15, (8), 5098-5104.
20. Kang, J. H.; Moon, J.; Kim, D. J.; Kim, Y.; Jo, I.; Jeon, C.; Lee, J.; Hong, B. H. *Nano Letters* **2016**, 16, (10), 5993-5998.
21. Li, B.-W.; Luo, D.; Zhu, L.; Zhang, X.; Jin, S.; Huang, M.; Ding, F.; Ruoff, R. S. *Advanced Materials* **2018**, 30, (10), 1706504.
22. Huang, H.; Spaepen, F. *Acta Materialia* **2000**, 48, (12), 3261-3269.
23. Gianola, D. S.; Eberl, C. *JOM* **2009**, 61, (3), 24.

24. Saha, R.; Nix, W. D. *Acta Materialia* **2002**, 50, (1), 23-38.
25. Lu, N.; Wang, X.; Suo, Z.; Vlassak, J. *Applied Physics Letters* **2007**, 91, (22), 221909.
26. Lee, C.; Wei, X.; Kysar, J. W.; Hone, J. *Science* **2008**, 321, (5887), 385-388.
27. Huang, M.; Pascal, T. A.; Kim, H.; Goddard, W. A.; Greer, J. R. *Nano Letters* **2011**, 11, (3), 1241-1246.
28. Wu, Q.; Dai, Z.; Su, Y.; Volinsky, A. A.; Liu, L.; Zhong, Z. *Carbon* **2017**, 116, 479-489.
29. Espinosa, H. D.; Prorok, B. C.; Fischer, M. *Journal of the Mechanics and Physics of Solids* **2003**, 51, (1), 47-67.
30. Herbert, E. G.; Oliver, W. C.; de Boer, M. P.; Pharr, G. M. *Journal of Materials Research* **2011**, 24, (9), 2974-2985.
31. Turner, J. R. *International Journal of Solids and Structures* **1980**, 16, (5), 409-419.
32. Gao, Y.; Kim, S.; Zhou, S.; Chiu, H.-C.; Nélias, D.; Berger, C.; de Heer, W.; Polloni, L.; Sordan, R.; Bongiorno, A.; Riedo, E. *Nature Materials* **2015**, 14, 714.
33. Bhatia, N. M.; Nachbar, W. *International Journal of Non-Linear Mechanics* **1968**, 3, (3), 307-324.
34. Komaragiri, U.; Begley, M. R.; Simmonds, J. G. *Journal of Applied Mechanics* **2005**, 72, (2), 203-212.
35. *COMSOL Structural Mechanics Module User's Guide*, 5.0.1.276, December 17; 2014.
36. Wei, X.; Meng, Z.; Ruiz, L.; Xia, W.; Lee, C.; Kysar, J. W.; Hone, J. C.; Keten, S.; Espinosa, H. D. *ACS Nano* **2016**, 10, (2), 1820-1828.
37. Cao, C.; Daly, M.; Chen, B.; Howe, J. Y.; Singh, C. V.; Filleter, T.; Sun, Y. *Nano Letters* **2015**, 15, (10), 6528-6534.
38. Yoon, D.; Son, Y.-W.; Cheong, H. *Nano Letters* **2011**, 11, (8), 3227-3231.
39. Khomyakov, P. A.; Giovannetti, G.; Rusu, P. C.; Brocks, G.; van den Brink, J.; Kelly, P. J. *Physical Review B* **2009**, 79, (19), 195425.
40. Suk, J. W.; Kitt, A.; Magnuson, C. W.; Hao, Y.; Ahmed, S.; An, J.; Swan, A. K.; Goldberg, B. B.; Ruoff, R. S. *ACS Nano* **2011**, 5, (9), 6916-24.
41. Dahal, A.; Batzill, M. *Nanoscale* **2014**, 6, (5), 2548-2562.
42. Giovannetti, G.; Khomyakov, P. A.; Brocks, G.; Karpan, V. M.; van den Brink, J.; Kelly, P. J. *Phys Rev Lett* **2008**, 101, (2), 026803.
43. Mohiuddin, T. M. G.; Lombardo, A.; Nair, R. R.; Bonetti, A.; Savini, G.; Jalil, R.; Bonini, N.; Basko, D. M.; Galiotis, C.; Marzari, N.; Novoselov, K. S.; Geim, A. K.; Ferrari, A. C. *Physical Review B* **2009**, 79, (20), 205433.
44. Froehlicher, G.; Berciaud, S. *Physical Review B* **2015**, 91, (20), 205413.
45. Liu, F.; Ming, P.; Li, J. *Physical Review B* **2007**, 76, (6), 064120.
46. Teschner, D.; Pestryakov, A.; Kleimenov, E.; Hävecker, M.; Bluhm, H.; Sauer, H.; Knop-Gericke, A.; Schlögl, R. *Journal of Catalysis* **2005**, 230, (1), 195-203.
47. Seriani, N.; Mittendorfer, F.; Kresse, G. *The Journal of Chemical Physics* **2010**, 132, (2), 024711.
48. Teschner, D.; Borsodi, J.; Wootsch, A.; Révay, Z.; Hävecker, M.; Knop-Gericke, A.; Jackson, S. D.; Schlögl, R. *Science* **2008**, 320, (5872), 86-89.
49. Teschner, D.; Vass, E.; Hävecker, M.; Zafeiratos, S.; Schnörch, P.; Sauer, H.; Knop-Gericke, A.; Schlögl, R.; Chamam, M.; Wootsch, A.; Canning, A. S.; Gamman, J. J.; Jackson, S. D.; McGregor, J.; Gladden, L. F. *Journal of Catalysis* **2006**, 242, (1), 26-37.

50. Rabah, M.; Benalia, S.; Rached, D.; Abidri, B.; Rached, H.; Vergoten, G. *Computational Materials Science* **2010**, 48, (3), 556-562.

CHAPTER 6: STRENGTHENING AND TOUGHENING OF THIN METAL FILMS BY CVD GROWN GRAPHENE

Abstract:

Freestanding metal thin films ($<1 \mu\text{m}$ thickness) can have high yield strength yet are typically brittle. Nanoindentation experiments demonstrate that the yield strength of thin films increase substantially after the graphene synthesis. Due to CVD grown graphene's high conformability and superior interfacial strength on the metal substrate, it can reinforce thin metal films by constraining dislocations motion and strain localization at the metal grain boundaries. Nanoindentation can mimic pure uniaxial tensile loading on freestanding thin films, especially for thin film microbridge geometry, enabling studies on thin film strength and fracture toughness. The unusual strengthening observed from these experiments exceeds what could be expected from the rule of mixtures. To further probe the intrinsic toughening mechanisms at graphene-metal interface, I also studied the fracture behaviors of single crystal ultrathin Pd films reinforced by monolayer graphene synthesis. Preliminary results show clear evidence of stable crack propagation and extended ductility are observed in PdGr thin film composites, while bare Pd thin films show brittle failure behaviors. Possible explanations of these observations are provided.

6.1. Fracture of CVD grown Ni-MLG thin film composites

6.1.1. Strength of thin films probed by the membrane nanoindentation

We first evaluate the strength of CVD grown Ni-MLG thin film composites. As-grown Ni-MLG films are transferred onto a perforated substrate following the methods discussed before.

Nanoindentation is conducted using a cono-spherical indenter (tip diameter of 5 μm) on the center of freestanding circular Ni-MLG membrane. Equation 6.1 is used to estimate the maximum radial stress underneath the indenter.¹

$$\sigma_{rmax} = \sqrt{\frac{P_b E_t}{4\pi t c}} \quad (6.1)$$

where P_b is the breaking load when Ni-MLG starts to rupture, t is the membrane thickness, and c is the indenter tip radius. This value corresponds to the maximum stress in the membrane in the case of an indenter tip having finite but small radius and frictionless interface with the membrane. Importantly, we replace the elastic modulus E (calculated in the previous chapter) with the homogenized tangential modulus E_t extracted by fitting in the vicinity of the breaking load. This tangential modulus accounts for the local elastoplastic deformation at high loads following the Ramberg-Osgood strain hardening law, hence minimizes the overestimation of the breaking stress.² For freestanding membranes in this study, $c/a \ll 1$ (a is the membrane diameter), the load-displacement behavior is insensitive to the indenter tip radius. However, from Equation 6.1, the maximum stress underneath the indenter varies inversely with c , but shows no dependence on the membrane size.

Figure 6.1a shows the typical load-displacement behaviors of Ni-MLG, Ni and the MLG-on-Ni films until membrane breaking (marked as the red crosses). Figure 6.1b compares the calculated σ_{rmax} and the elastic modulus E (calculated in the previous chapter) for each film. For the freestanding MLG membrane (Ni-etched), $\sigma_{rmax} = 2.69 \pm 0.15 \text{ GPa}$, which is $\sim 2.1 \%$ of the intrinsic strength of a defect-free graphene monolayer.² For as-grown Ni-MLG having 7.35 vol. % (10.9 nm thick MLG), the maximum stress $\sigma_{rmax} = 2.35 \pm 0.2 \text{ GPa}$, representing 19.9 % increase over that for the as-sputtered Ni. Moreover, after removing MLG layer by O_2 RIE, the

average $\overline{\sigma_{rmax}}$ of Ni-C films show 6.1 % enhancements over the as-sputtered Ni. This is due to the carbon solution strengthening by the interstitial carbon atoms as well as metal-carbides, which is discussed in the previous chapter.

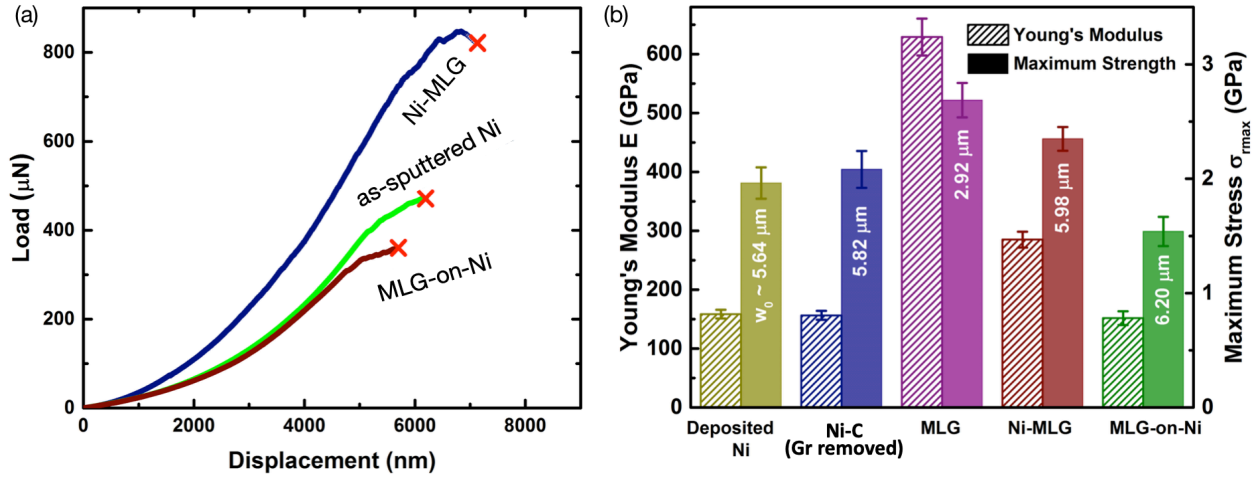


Figure 6.1. Fracture behaviors of freestanding Ni-MLG membranes. (a) Raw load-displacement curves for freestanding clamped circular Ni-MLG, as-sputtered Ni and the MLG-on-Ni thin films until fracture. (b) Summary of the elastic moduli and the maximum stresses in thin films. The values listed within stress columns are the maximum displacements corresponding to red crosses in (a).

From Figure 6.1b, the measured Ni-MLG thin film composite has a higher strength than the value predicted by the usual rule of mixture based on individually testing MLG (Ni-etched) and the Ni-C (MLG-etched): $\sigma_{r\ expected} = \nu_{MLG}\sigma_{MLG} + \nu_{Ni}\sigma_{Ni} = 2.12\ GPa$. The strengthening mechanisms of MLG in Ni-MLG can be explained by the conformal interface between graphene and the seed Ni achieved during CVD synthesis. This can also be further understood in light of the graphene synthesis mechanism on high interacting catalysts like Ni and Pd, in which dissolved carbon radicals segregate and precipitate to the metal grain boundaries and form

graphene layers during CVD cooling stage. As-grown graphene layers conform to and bridge the Ni grains and atomic vacancies in Ni. Because of the outstanding in-plane stiffness of the graphene, it plays a critical role in suppressing dislocation motion and delaying surface crack initiation under external stress. As a result, graphene delays the onset of yielding. Moreover, after yielding, the presence of graphene delays brittle fracture and enables the thin film to reach a higher maximum load as shown in Figure 6.1b.

6.1.2. Fracture behaviors at the graphene-Ni interface

At high indentation loads, microcracks start initiating and continue opening underneath the indenter tip. This is related to the discontinuities in the load-displacement curves, for example, as shown in Figure 6.2a inset. This enables the analysis of fracture behaviors of freestanding thin films with nanoindentation. On the other hand, it is known that fracture toughness does not obey the rule of mixtures. For instance, nacre and its artificial counterparts are ceramics which can be toughened by up to an order of magnitude by a few vol. % of soft low toughness polymer. Similarly, the toughness of ceramics can increase by over 235% due to the addition of 1.5 vol.% graphene.³ Here, we investigate the toughening of CVD grown MLG on the polycrystalline Ni substrate by comparing the breaking behaviors of as-grown Ni-MLG and the transferred MLG-on-Ni. Figure 6.2b and 6.2c highlight the cracking locations in two membranes in SEM. A consistent feature observed in the fractured Ni-MLG is the crack bridging of the Ni substrate by graphene layers. It is also observed that slip and pull-out between the MLG layers occur at the same location of the Ni cracks. We describe the coincident Ni cracks and MLG layer slip as collocated cracking, as sketched in Figure 6.2d. In contrast, the MLG-on-Ni shows much less strength (Figure 6.1b) and different fracture behavior compared to Ni-MLG, despite having the

same composition. In Figure 6.2c, the cracks in Ni and the pull-out in MLG occurs occur in different locations, we hence call it uncollocated crack initiation. Given the only difference between these two thin films is the interfacial adhesion of graphene on the metal, we explain the lower strength in the MLG-on-Ni by considering (i) the non-uniform van der Waals interfacial strength between graphene and Ni (which is inversely related to the Ni surface roughness), and (ii) the stress-free graphene-Ni interface. We believe these two factors characterized in chapter 4 lead to the uncollocated cracking.

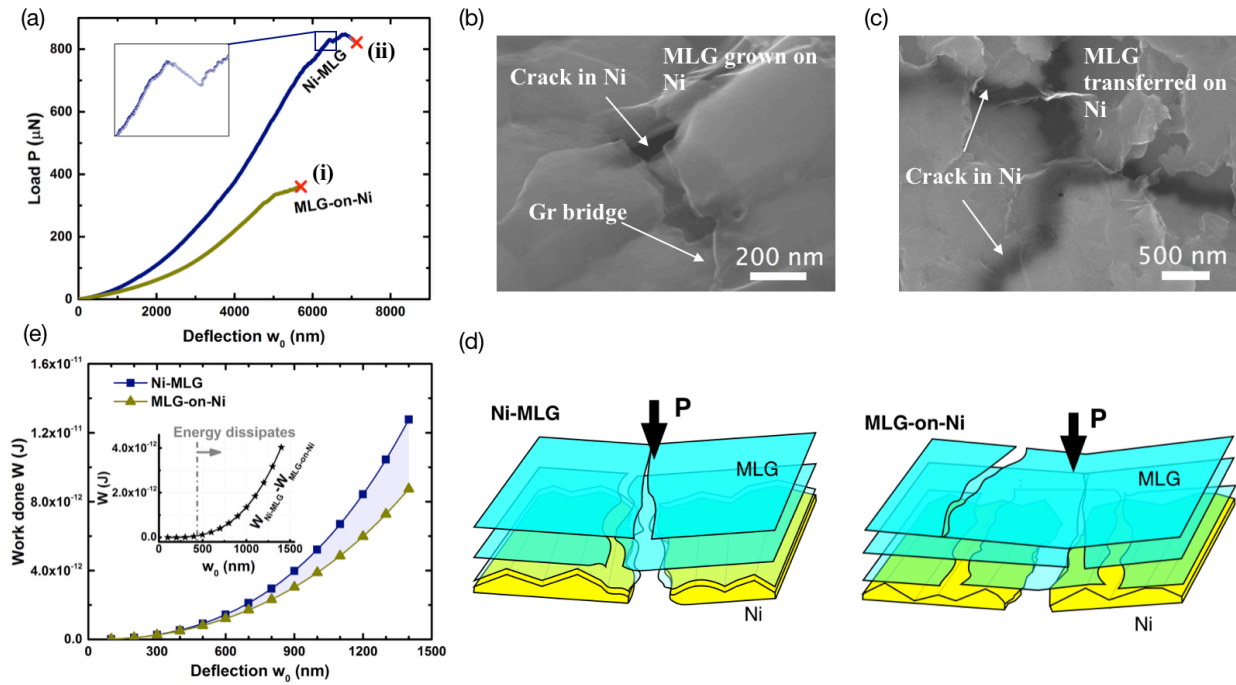


Figure 6.2. Strengthening mechanisms in Ni-MLG thin film composites. (a) Comparison of load-displacement curves of Ni reinforced by CVD synthesis of graphene (Ni-MLG) and by simply graphene transfer (MLG-on-Ni). Inset shows the discontinuity due to formation of micro cracks in membrane. (b-c) SEM images of the cracks in Ni-MLG and the MLG-on-Ni, respectively. (d) Schematics of the collocated versus the un-collocated cracking mechanism in Ni-MLG and the MLG-on-Ni. (e) Indentation work during loading of Ni-MLG and the MLG-on-Ni films by

Figure 6.2 (cont.)

integrating corresponding load-displacement curves. Inset gives the calculated energy dissipation due to interfacial slip between Ni and MLG in a deflected Ni-MLG film.

To obtain more quantitative insights into the toughness of the composite thin films, we calculate the energy dissipation during nanoindentation. The integration of indentation load with respect to the membrane displacement results in the work done W by the indenter:

$$W = \int_0^{w_b} P(w_0)dw_0 \quad (6.2)$$

where w_b is the membrane central deflection corresponding to the breaking load. Equation 6.2 presents the total energy transferred to the graphene-Ni system, including (i) the elastic strain energy in Ni and MLG layers, (ii) the plastic strain energy in Ni due to dislocation motion, (iii) the strain energy dissipated by interlayer slip within MLG, and (iv) the relaxation of interfacial stress and the corresponding energy dissipation between MLG and Ni. Figure 6.2e presents the indentation work for Ni-MLG and the MLG-on-Ni cases. The work done difference $W_{Ni-MLG} - W_{MLG-on-Ni}$, which is presented in the light blue region, demonstrates the evolution of energy dissipation in Ni-MLG composites. We attribute this energy dissipation to the interfacial relaxation between CVD grown graphene on Ni substrate beyond the purely elastic deformation ($w_0 < 0.5 \mu m$). It has been reported that the interfacial adhesion energy of CVD grown MLG on Ni surface is around $72.7 J m^{-2}$.⁴ In our case, the graphene-Ni interfacial interaction in Ni-MLG is shown as $\sim 20\%$ higher than that in the MLG-on-Ni. Figure 6.3 displays the cracks of the fractured membranes after indentation. In these tests, the indenter stops and retracts when the control algorithm detects a sudden decrease in load. The crack advancement length and geometry can be correlated to the fracture energy of membranes. In sputtered Ni, intergranular cracks

extending several micrometers are observed. Instead, the other three membranes (MLG, Ni-C and Ni-MLG) exhibit more confined crack propagation. The MLG membrane shown in Figure 6.3c and 6.3d also displays stable cracks compared to the dynamic cracking commonly observed in single crystal graphene monolayers. The crack morphologies are consistent with the reported studies on thick stacks of graphene oxide showing interlayer cleavage as well as through the thickness fracture pathways.⁵ Ni-MLG shows a highly jagged crack path which indicates the strong load transfer between Ni and MLG. The MLG-on-Ni develops long straight cracks as shown in Figure 6.3i and 6.3j. These observations confirm the crucial role of strong interfacial strength in achieving high strength and toughness in thin film composites.

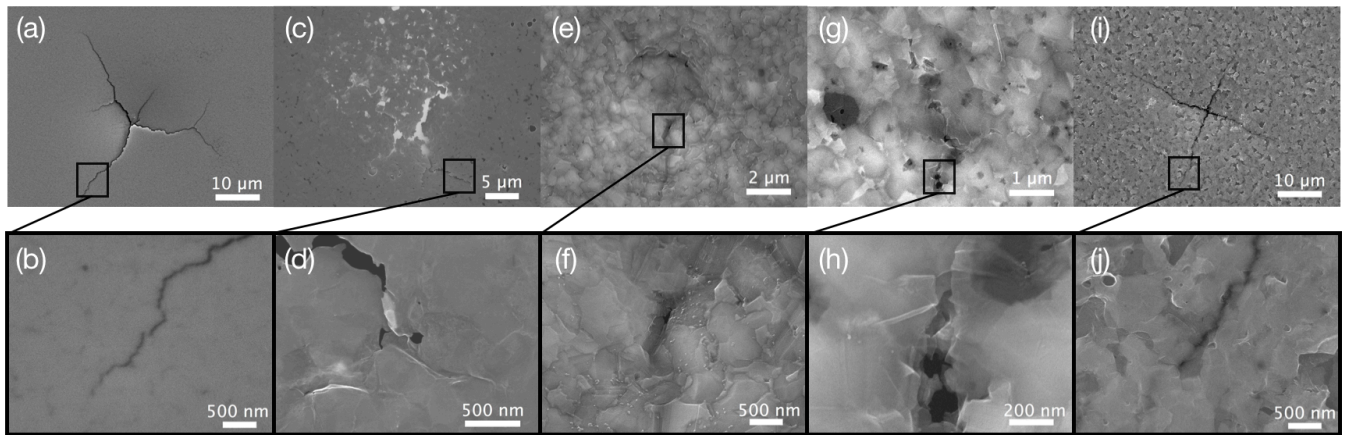


Figure 6.3. SEM images of post-indentation cracks in bare Ni (a-b), MLG (c-d), Ni-C (e-f), Ni-MLG (g-h) and the MLG-on-Ni (i-j).

In conclusion of CVD grown MLG reinforced polycrystalline thin Ni films, Figure 6.4 compares the extraordinary mechanical properties achieved by graphene synthesis to those in other most commonly used thin film materials in micro-electro-mechanical systems (MEMS) and flexible electronics fields. In particular, the fracture energy of thin films in this study is calculated by considering the fracture surface area in Equation 6.3:

$$G_c = \frac{\int_0^{w_b} P(w_0)w_0}{l_c t} \quad (6.3)$$

where, l_c is the total crack length measured in Figure 6.3. Using Equation 6.3, we calculate the typical fracture energy of Ni-MLG to be around 1407 J m^{-2} , which is an order of magnitude higher than the values for other deposited thin metal films.

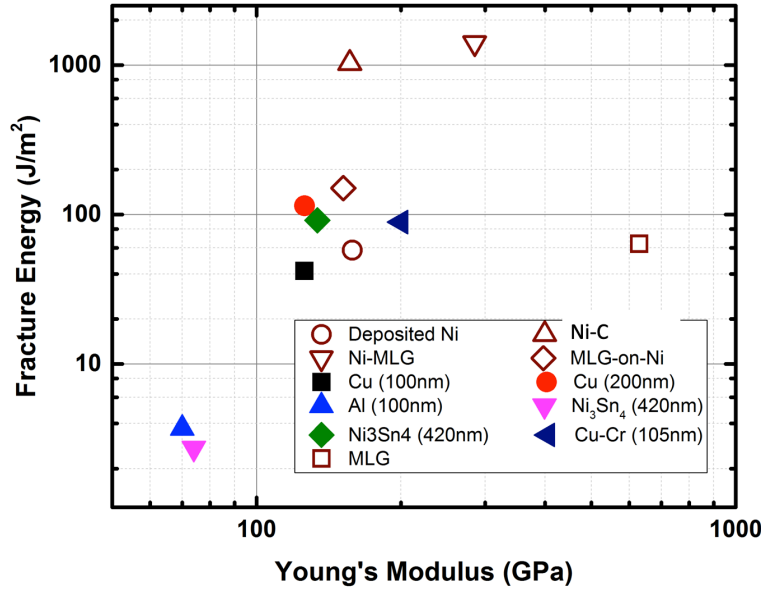


Figure 6.4. Summary of the elastic modulus versus fracture energy for Ni-MLG thin films and commonly-used thin metal films for MEMS and flexible electronic applications. Hollow points are thin films tested in this study. Solid points are Cu (100 nm),⁶ Cu (200 nm),⁷ Al,⁸ Au,⁹ Ni₃Sn₄,¹⁰ and Cu-Cr.¹¹

6.2. Strengthening and toughening of graphene monolayer on polycrystalline thin Pd films

Although outstanding strengthening of as-grown MLG in Ni-MLG system has been observed and discussed in the previous section, several open questions remain: (i) Equation 6.1 can overestimate the actual mechanical strength in freestanding thin films. It is based on the assumption that the indenter tip does not interact the deflected membrane. However, the top

graphene layer of the MLG may adhere and slide on the indenter tip, which will introduce non-homogeneous stress transfer across the tip interface and the thickness of the film. (ii) The high defect density nature of CVD grown MLG layer may cause sliding between the graphene layers and further initiate interlayer cracking path within the MLG. Given these drawbacks in the membrane nanoindentation and MLG, we turn to the modified microbridge testing with sputtered polycrystalline thin Pd films and their composites with monolayer graphene synthesis. Figure 6.5a sketches the nanoindentation using a wedge indenter tip on a doubly clamped freestanding thin film strip. The strip deformation has been discussed in the previous chapter. Specially, for a “ultrathin” strip having a low t/l ratio, the bending stiffness term in $P - h$ relation becomes very small, the deformation in strip hence is stretching dominated. As a result, we can mimic the pure tensile testing in two straight strip segments by applied line loading in nanoindentation. We also pattern freestanding strips into dog-bone shape using focus ion beam (FIB). Figure 6.5b shows the symmetric dog-bone-shape freestanding PdGr strips in TEM. Using a similar route described in chapter 5, we can synthesize graphene monolayer on the freestanding area. Figure 6.5c confirms that as-grown graphene monolayer conformably wraps Pd substrate in TEM as well as in Raman spectroscopy.

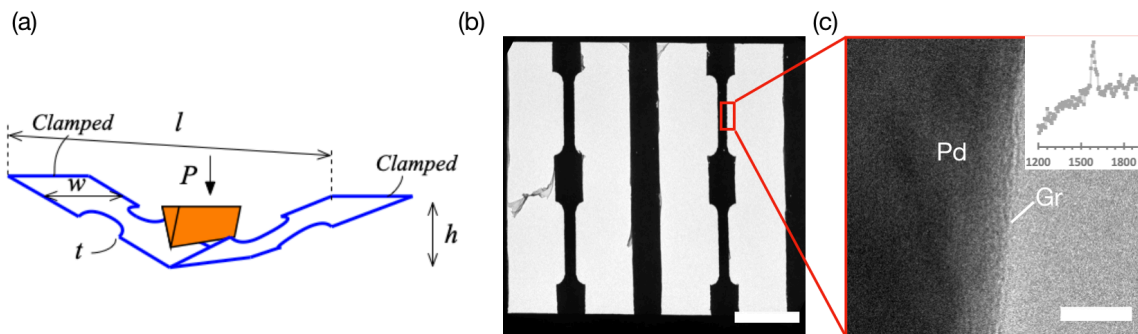


Figure 6.5. Strength and toughness characterization of ultrathin materials. (a) Microbridge testing on freestanding thin films with a dog-bone shape. (b) TEM images of two dog-bone shape

Figure 6.5 (cont.)

freestanding PdGr thin film composites on a TEM grid. Scale bar: 25 μm . (c) Zoomed-in TEM image on the edge of a PdGr film showing uniform Pd-monolayer graphene interface. Scale bar: 5 nm. Inset is the Raman spectrum (514 nm, 30s) on the same region confirming the existence of graphene layer.

Figure 6.6a depicts the typical $P - h$ behaviors of a sputtered Pd and a PdGr composite until thin film fracture. Similar to what we observe in Ni-MLG membrane testing, discontinuities in $P - h$ curves show up for Pd at high loads, and they are related to micro / nano cracks nucleation on metal surface. Notably, the same discontinuity is imperceptible for PdGr before fracture. This can be understood that high in-plane stiffness of graphene monolayer increases the energy barrier for dislocations to move towards metal surface and form surface steps. As a result, one layer high-quality graphene synthesis can effectively increase the elastic limit in thin metal films. The fitting algorithm proposed in chapter 5 with the elastic $P - h$ relation for microbridge testing helps to quantitatively determine the elastic limits of thin films. For the elastic deformation, fitting with an intermediate range (FR) should be independent of indent (h) and should results in consistent and low Root Mean Square Error (RMSE) values. Since the nanoindentation equations assume a linear elastic material (i.e. constant modulus), any abrupt increase in RMSE indicates the non-elastic behavior or the elastic limit in a thin film. Figure 6.6b compares the evolution of RMSE for Pd and PdGr. When strained to $\sim 0.27\%$, RMSE (Pd) increases immediately indicating the surface steps/cracks formation. Whereas, PdGr can be strained up to 0.43% until failure without surface steps initiation. A zoomed-in look at the early stage of RMSE evolution shown in the insets of Figure 6.6b suggests that non-elastic behavior starts in Pd from $\sim 0.06\%$,

but it is delayed in PdGr and start at $\sim 0.11\%$, which is about 83% enhancement in the onset of yielding.

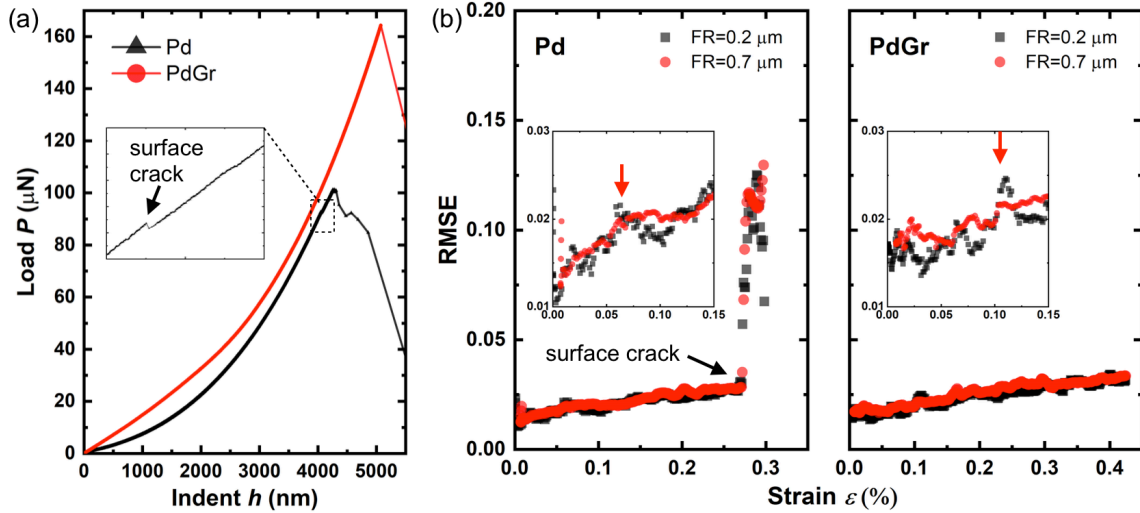


Figure 6.6. Microbridge testing of freestanding PdGr thin film composites beyond the elastic regime. (a) Full range load-displacement data of an as-sputtered Pd and as-grown PdGr thin films. Inset highlights the discontinuity in $P - h$ curve for Pd, which is related to the initiation of surface crack on metal surface under large deflection. (b) Comparison of RMSE of the elastic model fitting (Equation 5.6 in chapter 5) for Pd and PdGr at different strain levels. Insets are zoomed-in views for small strains below 0.15%.

We explain the increase in the onset of yielding by the suppression of dislocations motion towards the Pd-Gr interface due to the extremely high stiffness of the graphene layer. The dislocations gradually pile up near graphene-Pd interface and interact or tangle with each other thus also leading to strain hardening in these suspended thin films, and increases the fracture strength. An evidence supporting this hypothesis can be seen in the cross-sectional view of the indented thin films in TEM. Figure 6.7a sketches the typical slip band formation in bare Pd

films. The related behavior is seen in TEM in Figure 6.7b. In contrast, Figure 6.7c and 6.7d display the dislocation concentration near graphene-Pd interface, but without surface steps or slipping.

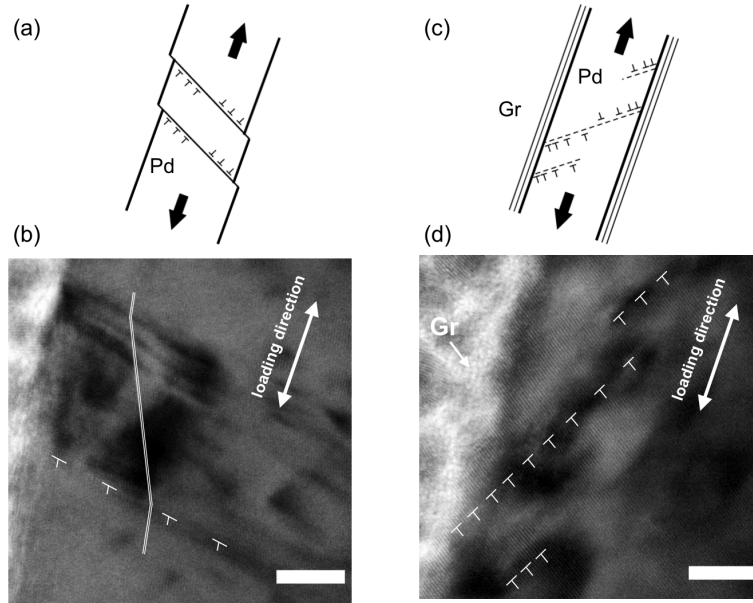


Figure 6.7. Enhancement of the elastic limit by monolayer graphene synthesis. (a) Schematic showing dislocation nucleation in a bare Pd under uniaxial tension, and dislocations move towards Pd surface and cause slip and plasticity. (b) Cross sectional TEM image of an indented thin Pd film. (c) Schematic showing dislocations pile up at graphene-Pd interface. Scale bar: 5 nm. (d) Corresponding cross sectional TEM image to (c) showing high dislocation density near Pd surface. Scale bar: 5 nm.

On the other hand, we can estimate and compare the tensile strength for two thin films using Equation 6.4:

$$N = \frac{P_b}{2\sin\theta} \approx \frac{P_b}{2 \cdot 2h_b/l_0} \Rightarrow \sigma_{max} = \frac{P_b l_0}{4h_b A} \quad (6.4)$$

where, P_b is the breaking load and h_b is the maximum indent before film fracture. l_0 is initial length of the strip, and A is cross sectional area. Table 6.1 lists the calculated results. $\sigma_{PdGr\ max} \approx 1.19\ GPa$ which is over 57 % increase over $\sigma_{Pd\ max} \approx 0.76\ GPa$. This enhancement is again beyond the prediction of the rule of mixtures assuming as-grown graphene has the intrinsic strength of 130 GPa.¹²

Table 6.1. Measurement of Pd and PdGr thin film strength in the microbridge nanoindentation

(loading rate: $0.5\ \mu N\ s^{-1}$, $l_0 = 105\ \mu m$)

Sample	Thickness (nm)	Dog-bone segment width (μm)	P_b (μN)	h_b (nm)	σ_{max} (GPa)
#1-sputtered Pd	206.2	3.5	97.98	4803	0.74
#2-sputtered Pd	206.2	3.1	101.2	4750	0.87
#3-sputtered Pd	206.2	2.8	79.89	5502	0.66
#4-PdGr	88.5	3.1	50.88	3632	1.34
#5-PdGr	88.5	3.1	41.41	2933	1.35
#6-PdGr	88.5	3.1	47.40	3559	1.27
#7-PdGr	206.9	4.1	159.50	4792	1.03
#8-PdGr	206.9	4.1	164.40	5282	0.96

More interesting consequence of the graphene “shielding” is observed when comparing the fractography of Pd and PdGr. Figure 6.8a and 6.8b show two fracture surfaces, in which bare Pd exhibits relatively straight crack propagation, whereas PdGr has a more jagged path. This is a clear sign of more energy dissipation in PdGr and has been discussed in Ni-MLG system. Importantly, unusual material thinning can be observed in PdGr. A close look in cross sectional view in TEM clearly shows this difference. In Figure 6.8c, Pd exhibits a flat fracture surface which is about 55° away from the tension direction. Black arrows highlight the dislocations which line up along the fracture surface. For PdGr, as shown in Figure 6.8d, obvious elongation and thickness reduction can be observed. More tangled dislocations are seen in PdGr, especially

near thin film surface. This can introduce more dislocation interactions and ductility in PdGr composites. A rigorous explanation for this difference caused by monolayer graphene synthesis is still underway. This will go to the future work of this study. The preliminary thoughts are represented in the next section.

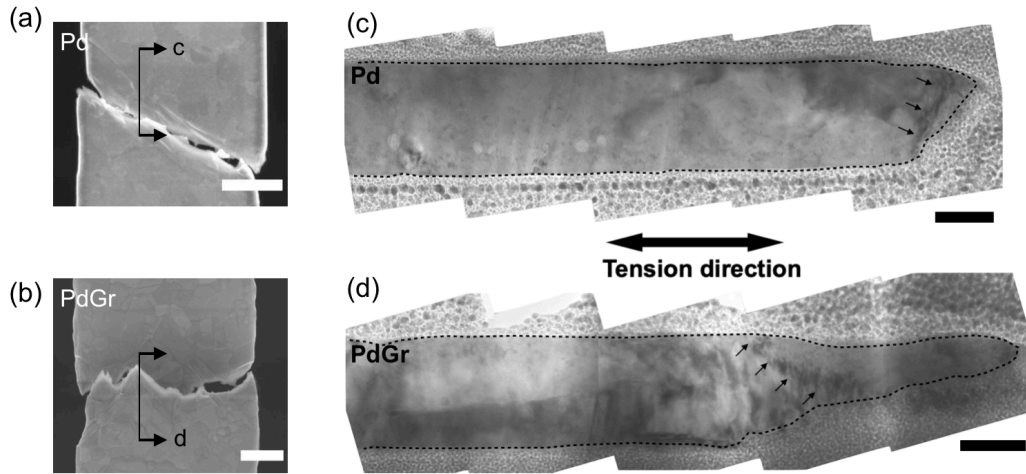


Figure 6.8. Fracture surfaces of bare Pd and as-grown PdGr thin film composites. (a-b) Top view SEM images of fractured Pd and PdGr, respectively. Scale bars: 1 μm . (c-d) Stitched cross sectional TEM images corresponding to fracture surfaces in (a) and (b). Scale bars: 50 nm.

6.3. Fracture behaviors of single crystal thin Pd films with graphene monolayer

A zoomed-in observation on fracture surfaces displayed in Figure 6.8 shows the inter and intra granular crack propagations because of the polycrystalline microstructures in the tested thin Pd films. This indicates both extrinsic and intrinsic toughening effects play roles in our experiments. To better understanding of the intrinsic toughening mechanisms of the graphene in composites, we repeated the testing in the previous section on freestanding single crystal PdGr thin film composites.

6.3.1. The onset of plasticity in as-grown PdGr thin film composites

We prepare freestanding Pd leaf strips having 150 nm in thickness and 10-15 μm in width, and use CVD to grown graphene monolayers on their surface following the recipes and the fabrication processes in Chapter 3 and Chapter 5 (Figure 5.7). Preliminary results are obtained from the microbridge testing. Under high loads beyond the elastic limit but below the breaking load, e.g. $P = 20 \mu\text{N}$, dislocations move to metal surface and surface steps can be observed in Pd, see Figure 6.9a. In contrast, PdGr displayed in Figure 6.9b does not show obvious surface steps or slip lines in TEM, but more dislocations than those in Pd. This observation is consistent with our understanding on the elastic limit enhancement in PdGr. Here, we can quantify the dislocation density increase under tension, e.g. $1.83 \times 10^9 \text{ cm}^{-2}$ in PdGr versus that in Pd is $7.12 \times 10^8 \text{ cm}^{-2}$. More systematic characterizations like slip direction, Pd orientation dependence are needed in the future work.

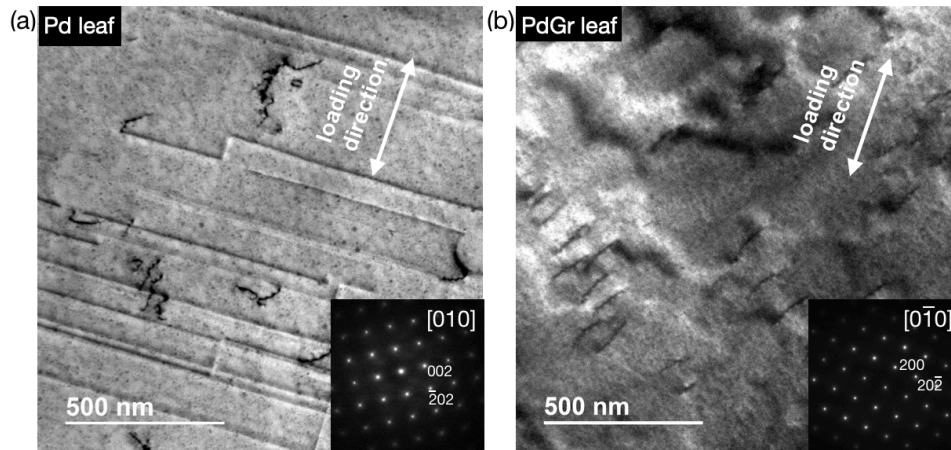


Figure 6.9. (a) Top view TEM image show surface steps / slip lines on Pd subjected to high load (20 μN) in microbridge indentation. The Pd leaf is annealed at 500 $^{\circ}\text{C}$ for 5 hrs before testing. (b)

At the same loading, no surface steps / slip lines are observed on PdGr surface. Insets TEM diffraction patterns confirm the single crystal orientation in Pd phase.

6.3.2. Crack propagation in thin metal films coated with graphene monolayer

As a consequence of notable strain hardening in PdGr composites, PdGr leaf composites exhibit qualitatively different fracture behaviors than bare Pd leaves. We firstly prepare freestanding dog-bone shaped Pd leaf strips using the route described in Figure 6.5. We make precracks with the tip radii < 200 nm using FIB on the dog-bone segments, as shown in Figure 6.10a. The tension applied by nanoindentation can trigger mode I fracture in thin films. The intrinsic fracture toughness of thin film materials is typically lower than plane strain fracture toughness (K_{Ic}). This is because of many factors for example strain localization and the rapid nucleation of cracks with limit size of the plastic zone. We indeed observe Pd leaves exhibit brittle fracture. This can be concluded by the straight crack morphology emerging from the precrack, as show in Figure 6.10b and 6.10c. On the other hand, we observe that PdGr composites exhibit saw-tooth like crack path, which is indicative of higher toughness, see Figure 6.10d and 6.10e. This serrated crack morphology is often observed when significant ductile behavior is present during crack propagation. Preliminary explanation for this is: the cracks follow the direction of the maximum shear stress which is orientation at 45° due to the plane stress nature in thin films. However, if the crack propagation is stable and the material is ductile, significant work hardening takes place in the metal ahead of the crack tip. This can redirect the crack from $+45^\circ$ to -45° following the other maximum shear stress direction. Figure 6.10f and 6.10g show the corresponding $P - h$ data for Pd and PdGr leaves. Close correlations of $P - h$ with TEM and SEM characterization can help to gain more fundamental understandings.

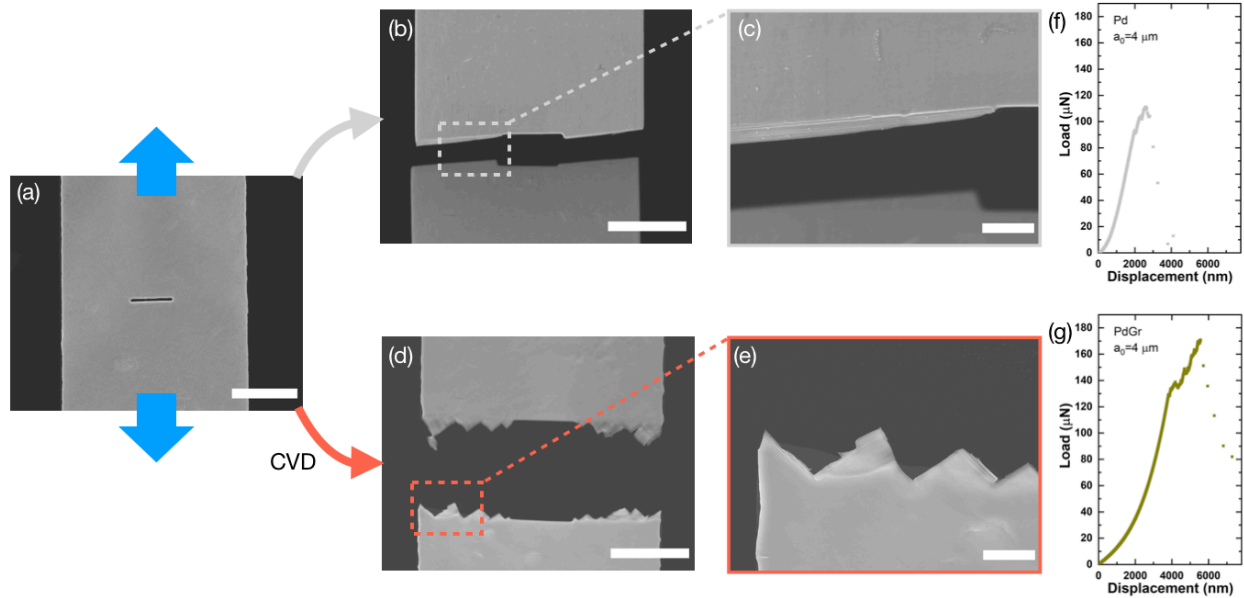


Figure 6.10. Fracture toughness testing on freestanding thin films in the microbridge nanoindentation. (a) SEM image of a freestanding Pd leaf strip with a central crack cut in FIB. This section will undergo pure tension and mode I fracture during nanoindentation. (b-c) SEM images of the fractured Pd leaf. (d-e) SEM images of the fracture PdGr leaf composite. (f-g) The load-displacement data for Pd and PdGr, respectively. Scale bars: Scale bars: 5 μm for (a), (b) and (d) and 1 μm for (c) and (e).

6.4. Conclusions

We probed the fracture behaviors of Ni-MLG thin film composites using the membrane nanoindentation. With 7.35 vol. % MLG synthesized on thin Ni films, 19.9 % enhancement in strength is achieved and it exceeds the average properties of the constituents. The critical fracture energy of as-grown Ni-MLG is found to be 1407 J m^{-2} which is an order of magnitude higher than other sputtered thin metal films. In particular, it is found that the ideal reinforcement should be conformal to the metal grains and have high interfacial interactions. This enables efficient load transfer across the whole material, as well as crack bridging and energy dissipation during

crack advancement. Similarly, obvious delay of onset of the plasticity and over 57 % increase in tensile strength are observed in thin Pd films with graphene monolayer synthesis. It is explained by the strain hardening enabled in the Pd due to the energy barrier to surface steps formation by graphene shielding. Finally, TEM imaging demonstrates that CVD grown PdGr thin film composite elongates significantly more before fracture compared to bare Pd. Together, these results can constitute the elements of a future study on the mechanisms of strengthening and toughening in graphene-metal thin film composites.

6.5. References:

1. Bhatia, N. M.; Nachbar, W. *International Journal of Non-Linear Mechanics* **1968**, 3, (3), 307-324.
2. Lee, C.; Wei, X.; Kysar, J. W.; Hone, J. *Science* **2008**, 321, (5887), 385-388.
3. Walker, L. S.; Marotto, V. R.; Rafiee, M. A.; Koratkar, N.; Corral, E. L. *ACS Nano* **2011**, 5, (4), 3182-3190.
4. Das, S.; Lahiri, D.; Lee, D. Y.; Agarwal, A.; Choi, W. *Carbon* **2013**, 59, 121-129.
5. C.H. Cao; M. Daly; B. Chen; J.Y. Howe; C.V. Singh; T. Filleter; Sun, Y. *Nano Lett.* **2015**, 15, 6528-6534.
6. H. Hirakata; O. Nishijima; N. Fukuhara; T. Kondo; A. Yonezu; Minoshima, K. *Mater. Sci. Eng. A* **2011**, 528, (28), 8120-8127.
7. R.R. Keller; J.M. Phelps; Read, D. T. *Mater. Sci. Eng. A* **1996**, 214, (1-2), 42-52.
8. M.A. Haque; Saif, M. T. A. *J. Mater. Res.* **2005**, 20, (7), 1769-1777.
9. H. Hosokawa; A.V. Desai; Haque, M. A. *Thin Solid Films* **2008**, 516, (18), 6444-6447.
10. Chen, Z.; He, M.; Balakrishnan, B.; Chum, C. C. *Mater. Sci. Eng. A* **2006**, 423, (1-2), 107-110.
11. H.G. Kim; J.W. Yi; S.W. Kim; K.S. Kim; Kumar, K. S. *Acta Mater.* **2015**, 84, 95-109.
12. Lee, C.; Wei, X. D.; Kysar, J. W.; Hone, J. *Science* **2008**, 321, (18), 385-388.

CHAPTER 7: CONCLUSIONS AND SUGGESTIONS FOR FUTURE WORK

7.1. Summary and conclusions

In this dissertation, we demonstrated a model system consisting of a micro / nanoscale metal catalyst coated by high-quality graphene and showed that this material system can properly bridge the understanding gap between atomic scale graphene interfacial mechanics and the mechanical properties of graphene-composites at the macroscale. To realize this, we have developed new methods for the synthesis of graphene on ultrathin materials in very short durations, and studied the graphene nucleation and growth kinetics, the resulting graphene-metal interfacial mechanics and the mechanical behaviors of graphene-metal thin film composites. These composite thin films can have applications in flexible electronics with superior mechanical behavior and longer life. Moreover, the new understanding paves the way to designing bulk graphene-based metallic composites with enhanced mechanical behaviors.

In Chapter 2, we have developed a laser assisted draw-casting (LDC) process to downsize metallic microwires into nanoscale continuous wires to be used as catalysts for graphene synthesis. LDC is based on modified Taylor drawing process, which can quickly yield continuously long metal micro / nanowires with giant crystalline structures. This offers a neat and defect-scarce platform for graphene to nucleate on, and importantly, an efficient way to characterize graphene-metal interface as in a core-shell composite.

Due to nanowires' high surface-volume ratios and the solid-state dewetting instability at the graphene synthesis temperatures, we turned our efforts to a relatively simpler system: ultrathin

metal films, presented in Chapter 3. These thin films are readily available in various grain size and allowed us to study the reinforcement mechanisms of graphene synthesis in ultrathin polycrystalline materials. We selected Ni and Pd as the catalysts in rapid chemical vapor deposition (CVD) synthesis for their strong interactions with graphene, high carbon solubility and better resistance to solid-state dewetting. We have studied the graphene nucleation kinetics by considering dynamic carbon segregation and precipitation driven by temperature change and found an optimal window for large crystal low defect graphene monolayer to form.

High-quality graphene monolayer grown on thin metal substrates enables us to focus on intrinsic graphene-metal interface properties. In Chapter 4, we focused on the interfacial mechanics of graphene synthesized by CVD on Ni and Pd. This study was carried by a combination of Raman spectroscopy and TEM imaging on the polycrystalline samples. Comparison of the Raman spectra of graphene on various Pd crystal orientations allows us to correlate the strains to the graphene-metal lattice mismatch, which we think are critical factors in graphene-based composites. It is found CVD grown graphene is highly conformable and largely epitaxial on Pd, but may be in unexpected strain states (either tension or compression) based on the combination of metal grain orientation and graphene rotation orientation.

In Chapter 5 and 6, we have unveiled that the high interfacial stress from graphene growth on thin metal films effectively modifies the elastic properties in graphene-metal composites. In Chapter 5, we have tested the mechanical behaviors of Ni-MLG and PdGr by various indentation methods: tip-based indentation of supported films as well as indentation of freestanding membranes and microbridges. From these tests, we calculated the elastic properties of the

composite graphene-metal thin films. In addition, the conformable graphene shielding on metal surface increases the energy barrier for the surface steps formation due to dislocation motion, and allows strain hardening to occur in thin metal substrates. We have qualitatively studied this toughening effect of graphene monolayer on thin Pd films.

7.2. Discussions and suggestions for future work

In this section, I discuss the insights obtained in this dissertation and the possible next steps to drive better understanding and applications carbon-based materials.

7.2.1. Synthesis of graphene single crystal on polycrystalline metal substrates

Achieving large area high quality graphene sheets require large graphene crystal size as well as low nucleation density. Using the rapid CVD synthesis recipes presented in Chapter 3, we are able to synthesize single graphene crystals with size up to 34 μm on 150 nm thick Pd films, with nucleation density as low as $10^{-3} \mu\text{m}^{-2}$. However, this is still far smaller than the giant graphene crystals grown on bulk metal catalysts with low growth rates.¹⁻³ It is expected, in our case, to obtain larger graphene crystals if increasing the growth time at synthesis temperature, however, the solid-state dewetting issue of thin metal films would rise and limit the synthesis. In light of this, I propose the next research steps to improve graphene crystallinity on ultrathin metal catalysts.

Lateral homoepitaxial growth of graphene via CVD on a pre-deposited domain from mechanical exfoliation has been achieved on copper foils in a previous study.⁴ Similarly, in-plane growth of a pre-nucleated graphene domain with multiple heating-cooling cycles could expand graphene

crystal size without substrate dewetting. This can be realized by cyclic loading and retracting Pd catalysts to and from the hot zone while controlling precursor gas flows. A batch of single crystal graphene domains will nucleate from the first growth cycle, and a subsequent heating-cooling round can drive additional carbon radicals to Pd surface and possibly register to the edges of the pre-nucleated domains.

On the other hand, recent study on evolutionary selection growth of graphene on polycrystalline copper foils develops a method to achieve continuous single crystal graphene monolayer by aligning and merging sub graphene hexagonal domains across copper grains.⁵ We indeed observed various graphene hexagons orientations and even symmetries on different Pd grains in Chapter 3 and Chapter 4. The systematic correlations of graphene crystal geometry and alignment to growth front motion as well as CVD parameters are needed for the next step.

7.2.2. The intrinsic toughening mechanisms in graphene-metal nanocomposites

Chapter 5 and 6 mainly focused on the extrinsic strengthening and toughening mechanisms in graphene-metal thin film composites, e.g. grain bridging, collocated cracking and crack path redirection. However, we expect that the intrinsic toughening mechanisms related to ductility within the metal grain also play a significant role in these materials. To further probe the limits of the intrinsic toughening mechanisms of graphene in composites, we need a simplified model system consisting a single metal grain / single crystal orientation and high-quality graphene monolayer covering the entire area of the grain. With the rapid CVD synthesis route developed in Chapter 3 for coarse grain Pd leaf, as well as the fabrication flows proposed in Chapter 5, we are able to fabricate freestanding ultrathin Pd leaves with monolayer graphene synthesis. The

PdGr leaf system has large ($> 20 \mu\text{m}$) Pd grain size and high-quality graphene monolayer. By fabricating freestanding leaf strips with width less than $20 \mu\text{m}$, we have a chance to mimic the tensile testing on a single crystal thin Pd film and its composites with high-quality graphene monolayer synthesis.

Observations of fracture in these PdGr leaves presented in Chapter 6 suggest the strain hardening and the consequential ductility in thin metal films from graphene shielding. This behavior can solve the long-standing problem of the brittleness of metal thin films used in electronic devices, particularly flexible electronics. It is quite impressive that a monolayer of graphene can resist the fracture by this much. Owing to its potential impact, I propose that this material system is studied in detail. For example, the fracture toughness of thin films can be studied quantitatively as function of crack size and sample geometry.⁶ The fracture behavior can be studied to reveal the separate roles of crack nucleation/initiation versus crack propagation. This study should be correlated to microstructure studies by TEM.

The ultralong Pd nanowires fabricated by LDC - presented in Chapter 2 - offer another platform for making core-shell nanowires for studies on PdGr nanowire composites. As-drawn Pd via LDC also has large ($> 80 \mu\text{m}$) grain size in a bamboo-shape structure. We obtain regular graphene domains on the drawn Pd wires. While these nanowires suffer from solid-state dewetting of Pd at synthesis temperatures exceeding 1000C due to their cylindrical geometry, it is however expected that new CVD recipes can be developed at lower temperatures to enable high quality graphene growth within short durations.

7.2.3. Multi-functionality in graphene-metal composites

Besides the enhancement in the mechanical behaviors, CVD grown graphene-metal nanocomposites also exhibit superb electrical properties. For example, as-grown Ni-MLG thin film composites show high electrical conductivity of $9.87 \times 10^6 \text{ S m}^{-1}$, which is slightly higher than a bare Ni film of $9.49 \times 10^6 \text{ S m}^{-1}$. This can be attributed to the enhanced elastic surface electron scattering due to surface passivation with low-density-of-state graphene.⁷ Moreover, directional thermal conductivity enhancement has been observed in graphene-copper matrix composites.⁸ To probe the limit of electrical and thermal conductivities in graphene-based composite materials, a study on electron transport and phonon scattering at the graphene-metal interfaces is needed.

One more thought about the graphene-metal interfaces is the rise of the chemical reactivity in both graphene and the underlying metal substrates. It is known that graphene can be functionalized by strain engineering.^{9,10} It has been recently reported that the high compressive strain in graphene due to epitaxial CVD growth on copper foils significantly increases the chemical reactivity in the graphene layer. A study on the orientation related interfacial strain observed in Chapter 4 would drive more insights into strain-induced graphene functionalization via CVD synthesis. On the other hand, the metal substrates in as-grown graphene-metal composites can also gain functionalities from the interfacial strain. Notably, Pd used in this dissertation, is also an important catalyst which can be widely used for selective hydrogenation of alkynes into alkenes in chemical engineering industry.¹¹ Two findings from the recent research in chemistry may motivate a study on tunable chemical reactivity of ultrathin Pd films from graphene synthesis: (i) It is found that the population of subsurface sites of Pd by carbon

governs the hydrogenation events on the Pd surface.¹¹ In Chapter 5, we have verified the existence of interstitial carbon and its carbides near the Pd surface by graphene synthesis. It is possible to tune the concentration of these subsurface carbon in CVD processes, hence control the reactivity on Pd surface. (ii) Pd (110) nanosheets with control on the intrinsic surface strain show optimized catalytic reactivity for the oxygen reduction and hydrogen evolution reactions.¹² We have demonstrated, in Chapter 4, that CVD synthesis on Pd leaves can introduce a range of strain from -0.1 % to 0.4 % in a single layer graphene. In Chapter 5, this interfacial strain has been shown to rise the Pd surface energy to one order of magnitude. It is reasonable to boost the reactivity of a thin Pd film by harnessing the graphene-Pd interfacial strain from in situ synthesis.

Overall, the synthesis and mechanical behaviors in graphene-metal nanocomposites is very rich with deep scientific questions, and offers an untapped potential to design future engineering materials at all scales for applications ranging from flexible electronic devices to aerospace structures.

7.3. References:

1. Gao, L.; Ren, W.; Xu, H.; Jin, L.; Wang, Z.; Ma, T.; Ma, L.-P.; Zhang, Z.; Fu, Q.; Peng, L.-M.; Bao, X.; Cheng, H.-M. *Nature Communications* **2012**, 3, 699.
2. Wu, T.; Zhang, X.; Yuan, Q.; Xue, J.; Lu, G.; Liu, Z.; Wang, H.; Wang, H.; Ding, F.; Yu, Q.; Xie, X.; Jiang, M. *Nature Materials* **2015**, 15, 43.
3. Xu, X.; Zhang, Z.; Dong, J.; Yi, D.; Niu, J.; Wu, M.; Lin, L.; Yin, R.; Li, M.; Zhou, J.; Wang, S.; Sun, J.; Duan, X.; Gao, P.; Jiang, Y.; Wu, X.; Peng, H.; Ruoff, R. S.; Liu, Z.; Yu, D.; Wang, E.; Ding, F.; Liu, K. *Science Bulletin* **2017**, 62, (15), 1074-1080.
4. Wang, H.; Wang, G.; Bao, P.; Shao, Z.; Zhang, X.; Yang, S.; Zhu, W.; Deng, B. *CrystEngComm* **2014**, 16, (13), 2593-2597.
5. Vlassiounk, I. V.; Stehle, Y.; Pudasaini, P. R.; Unocic, R. R.; Rack, P. D.; Baddorf, A. P.; Ivanov, I. N.; Lavrik, N. V.; List, F.; Gupta, N.; Bets, K. V.; Yakobson, B. I.; Smirnov, S. N. *Nature Materials* **2018**, 17, (4), 318-322.
6. Lanning, W. R.; Javid, S. S.; Muhlstein, C. L. *Fatigue & Fracture of Engineering Materials & Structures* **2017**, 40, (11), 1809-1824.
7. Mehta, R.; Chugh, S.; Chen, Z. *Nano Lett* **2015**, 15, (3), 2024-30.
8. Chu, K.; Wang, X.-h.; Wang, F.; Li, Y.-b.; Huang, D.-j.; Liu, H.; Ma, W.-l.; Liu, F.-x.; Zhang, H. *Carbon* **2018**, 127, 102-112.
9. Li, Y.; Jiang, X.; Liu, Z.; Liu, Z. *Nano Research* **2010**, 3, (8), 545-556.
10. Si, C.; Sun, Z.; Liu, F. *Nanoscale* **2016**, 8, (6), 3207-3217.
11. Teschner, D.; Borsodi, J.; Wootsch, A.; Révay, Z.; Hävecker, M.; Knop-Gericke, A.; Jackson, S. D.; Schlögl, R. *Science* **2008**, 320, (5872), 86-89.
12. Wang, L.; Zeng, Z.; Gao, W.; Maxson, T.; Raciti, D.; Giroux, M.; Pan, X.; Wang, C.; Greeley, J. *Science* **2019**, 363, (6429), 870-874.